POLITECNICO DI TORINO

Master's Degree in Mechanical Engineering



Experimental Evaluation and Predictive Modeling of
Composite Materials Crashworthiness.

Supervisor:

Prof. Davide Salvatore Paolino

Rodrigo Cruz Ojeda S300503

Candidate:

Company Supervisor:

Lorenzo Vigna

Academic Year 2024/2025

Acknowledgments

A mis padres y hermanos que me han mostrado en todo momento su apoyo incondicional y quienes son la causa de todos mis meritos.

To all those who have accompanied me through this first stretch of life, awakening countless curiosities that have shaped who I am and who I strive to become.

Ringrazio Lorenzo, il mio tutor, che mi ha guidato e mi ha dimostrato di cosa siano capaci la costanza e la resilienza, ispirandomi a credere che lo spirito possa superare le condizioni materiali e sociali.

The following work stands upon the resilient endurance of those who came before me, alongside every unrecorded effort that allowed thoughts to become action, and action to become mastery.

Abstract

The growing demand for safer, lighter, and more sustainable structures has accelerated the development and validation of composite materials, which offer exceptional combinations of strength and low weight. This thesis, a collaboration between Politecnico Di Torino, ITW Test and Measurement Italia s.r.l. - Instron CEAST division, and The Leibniz-Institut für Verbundwerkstoffe GmbH, investigates a novel testing methodology for assessing Specific Energy Absorption (SEA) and introduces predictive models to evaluate the influence of geometry on crashworthiness performance.

Motivated by the lack of a universal standard for the assessment of the SEA, this study investigates the performance of six different composite materials (CF-PA6, CF-PA66, CF-PC, GF-PP, GF-TEPEX, and CF-Epoxy) were tested under dynamic loading using an Instron 9450 drop tower and high-speed imaging. This study systematically explored the effects of geometry, boundary conditions, and impact velocity on energy absorption, aiming to isolate the intrinsic crash performance of each material.

Extensive data processing and statistical analyses identified the key parameters driving SEA variability, which were then integrated into predictive models capable of estimating the performance of corrugated geometries based on flat coupon tests. The results show that geometry and velocity significantly affect crashworthiness and that no universal predictive model applies across all composites; each material exhibits distinct behaviors.

This study advances the experimental evaluation of composite crashworthiness by providing a reproducible methodology and predictive framework that supports the design of lightweight crashworthy structures for automotive, aerospace, and related applications.



Contents

A	ckno	wledgments	iii
\mathbf{A}	bstra	act	V
1	Inti	roduction	1
	1.1	Relevance of Crashworthiness	1
	1.2	Importance of Specific Energy Absorption (SEA)	2
	1.3	Predicting SEA of corrugated coupons using flat coupon data.	2
	1.4	Objectives of the study	3
	1.5	Scope and limitations	3
2	Lite	erature Review	5
	2.1	Crashworthiness and Its Importance	5
	2.2	Composite Materials in Crash-worthy Applications	8
		2.2.1 Common Composite Structures used for Crashworthiness	9
	2.3	Failure Modes in Composite Materials	10
	2.4	Testing Methodologies for Crashworthiness for composite ma-	
		terials	14
		2.4.1 Benchmark for Crashworthiness testing methods	15
	2.5	Non-Standard Test Methodologies and Innovations	19
3	Exp	perimental Methodology	23
	3.1	Test Setup	23
	3.2	Coupons and Materials	24
	3.3	Test Procedure	26
	3.4	Data Processing and Analysis	28

	3.5	Validation and Prediction	31
	3.6	Limitations	34
4	Exp	perimental Testing and Analytical Framework	37
	4.1	Crash testing	37
		4.1.1 CF-PA6	37
		4.1.2 CF-PA66	41
		4.1.3 CF-PC	45
		4.1.4 GF-PP	48
		4.1.5 GF-TEPEX	54
		4.1.6 CF-Epoxy	56
		4.1.7 Variable velocity Crash testing	57
	4.2	SEA Evaluation	65
		4.2.1 SEA	66
		4.2.2 SEA as function of velocity	68
	4.3	Statistical Fitting Models	82
	4.4	Data Validation	92
	4.5	Predictive Models	95
5	Res	ults and Discussion	103
	5.1	Experimental Observations	103
	5.2	Confidence intervals	104
	5.3	Statistical Validation	
	5.4	Performance of Prediction Models	113
6	Cor	nclusions and Future Work	115

List of Figures

1.1	Press hardened B-Pillar, an example of an scalable Crashwor- thiness design that take advantage of the thermo-mechanical	
	properties of materials to enhance crashworthiness.[4]	1
1.2	Toyota GR010 Hybrid after the Sebring crash. Image credit: Sportscar365 [5]	2
2.1	Theoretical crash test output from a corrugated coupon	7
2.2	CFE crash test example	8
2.3	Comparison of SEA between composites and metals [22]	9
2.4	(A) Transverse shearing mode,(B) Brittle fracturing mode,(C) Lamina bending mode,(D) Local buckling mode.[8]	11
2.5	(A) Splaying mode, (B) Fragmentation mode [16]	12
2.6	Carbon fiber-Polycarbonate flat specimen test (A) Beginning of the test showing a fragmentation failure mode (B) Delamination and local buckling mode (C) Fragmentation mode	13
2.7	Crashworthines test performed in tube specimens of different	
	diameters. [14]	15
2.8	Test Fixture developed by NASA [8]	15
2.9	Feraboli Coupon. [12]	16
2.10	Scale and type of manufacturing defects on composite mate-	
	rials [13]	17
2.11	Taxonomy of defects in composite materials as proposed by Potter [26]. The classification highlights the relationship be-	
	tween manufacturing processes, geometry, and defect formation.	18

2.12	Flat coupon fixture, left figure presents the assembly of the fixture and right figure presents the fixture without the closing	20
2.13	gate allowing the view of the coupon	21
3.1	Drop Tower Setup for dynamic load tests	23
3.2	Sinusoidal coupon holder	24
3.3	Technical drawing for the IVW coupon geometry	25
3.4	From left to right: (a) The oven and vacuum pump, (b)	
	Coupons inside the drying process and (c) Balance and weight	2.0
2 -	of the specimens	26
3.5	Process for loading the Vigna Fixture, a) fixture after the end	
	of the test; b) unclamping the specimen rotating the handle on	
	the right; c) opening the door on the left side; d) extraction	
	of the specimen; e) removal of the debris and powders; f)	
	positioning a new specimen and door closing; g) fastening	
	the door using the handle on the left side; h) clamping the	0.5
2.0	specimen using the torque-limited handle on the right side. [28]	27
3.6	Diagram for data analysis of the Flat and corrugated coupons.	30
3.7	Diagram for building the prediction models	33
3.8	Diagram for the statistical evaluation of the models	34
4.1	Force as function of displacement results for Splaying setup of	
	CF-PA6	38
4.2	Cumulative energy transferred as function of displacement re-	
	sults for Splaying setup of CF-PA6	38
4.3	Delamination failure mode on coupons PA6-F-1 (upper part)	
	and PA6-F-3 (lower part)	39
4.4	Force as function of displacement results for Tearing setup of	
	CF-PA6	40
4.5	Cumulative energy transferred as function of displacement re-	
	sults for Tearing setup of CF-PA6	40
4.6	Buckling failure of the upper part of coupons PA6-F-7 and	
	PA6-F-8	40

4.7	of CF-PA6	41
4.8	Cumulative energy transferred as function of displacement re-	11
4.0	sults for Corrugated coupons of CF-PA6	41
4.9	Force as function of displacement results for Splaying setup of CF-PA66	42
4.10	Cumulative energy transferred as function of displacement re-	
	sults for Splaying setup of CF-PA66	42
4.11	Force as function of displacement results for Tearing setup of	
	CF-PA66	43
4.12	Cumulative energy transferred as function of displacement re-	
	sults for Tearing setup of CF-PA66	44
4.13	Force as function of displacement results for corrugated coupons of CF-PA66	44
4.14	Cumulative energy transferred as function of displacement re-	
	sults for Corrugated coupons of CF-PA66	45
4.15	Force as function of displacement results for Splaying setup of CF-PC	45
4.16	Cumulative energy transferred as function of displacement results for Splaying setup of CF-PC	46
4.17	Experimental Test of coupon AG-02-4 experiencing delamina-	
	tion and buckling failure modes	46
4.18	Force as function of displacement results for Tearing setup of	
	CF-PC	47
4 19	Cumulative energy transferred as function of displacement re-	_,
1.10	sults for Tearing setup of CF-PC	47
4.20	Force as function of displacement results for corrugated coupons	
	of CF-PC.	48
4.21	Force as function of displacement results for Splaying setup of	
	GF-PP	49
4.22	Cumulative energy transferred as function of displacement re-	
	sults for Splaying setup of GF-PP	49

4.23	GF-PP Flat coupons after Crashworthiness Splaying test, de-	
	lamination in multiple layers can be observed	50
4.24	Force as function of displacement results for Tearing setup of GF-PP	51
4.25	Cumulative energy transferred as function of displacement results for Tearing setup of GF-PP	51
4.26	GF-PP Vigna coupons after Crashworthiness Tearing test, multiple failure modes are observed	52
4.27	Force as function of displacement results for short corrugated coupons of GF-PP. (Instron tested)	53
4.28	Cumulative energy transferred as function of displacement results for Corrugated coupons of GF-PP	53
4.29	Force as function of displacement results for corrugated coupons of GF-PP. (IVW tested)	54
4.30	Force as function of displacement results for Splaying setup of GF-TEPEX	54
4.31	Force as function of displacement results for Tearing setup of GF-TEPEX	55
4.32	Force as function of displacement results for Corrugated setup of GF-TEPEX	55
4.33	Force as function of displacement results for Splaying setup of CF-EPOXY	56
4.34	Force as function of displacement results for Tearing setup of CF-EPOXY	56
4.35	Force as function of displacement results for corrugated setup of CF-EPOXY	57
4.36	300 [kN] Instron 6800 Series Universal Testing Machine setup.	58
	Quasi-static and Dynamic test comparison of a Splaying setup of a CF-PA66 coupons	59
4.38	From left to right, (A) Bottom part of quasi-static CF-PA66 coupon. (B) CF-PA66 in the testing bench	60

4.39	of a CF-PC coupons	61
4.40	From left to right, (A) Bottom part of quasi-static CF-PC	
	coupon. (B) CF-PC in the testing bench	61
4.41	Quasi-static and Dynamic test comparison of a Splaying setup	
	of a GF-PP coupons	63
4.42	From left to right, (A) Bottom part of quasi-static GF-PP	
	coupon. (B) GF-PP in the testing bench	63
4.43	Quasi-static and Dynamic test comparison of a Tearing setup	
	of a GF-PP coupons	64
4.44	Force-displacement curve for splaying setup of variable veloc-	
	ity tests on GF-PP	65
4.45	Force-displacement curve for tearing setup of variable velocity	
	tests on GF-PP	65
4.46	SEA obtain from experimental data of CF-PC, CF-Epoy and	
	CF-PA6 (From left to right)	67
4.47	SEA obtain from experimental data of GF-TEPEX, CF-PA66	
	and GF-PP (From left to right)	68
4.48	CF-PC Splaying test, (A) Velocity-displacement curve (B)	
	Force-displacement curve	69
4.49	From left to right, Splaying, Tearing and corrugated results	
	of SEA evaluation under high and low speed evaluation for	
	CF-Epoxy coupons	70
4.50	From left to right, Splaying, Tearing and corrugated results	
	of SEA evaluation under high and low speed evaluation for	
	CF-PA6 coupons.	70
4.51	From left to right, Splaying, Tearing and corrugated results	
	of SEA evaluation under high and low speed evaluation for	71
4 50	CF-PA66 coupons	71
4.52	From left to right, Splaying, Tearing and corrugated results	
	of SEA evaluation under high and low speed evaluation for	70
	CF-PC coupons	72

4.53	From left to right, Splaying and Tearing crushing velocity-	
	displacement curve and corrugated results of SEA evaluation	
	under high and low speed evaluation for GF-PP coupons	73
4.54	From left to right, Splaying crushing velocity-displacement	
	curve, Tearing and corrugated results of SEA evaluation under	
	high and low speed evaluation for GF-TEPEX coupons	74
4.55	$SEA_{(\dot{x})}$ -Crushing velocity curve for splaying and tearing setup	
	CF-Epoxy	75
4.56	$SEA_{(\dot{x})}$ -Crushing velocity curve for corrugated setup CF-	
	Epoxy	76
4.57	$SEA_{(\dot{x})}$ -Crushing velocity curve for splaying and tearing setup	
	CF-PA6	76
4.58	$SEA_{(\dot{x})}$ -Crushing velocity curve for short corrugated setup	
	CF-PA6	77
4.59	$SEA_{(\dot{x})}$ -Crushing velocity curve for splaying and tearing setup	
	CF-PA66	78
4.60	$SEA_{(\dot{x})}$ -Crushing velocity curve for short corrugated setup	
	CF-PA66	78
4.61	$SEA_{(\dot{x})}$ -Crushing velocity curve for splaying and tearing setup	
	CF-PC	79
4.62	$SEA_{(\dot{x})}$ -Crushing velocity curve for short corrugated setup	
	CF-PC	79
4.63	$SEA_{(\dot{x})}$ -Crushing velocity curve for splaying and tearing setup	
	GF-TEPEX	80
4.64	$SEA_{(\dot{x})}$ -Crushing velocity curve for corrugated setup GF-	
	TEPEX	80
4.65	$SEA_{(\dot{x})}$ -Crushing velocity curve for splaying and tearing setup	
	GF-PP	81
4.66	$SEA_{(\dot{x})}$ -Crushing velocity curve for short corrugated setup	
	GF-PP	81
4.67	$SEA_{(\dot{x})}$ -Crushing velocity curve for IVW corrugated setup	
	GF-PP	82

4.68	(A) Splaying setup coupon, (B) Tearing setup coupon, (C)	
	IVW Geometry coupon, each of the coupons exhibit different	
	number of curvatures	83
4.69	Linear statistical fitting model curve for the parameter of	
	number of curvatures	85
4.70	Exp. statistical fitting model curve for the parameter of the	
	number of curvatures	86
4.71	Log. statistical fitting model curve for the parameter of the	
	number of curvatures.	86
4.72	Left figure the total length for the fixing points in a tearing	
	setup for flat coupon. The right figure is the length in between	
	the smallest distance of fixing points for flat coupon under a	
	tearing setup	87
4.73	Linear statistical fitting model curve for the parameter Rate	
	of distance	90
4.74	Exp. statistical fitting model curve for the parameter Rate of	
	distance	90
4.75	Log. statistical fitting model curve for the parameter Rate of	
	distance	91
4.76	Manufacturing defects presented in a CF-PA6 coupon by a	
	CT-Scan	94
4.77	Linear predictive model with the number of curvatures	96
4.78	Log. predictive model with the number of curvatures	97
4.79	Linear predictive model with the Rate of distance parameter.	99
4.80	Log. predictive model with the Rate of distance parameter	100
5.1	Confidence intervals curve of Experimental Data and Predic-	
	tion Models for CF-EPOXY	105
5.2	Confidence intervals curves of Experimental Data and Predic-	
	tion Models for CF-PA66	106
5.3	Confidence intervals curves of Experimental Data and Predic-	
	tion Models for CF-PA6 tested at Instron	107

5.4	Confidence intervals curves of Experimental Data and Predic-
	tion Models for CF-PA6 tested at IVM
5.5	Confidence intervals curves of Experimental Data and Predic-
	tion Models for CF-PC
5.6	Confidence intervals curves of Experimental Data and Predic-
	tion Models for GF-TEPEX
5.7	Confidence intervals curves of Experimental Data and Predic-
	tion Models for GF-PP tested at Instron
5.8	Confidence intervals curves of Experimental Data and Predic-
	tion Models for GF-PP tested at IVW

List of Tables

2.1	SEA vs CFE material comparison [29]	8
3.1	Drop Tower technical specs	24
3.2	Properties of the investigated composite materials	25
3.3	Test plan for materials and institutions of testing	26
3.4	Test parameters for the test plan	28
4.1	Test conducted for variable velocity	57
4.2	Test parameters for the variable velocity test plan	62
4.3	Mean SEA values with their respective standard deviation	68
4.4	$SEA_{(\dot{x})}$ results for CF-Epoxy	70
4.5	$SEA_{(\dot{x})}$ results for CF-PA6	71
4.6	$SEA_{(\dot{x})}$ results for CF-PA66	72
4.7	$SEA_{(\dot{x})}$ discrete approach for CF-PC	73
4.8	$SEA_{(\dot{x})}$ discrete approach for GF-PP	74
4.9	$SEA_{(\dot{x})}$ discrete approach for GF-TEPEX	74
4.10	Unaltered SEA $R^2 - Coeff$. for linear, exponential and log-	
	arithmic statistical fitting models	83
4.11	Normalized SEA $R^2 - Coeff$. for linear, exponential and log-	
	arithmic statistical fitting models	83
4.12	SEA normalized to the mean of the corrugated coupons \mathbb{R}^2 –	
	Coeff. for linear, exponential and logarithmic statistical fit-	
	ting models	84
4.13	Normalized SEA RMSE for linear, exponential and logarith-	
	mic statistical fitting models	84

4.14	Unaltered SEA $R^2 - Coeff$. for linear, exponential and log-	00
	arithmic statistical fitting models	88
4.15	Unaltered SEA $R^2 - Coeff$. for linear, exponential and logarithmic statistical fitting models	88
4.16	Unaltered SEA $R^2 - Coeff$. for linear, exponential and logarithmic statistical fitting models	88
1 17		00
4.17	Normalized SEA RMSE for linear, exponential and logarithmic statistical fitting models	89
4.18	Statistical Parameters of CF-PA6 for the null hypothesis anal-	
	ysis	92
4.19	Null Hypothesis results for CF-PA6 to the evaluation of H_0 .	93
4.20	Statistical Parameters of GF-PP for the null hypothesis analysis.	94
4.21	Null Hypothesis results for GF-PP to the evaluation of H_0	94
4.22	Comparison of STD for linear model between CMC and MC Models for different materials	97
4.23	Comparison of STD for log. model between CMC and MC Models for different materials	98
4.24	Comparison of STD for linear model between CMC and MC Models for different materials	99
4.25	Comparison of STD for Log. model between CMC and MC Models for different materials	101
5.1	Confidence intervals data of Experimental Data and Prediction Models for CF-EPOXY (in all cases, values are given in $[kJ \cdot kg^{-1}]$)	105
5.2	Confidence intervals data of Experimental Data and Prediction Models for CF-PA66 (in all cases, values are given in $[kJ \cdot kg^{-1}]$)	106
5.3	Confidence intervals data of Experimental Data and Prediction Models for CF-PA6 (in all cases, values are given in $[kJ \cdot kg^{-1}]$)	

5.4	Confidence intervals data of Experimental Data and Predic-	
	tion Models for CF-PC (in all cases, values are given in $[kJ\cdot$	
	kg^{-1}])	108
5.5	Confidence intervals data of Experimental Data and Predic-	
	tion Models for GF-TEPEX (in all cases, values are given in	
	$[kJ \cdot kg^{-1}]$)	109
5.6	Confidence intervals data of Experimental Data and Predic-	
	tion Models for GF-PP (in all cases, values are given in $[kJ\cdot$	
	kg^{-1}])	110
5.7	Null hypothesis results of predictive models with positive pre-	
	dictive outcomes.	112
5.8	Null hypothesis results of predictive models with not capable	
	predictive outcomes	113
5.9	Performance of predictive models by materials correctly pre-	
	dicted	114



Chapter 1

Introduction

1.1 Relevance of Crashworthiness

According to the Imperial College of London definition of Crashworthiness can be defined as, The ability of land-,sea- or air-vehicles to survive a collision without that part of the structure containing the payload suffering unacceptable distortion or deceleration. [23], this is an essential characteristic for design, intrinsic to material properties used in a broad range of applications as automotive, aerospace and sports where the ability to absorb energy during impact events is essential for the safety of the users and the structural integrity of the vehicle.

These applications can be seen extensively in our daily lives, from energy-absorbing elements in cars, crush barriers on highways, and sports safety gear to crash energy management systems in trains. This shows a clear trend of growing demand for crash-worthy designs and a deep understanding of their underlying

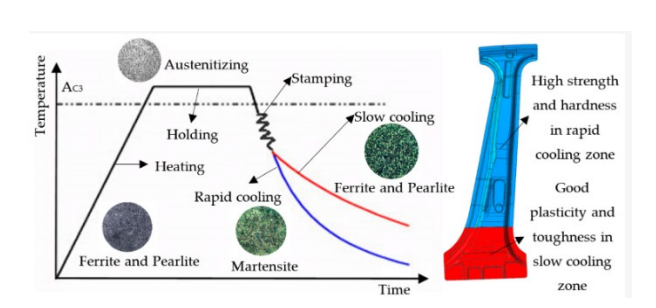


Figure 1.1: Press hardened B-Pillar, an example of an scalable Crashworthiness design that take advantage of the thermo-mechanical properties of materials to enhance crashworthiness.[4].

physics. The search for new materials capable of delivering the required performance has been accelerated by the tendency for the reduction of the emissions and the search for carbon neutrality defined at last at the Paris agreement [27]. Considering that the transportation sector accounts for ap-

proximately 24% of global CO2 emissions [6] the need for the development of lightweight materials that do not compromise the structural integrity of the vehicle has been a driver for the integration of new materials, such as advanced composites, which play a relevant role in this effort, offering the potential to significantly reduce vehicle weight and improve fuel efficiency. However, the anisotropic nature of these materials necessitates advanced testing and modeling techniques to accurately predict their energy-absorption capabilities.

1.2 Importance of Specific Energy Absorption (SEA).

Specific Energy Absorption (SEA) is the main parameter used to evaluate the Crashworthiness of materials. It is defined as the energy absorbed per unit mass of a material during an impact. High SEA values are desirable because they indicate efficient energy dissipation while minimizing weight, which is crucial for applications



Figure 1.2: Toyota GR010 Hybrid after the Sebring crash. Image credit: Sportscar365 [5].

in which weight reduction is a priority. Composite materials are anisotropic, and their performance varies according to a long set of variables intrinsically attached to the materials themselves, such as fiber orientation, stacking sequence, matrix properties, and geometric configuration. Accurate prediction of SEA is essential for optimizing the design of crash-worthy structures and ensuring their performance under dynamic loading conditions[8].

1.3 Predicting SEA of corrugated coupons using flat coupon data.

Despite the extensive research on the crashworthiness of composite materials, predicting the SEA of complex geometries from basic elements, such as coupons, is challenging, and corrugated coupons provide the best relation to real-world scenarios [25]. However, there have been some efforts to

characterize flat coupons due to their simplicity and ease of testing, and to evaluate the materials based on their failure modes [8]. However, the behavior of corrugated structures under impact can differ significantly because of stress concentrations, geometric effects, and localized failure modes.

1.4 Objectives of the study.

This study builds on the work of Vigna by developing a non-standard methodology for the Crashworthiness evaluation of composite materials. The methodology involves an assessment of flat coupons to evaluate the different failure modes of the materials [28], with the aim of predicting the Specific Energy Absorption (SEA) of corrugated coupons. This approach aims to provide an accurate and efficient method for estimating the SEA of corrugated coupons, with the main goal of predicting complex geometries, ultimately advancing the design of lightweight, crash-worthy structures.

1.5 Scope and limitations.

The primary objectives of this study were as follows:

- 1. Evaluate the behavior, forces, and energy absorption of flat and corrugated composites for the most common composite materials under dynamic loading conditions.
- 2. Evaluate trends and fitting models to determine if there is a correlation between flat failure modes and corrugated failure modes.
- 3. Develop a predictive model for estimating the SEA of corrugated coupons using data from flat coupon tests.
- 4. Validate the proposed model through experimental testing and statistical analysis.

This study focuses on fiber-reinforced polymer composites with a specific emphasis on flat geometries. The scope of this study includes experimental testing, data processing, statistical analysis, and development of a predictive model. However, this study is limited to specific materials and loading conditions, and the findings may not be directly applicable to other composite configurations or impact scenarios.

Chapter 2

Literature Review

2.1 Crashworthiness and Its Importance

The study of crashworthiness has evolved in various industries. In the automotive sector, Béla Barényi introduced crumple zones in Mercedes-Benz vehicles in 1950 [3]. Meanwhile, in the aerospace sector, DeHaven published studies on energy absorption and occupant protection in crashes in 1942, laying the foundation for the evolution of crashworthiness. The 1980s marked a shift towards composite materials, driven by the demands of aerospace, such as crash-worthy helicopter seats, and motorsports, such as the Formula 1 carbon fiber monocoque [1]. Regulatory frameworks, including FMVSS 214 for automotive and FAA 25.562 for aircraft, later standardized crashtesting protocols, emphasizing energy absorption and occupant survivability [19].

As previously defined, crashworthiness refers to the ability of a structure to protect its occupants by absorbing impact energy through controlled failure modes and mechanisms [23]. The energy absorption capacity of a material is often evaluated through crash tests in which the material is subjected to dynamic loading conditions. The energy absorbed (E) during the impact of any material can be calculated using the following formula:

$$E = \int_0^d F_{(x)} \cdot dx \tag{2.1}$$

Where:

• $F_{(x)}$ is the force as function of displacement (x)

• d is the total displacement of the component deformation during the impact.

This relationship indicates that the energy absorbed by the material during impact can be obtained by integrating the reaction force over the deformation path. The primary objective of crash-worthy designs is to maximize energy absorption and reduce deceleration to enhance safety, as can be seen in this formula, and this objective is highly dependent on the material properties. However, due to recent years technological drivers aimed at developing new materials to achieve carbon neutrality by 2050 [27], this has been a genuine driver for weight reduction and lightweight design.

Specific Energy Absorption (SEA) is a metric that evaluates those two main parameters essential to Crashworthiness, Energy Absorption and mass, It is defined as the energy absorbed per unit mass of the material during an impact event:

$$SEA = \frac{\int_0^d F_{(x)} \cdot dx}{\rho \cdot A \cdot \int_0^d dx}$$
 (2.2)

Where:

- $F_{(x)}$ is the force as function of displacement (x).
- \bullet 0 d is the total displacement under steady state conditions of the impact.
- ρ is the material density.
- A is the cross section of the component under evaluation.

Higher SEA values are more desirable because they indicate efficient energy dissipation while minimizing weight, which is crucial for applications where weight reduction is a priority; typical units of SEA are in $kJ \cdot kg^{-1}$. Conversely, the impact behavior is not as straightforward as this formula suggests, as shown in Figure 2.1.

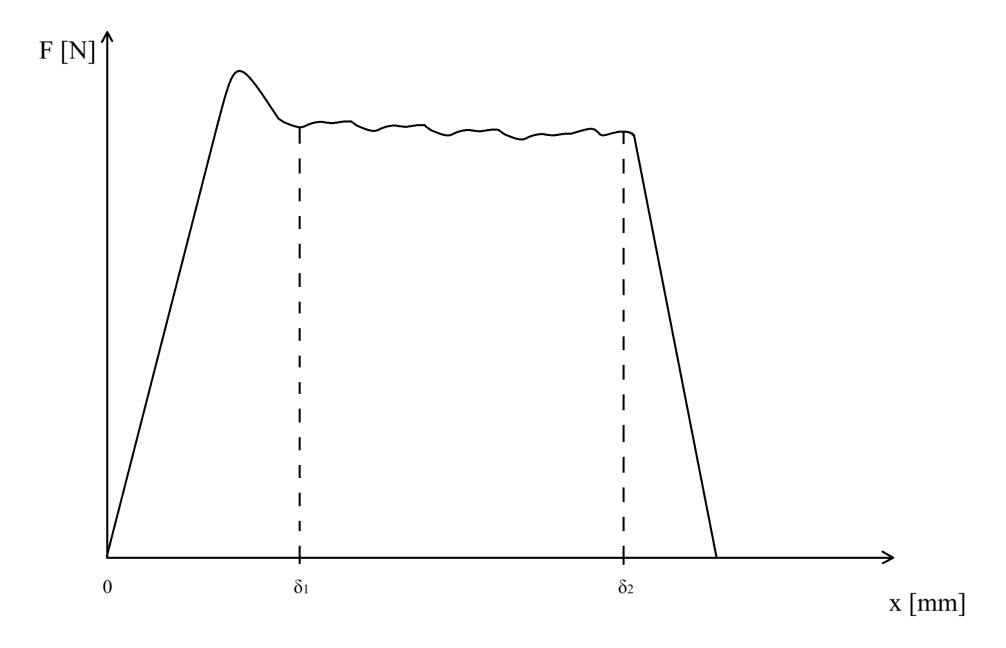


Figure 2.1: Theoretical crash test output from a corrugated coupon.

The evaluation of an impact has some stages, as it is shown the stage between 0 and δ_1 is known as the crush initiator region, where the maximum force is reached. This occurs because of the transition from the initial portion of the coupon—called the **trigger**—whose purpose is to enable the material to begin absorbing energy and to ensure a smooth transition toward a stable plateau of energy absorption defined by the geometry of the structure, followed by the region between δ_1 and δ_2 , which is considered the steady-stage crush behavior region, and finally after δ_2 represents the final stage of the test, where the coupon has absorbed all the energy.

Although SEA is a useful parameter for measuring the energy absorbed per unit mass, other parameters, such as Crush Force Efficiency (CFE), can also indicate the performance of crash components, and it is a key parameter used to evaluate the energy absorption characteristics of a structure during an impact. The CFE is defined as the ratio of the mean crushing force to the peak force experienced during deformation:

$$CFE = \frac{F_{mean}}{F_{peak}} \tag{2.3}$$

Where:

• F_{mean} is the average force experience during the test (x).

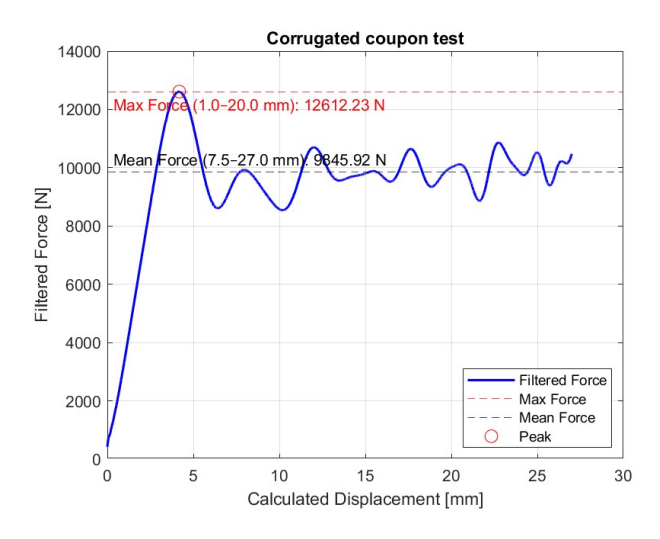


Figure 2.2: CFE crash test example

• F_{peak} is the maximum force experience by the coupon.

These parameters vary significantly across material classes due to differences in the deformation mechanisms. For instance, metals such as steel absorb energy through plastic deformation, whereas composites rely on progressive fiber fracture and delamination. Table 2.1 compares these metrics for common materials, highlighting the superior SEA and CFE of composite materials relative to metals, which is a key driver for their adoption in lightweight crash-worthy designs.

Material	SEA $[kJ \cdot kg^{-1}]$	CFE $[N/N]$
Steel (HSLA)	10–15	0.4 – 0.6
Aluminum (6061)	20-30	0.5 – 0.7
CF-DLR (Carbon Fiber-Termosett)	50-100	0.7-0.9

Table 2.1: SEA vs CFE material comparison [29].

2.2 Composite Materials in Crash-worthy Applications

Composite materials are engineered by combining two or more constituent materials with distinct physical or chemical properties to achieve superior performance characteristics. Typically, they consist of a reinforcing phase (e.g., carbon, glass, or aramid fibers) embedded in a matrix (e.g., epoxy, polyester, or thermoplastic polymers). This combination leverages the high strength and stiffness of the fibers, along with the matrix's ability to dis-

tribute loads and protect the fibers from environmental degradation. The resulting materials exhibit exceptional strength-to-weight ratios, corrosion resistance, and customizable—properties that are highly desirable in crashworthy applications such as automotive, aerospace, and sports safety equipment [25],

The customization nature of composite materials makes them a great choice for developing crash-worthy designs; however, as shown in Figure 2.3, traditional materials such as steel or aluminum underperform under dynamic loading. The ability of composite materials to dissipate energy relies on the progressive failure of fiber fracture, matrix cracking, and controlled delamination, whereas metals rely on

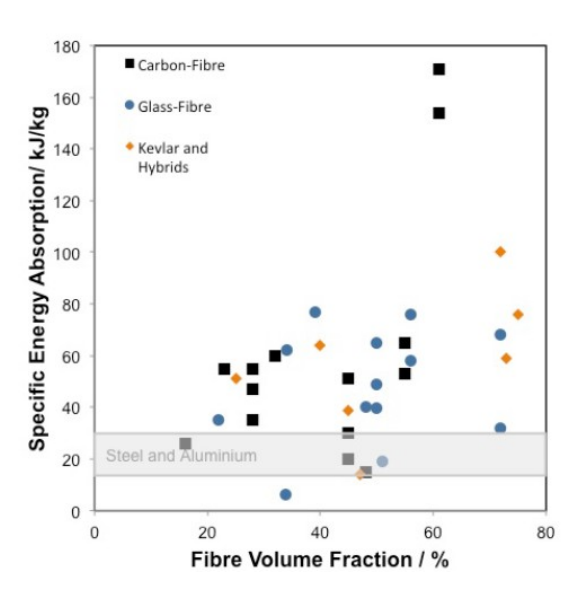


Figure 2.3: Comparison of SEA between composites and metals [22]

plastic deformation, which is a less efficient mechanism under dynamic loading[22].

2.2.1 Common Composite Structures used for Crashworthiness

In crash-critical environments where the SEA-to-weight ratio is a driver for development, typical applications are found in the motorsport industry, such as F1, Space exploration for the structural integrity of landing modules[24], aerospace inside fuel systems, and landing gear for helicopters[7]. To achieve this goal, several composite structural forms are routinely used to enhance crashworthy designs.

- 1. **Crash tubes:** Cylindrical, square or conical tubes are commonly used as energy absorbing elements and are well studied in terms of its axial crushing behavior[1].
- 2. Sandwich Panels: Their energy absorption capability arises from a

layered structure composed of composite face sheets bonded to a lightweight core, typically honeycomb or foam. The core is primarily responsible for absorbing impact energy through deformation or crushing, whereas the face sheets distribute and stabilize the load during impact[1].

3. Laminated Flat Panels: Used in the impact test for standardized specimens of ASTM D7136/D7137, which determines the damage resistance of multidirectional composite plates after an impact test.

2.3 Failure Modes in Composite Materials

During a crash, many dynamic complex phenomena take place in the behavior of composite materials, and the nature of these and the relationship between the bonding of the fibers and matrix create a complex environment that can behave very differently during failure. The failure of the material is the result of many of the following phenomena:

- Fibers failure due to tensile or compression stress, the failure mode of the fiber is function on the nature of the material itself, for example brittle failure is typical of glass or carbon fibers while ductile failure is more frequent on thermoplastic fibers
- Matrix failure can withstand tensile, compressive and shear loads, as for the fibers the failure mode is related to the material which constitutes the matrix, which can have brittle failure with strong fragmentation usually present in thermosets or plastic deformation typical for thermoplastics.
- Debonding between the fibers and the matrix.
- Delamination in between the layers of the composite material.

There has been a deep study on the failure of composite materials, since the complexity of its anisotropy has driven different approaches to define a model that can predict its behavior. Tsai-Hill proposed a failure theory based on Von-Mises anysotropic material approach, adapting it to a unidirectional lamina[25]; while for dynamic loading conditions Gary Farley and Robert

Jones at NASA [8] whereas at Cambridge D. Hull [16] have developed studies for the study of failure modes in composite materials.

As shown in Figure 2.4 Farley and Jones[8] studied the failure modes of composite materials by crushing circular and square cross-section tubes and described four possible failure modes of composite materials during crash testing:

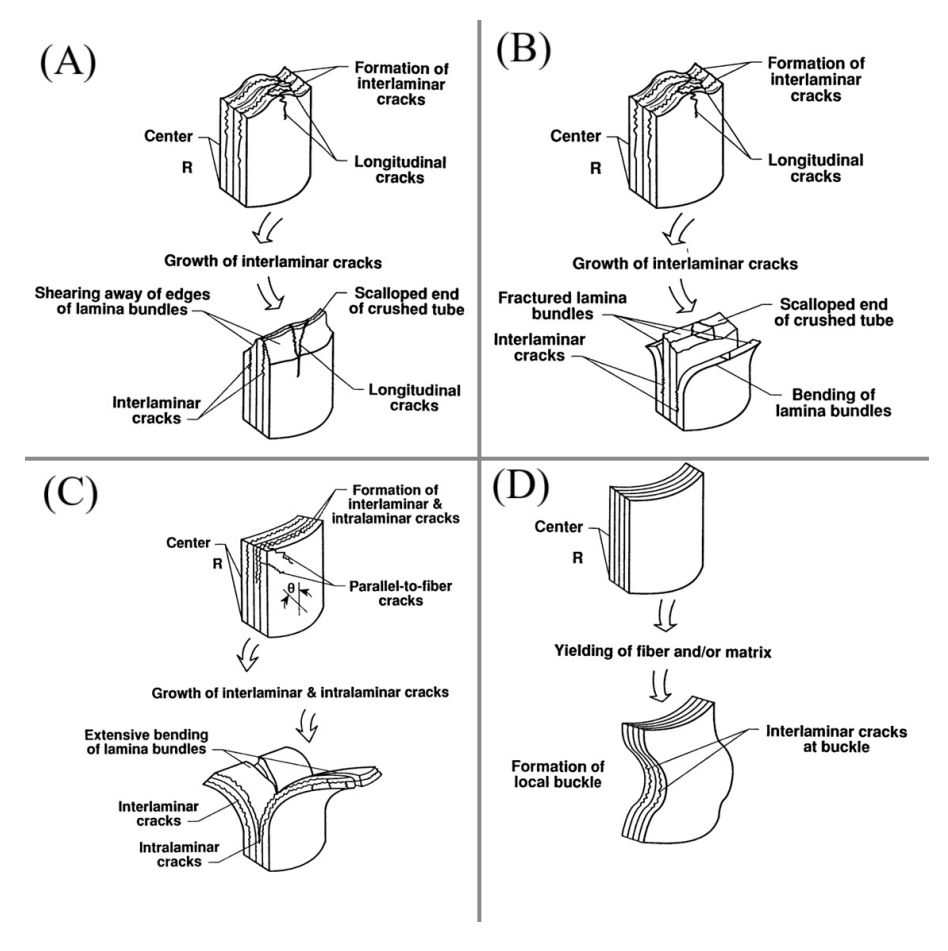


Figure 2.4: (A) Transverse shearing mode, (B) Brittle fracturing mode, (C) Lamina bending mode, (D) Local buckling mode.[8]

- 1. Transverse shearing mode, the composite structure fails due to shear stresses acting perpendicular to the fibers direction, this result in the formation of shear cracks across the laminate leading to a progressive collapse of the structure. Energy absorption is efficient due to the progressive shear that forms conical cross sections.
- 2. Brittle fracturing mode, its characterized by interlaminar cracks with a length size between one and ten laminate thickness, the lamina layer bends and fractures near to the base of its deformation. The energy

absorption results were efficient because of the lamina bundles.

- 3. Lamina bending mode, its characterized by interlaminar, intralaminar and parallel-to-fiber cracks of a length size more than ten times bigger than laminate thickness which tend to form lamina bundles. The composite structure exhibit significant bending without or with minimal failure of the fibers. Energy absorption is inefficient because of crack growth and the lack of fiber failure.
- 4. Local buckling mode, occurs when the fiber and/or matrix yield producing buckles in the tube, the distance between buckles is large compared to the thickness of the composite structure typical coupon of test are tubes. The energy absorption in this mode is a function of the wall thickness of the tube, and it increases as the thickness increases.

In a study by NASA, Hull[16] also performed experiments on circular crosssection tubes, considering the energy absorbed during the crushing phase as a critical performance metric, and identified two primary progressive failure modes:

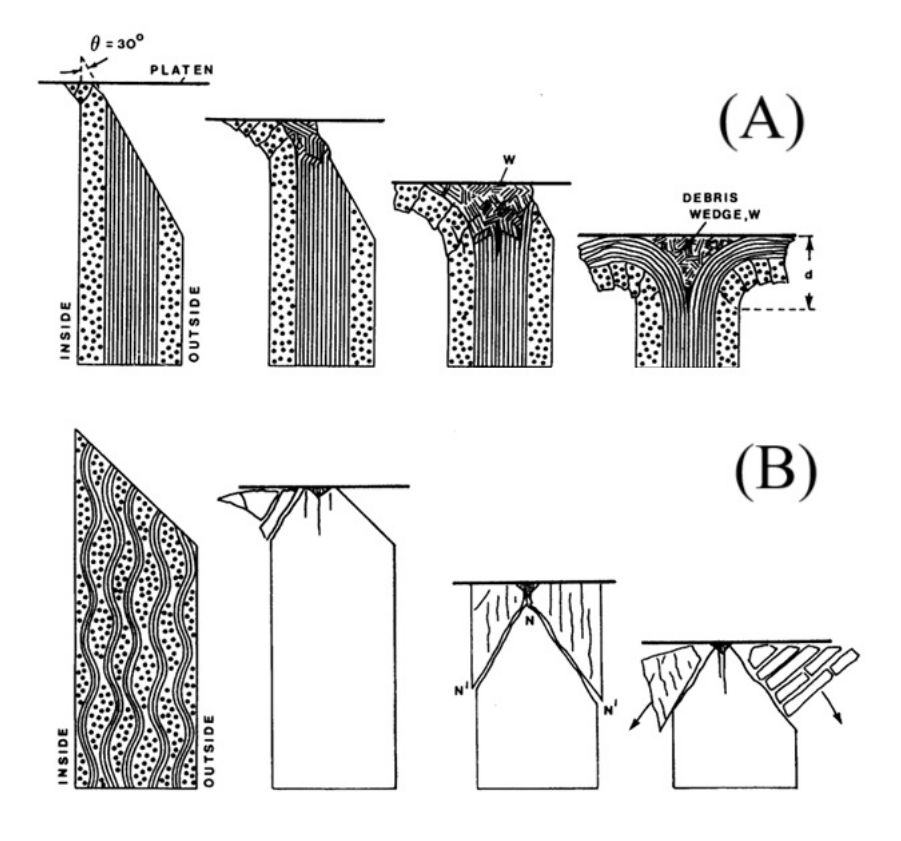


Figure 2.5: (A) Splaying mode, (B) Fragmentation mode [16]

- 1. Splaying mode, characterized by the delamination and outward bending of the lamina, as the composite structure undergoes axial compression. This mode describes interlaminar fractures and the lack of failure of the fibers or matrix, leading to the formation of longitudinal cracks initiated by a crush front. The energy absorption in this mode is the result of the friction between the crushing plate and the splayed layers and the resistance by the delamination of the composite structure, which leads to poor energy absorption performance.
- 2. Fragmentation mode also called tearing, describes an extensive breaking of the fibers and matrix cracking, leading to the material disintegrating into small debris. This mode is initiated by shear failures at the crush front, often triggered by a wedge, resulting in sharp edges that propagate additional fractures. This process continues with the formation of new wedges and subsequent material breakage until the composite is fully consumed. Fragmentation is considered highly effective for energy absorption because of the substantial damage and material separation involved.

The classification offered by previous authors is an effort that works towards the description of this phenomenon; however, because of the nature of the dynamic loads, it is a simplification of the problem and does not imply that only one of these modes occurs during one event, as can be seen in Figure 2.6, where two failure modes can occur in the same test or one can trigger the other.

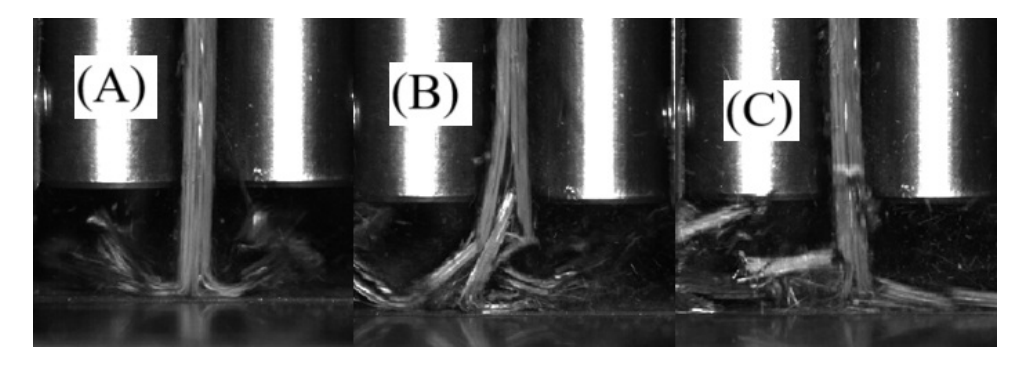


Figure 2.6: Carbon fiber-Polycarbonate flat specimen test (A) Beginning of the test showing a fragmentation failure mode (B) Delamination and local buckling mode (C) Fragmentation mode

2.4 Testing Methodologies for Crashworthiness for composite materials

Characterizing the behavior and mechanical properties of composite materials is a complex process due to the intrinsic nature of these materials; therefore, the industry relies on a combination of standards and best practices for testing and predicting the behavior of these materials. Several efforts have been made to standardize the dynamic load test for composite materials, which has resulted in the following:

- ASTM D7136 Drop Weight Impact Testing: This test employs a flat, rectangular composite specimen subjected to a controlled drop-weight impact using a hemispherical dart. It resumes the energy absorbed during the impact and the extent of the internal damage. Postimpact, the specimen is often subjected to a compression-after-impact (CAI) test, commonly referred to as Compression After Impact, to assess its residual mechanical performance [2].
- ISO 179-2 Charpy Impact Test: Designed to evaluate the material's resistance to impact loading, this method uses notched or unnotched specimens struck by a pendulum hammer. It records the energy absorbed during fracture and enables failure mode analysis, making it suitable for comparing the impact resistance across different composite formulations [18].
- ISO 6603-2 Instrumented Puncture Impact: This standard specifies a multi-axial impact test using a falling weight and a clamped specimen. This method provides detailed energy—time and force displacement records, allowing a complete analysis of energy absorption and failure progression [17].

Although these standards provide valuable insights into impact behavior and damage resistance, they are not specifically intended to evaluate the Specific Energy Absorption (SEA) of composite materials under crash-like conditions. SEA, defined as the energy absorbed per unit mass of material, is a key metric in crashworthiness applications. Despite the lack of a



Figure 2.7: Crashworthines test performed in tube specimens of different diameters. [14]

standardized SEA evaluation method, several researchers have proposed repeatable methodologies involving the controlled crushing of composite specimens, such as tubes or flat plates, to determine the SEA under quasi-static or dynamic loading [21], [28], [10].

2.4.1 Benchmark for Crashworthiness testing methods

Initial efforts to characterize the Specific Energy Absorption (SEA) of composite materials were conducted by NASA [8] and Hanagud [15] in the early 90s. These studies laid the groundwork for understanding the crushing behavior of composites. H

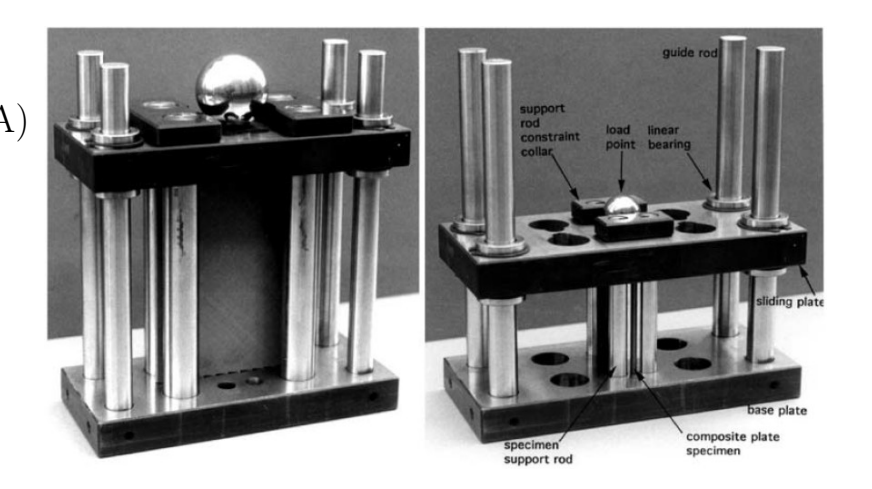


Figure 2.8: Test Fixture developed by NASA [8]

Hanagud [15] focused on sinusoidal geometries to

examine energy absorption under dynamic loads, highlighting the influence of geometry on fragmentation and deformation modes. Meanwhile, NASA [8] developed an anti-buckling test fixture tailored for flat plate specimens to isolate the failure mechanisms previously explained.

The choice of specimen geometry significantly influences SEA measurements. Self-supporting geometries are often preferred in crashworthiness testing because they eliminate the need for external anti-buckling supports. Tubes, cones, and sinusoidal coupons have emerged as traditional forms due to their geometric stability and resemblance to structural elements in transport applications. In particular, tubular specimens have been widely adopted in the automotive and aerospace sectors because they are easy to manufacture using conventional composite processing techniques and are inherently stable under axial loads. These configurations typically exhibit crush progression through local folding or frond formation, enabling the acquisition of reproducible SEA data. However, they also introduce complexities, such as hoop stress interactions and fiber constraints, which may mask the intrinsic energy absorption properties of the laminate [11].

In this context, Feraboli contributed significantly by developing a benchmark geometry, often referred to as the "Feraboli coupon" which enables the decomposition of the crush behavior into contributions from corners and flat segments. Beginning with square tubes, they ma-

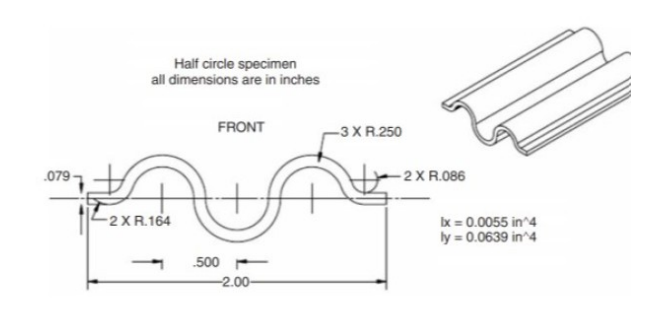


Figure 2.9: Feraboli Coupon. [12]

chined channel and corner section specimens to systematically evaluate how different geometric features (e.g., radius of curvature and flat segment width) affect the SEA. Through a comparative analysis of these derived geometries, Feraboli demonstrated that the corner regions, governed by tearing and fiber rupture, dominate the energy absorption, whereas the contribution from flat segments is notably lower and strongly dependent on anti-buckling

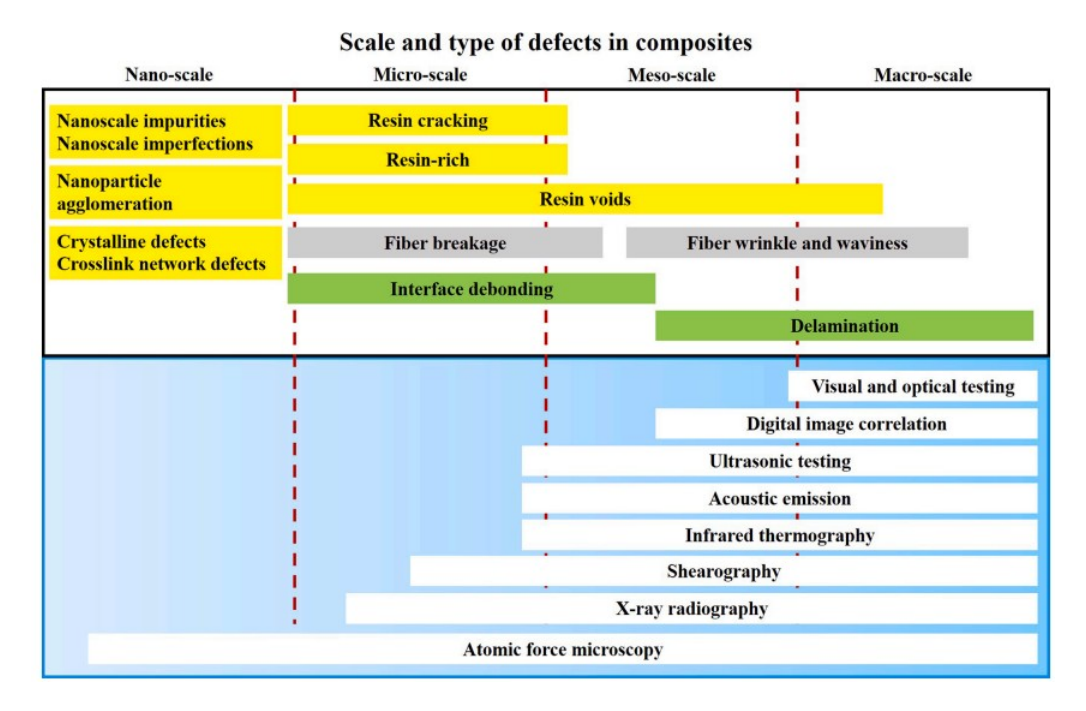


Figure 2.10: Scale and type of manufacturing defects on composite materials [13]

constraints. This approach allowed for a clearer interpretation of geometry-specific effects and established a modular strategy for crashworthiness assessment, which has since become a reference in experimental programs [11]

Despite their analytical clarity, complex geometries such as those of Feraboli coupons have practical limitations that hinder their widespread adoption in industrial test standards. Tailor-made molds must often be fabricated to achieve the precise dimensions and curvature transitions required for consistent testing. Moreover, the anisotropic and process-sensitive nature of composite materials means that small deviations in the lay-up, resin content, or curing conditions can lead to significant variability in SEA results. Flat coupons, although artificially constrained by fixtures, remain attractive for preliminary material screening because they are cheaper and easier to manufacture, and defects and geometry bias can be neglected if the failure modes are isolated. As shown by subsequent adaptations of the NASA fixture and the development of modified rigs by Feraboli, the test setup itself can profoundly influence the observed failure modes and energy dissipation patterns [9], [20].

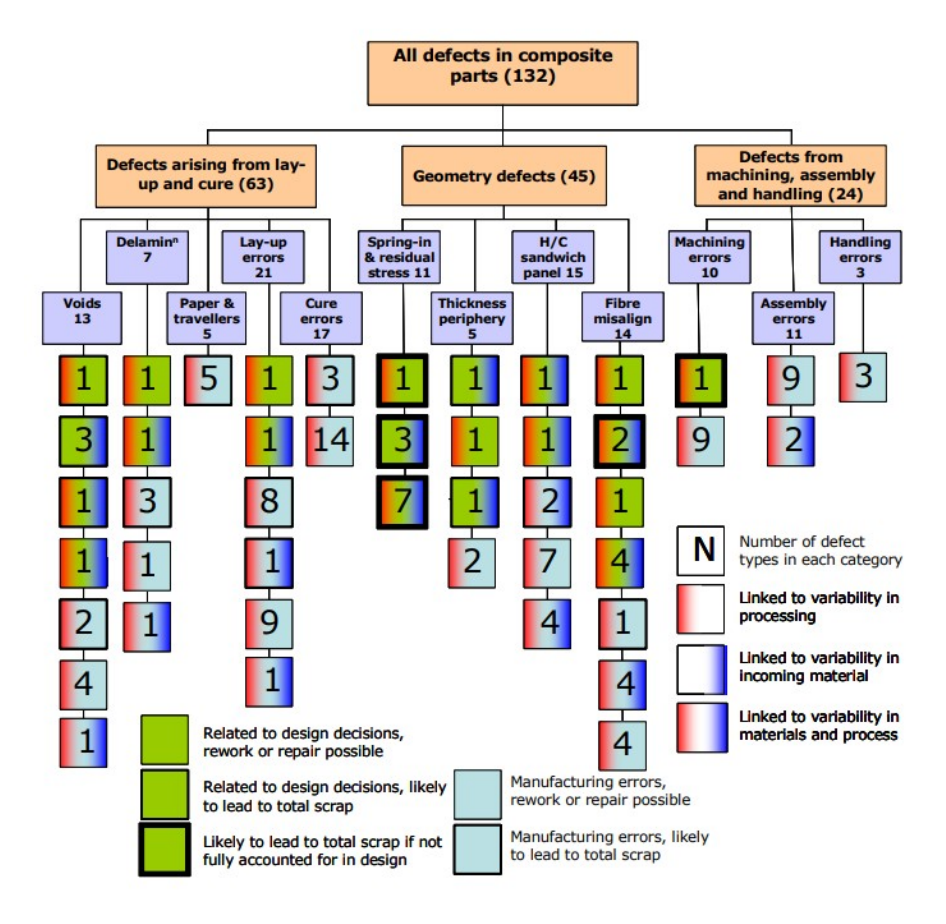


Figure 2.11: Taxonomy of defects in composite materials as proposed by Potter [26]. The classification highlights the relationship between manufacturing processes, geometry, and defect formation.

As highlighted by Potter [26], defects in composite materials can arise from three main categories, as shown in Figure 2.11. As shown in the Potter study, geometry is a key parameter in the defects and performance of the composite materials. Variations in thickness along curved regions can lead to non-uniform stress distributions, resulting in inconsistent mechanical behavior and potential misinterpretation when characterizing the structural layout of the composite. Coupons that integrate this geometry bias can affect the design process by an inaccurate measurement of the SEA that a material can withstand. In contrast, flat coupons minimize these sources of variability because of their geometric simplicity and ease of fabrication. As such, they offer a more controlled and reliable means of assessing the intrinsic energy absorption capacity of a material, particularly in the early stages of testing or when isolating material-level phenomena.

Correspondingly, Yutong [13] explained how the manufacturing process

plays a critical role in the performance of composite materials. In this line of reasoning, residual stress related to the curation process, such as pressure uniformity, thermal stability, or geometry, can significantly influence the characteristics of the final material, leading to the formation of multiscale defects on the fibers, layers, or laminae of the composite materials, as shown in Figure 2.10. Therefore a great consideration must be taken into consideration when designing the parameters for the manufacturing process in order to keep the desired characteristics of the material.

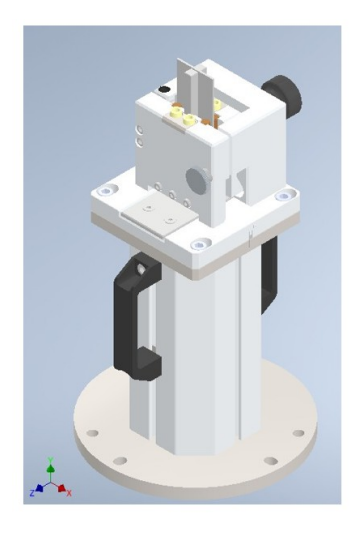
In summary, the existing standardized tests do not cover the SEA in great detail, and the current benchmarking techniques for crashworthiness evaluation provide great insight into the SEA performance of composite materials but suffer from two critical shortcomings **geometry dependency and fixture interference**. Self-supporting coupons, such as tubes or sinusoidal specimens, intrinsically couple the performance with geometric effects. Conversely, Flat coupons exhibit unrealistic failure modes (e.g., global buckling) due to inadequate constraint design, leading to an underestimation of the SEA. These limitations underscore the need for a methodology that decouples the material behavior from geometric biases while replicating the failure mechanisms observed in real-world corrugated structures. Lorenzo Vigna's PhD work [28] addressed this gap by developing a novel flat-coupon testing framework capable of inducing splaying and tearing failures—modes typically reserved for complex geometries—through a purpose-built anti-buckling fixture.

2.5 Non-Standard Test Methodologies and Innovations

Traditional state-of-the-art methodologies for the assessment of SEA typically rely on self-supported structures. As previously explained, these methodologies exhibit certain intrinsic limitations due to their inherent nature. Consequently, flat coupon tests have emerged as a de facto non-traditional methodology for evaluating crashworthiness. To address this gap, Vigna improved the existing non-standard testing methodology that isolates the intrinsic dominant failure modes of **Splaying and Tearing (Fragmen-**

tation) in flat coupons [28]. This innovation addresses the key limitations of current crashworthiness testing practices by reconciling geometric simplicity with the ability to mimic the failure dynamics typical of real-world structures.

To achieve this objective, Vigna developed an innovative methodology for the assessment of Specific Energy Absorption (SEA) by evaluating flat coupons under dynamic loads defined by an impact test machine, where the parameters for testing are defined by the energy of impact as a function of the weight and velocity of the tester [28]. The designed fixture holds the coupon by means of 6 bronze pillars, which can vary in length, to constrain the coupon to a certain failure mode. As shown in Figure 2.12 the fixture clamps the coupon at a defined force, while the copper is used to make the friction forces generated at the clamping negligible; the testing probe impacts the coupon at the upper part. This fixture allows for the use of two setups, enhancing the two main failure modes of composite materials:



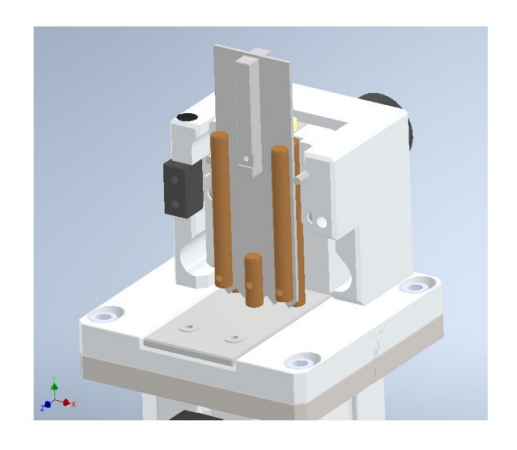


Figure 2.12: Flat coupon fixture, left figure presents the assembly of the fixture and right figure presents the fixture without the closing gate allowing the view of the coupon.

- Splaying failure mode, by not constraining the crashing contact part of the coupon, thereby enhancing interlaminar delamination and the outward peeling of plies, which are characteristic of the splaying failure mode. The energy absorption in this scenario is primarily attributed to interface friction and interlaminar failure.
- Tearing failure mode, conversely this setup fixes three pillars con-

straining the displacement of the material forcing the fiber failure and progressive matrix cracking, thereby triggering the tearing failure mode, this results in high energy absorption.

As illustrated in Figure 2.13 the standardized flat coupon offers repeatability and modularity in terms of the testing desired to be performed because there is a single geometry for both types of setups for the fixture. The geometry exhibits a trigger made of triangles, which allows the coupon to initiate energy absorption, as described by Vigna [28]. The influence of the trigger is a critical factor in the transition phase from static to dynamic load.

By capturing the SEA performance of a material under both failure modes, it is possible to estimate the behavior of more complex structural configurations, such as sinusoidal or tubular coupons.

The literature provides a comprehensive foundation for the failure mechanics of composite materials under dynamic loading, delineating primary energyabsorbing modes such as transverse shearing, lamina bending, splaying, and fragmentation. The critical role of Specific Energy Absorption (SEA) as a principal metric for evaluating crashworthiness in weight-sensitive applications has been established. Notwithstanding these advancements, a persistent challenge in the field is the absence of a stan-

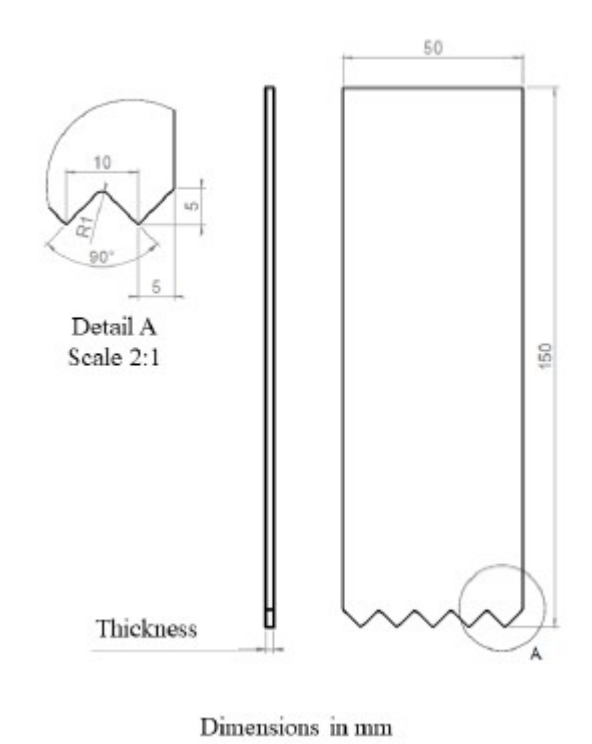


Figure 2.13: Technical drawing for flat coupon.

dardized and practical methodology for extrapolating the crash performance of complex structural geometries from fundamental material-level data.

Conventional standardized tests (e.g., ASTM D7136, ISO 179-2) are primarily designed for damage resistance characterization and do not directly

facilitate SEA quantification for crashworthiness designs. Conversely, benchmark methodologies employing self-supporting geometries, such as tubes and corrugated coupons, intrinsically couple geometric effects with material performance, thereby obscuring the intrinsic energy absorption properties of the laminate. While innovative fixtures, such as those developed by NASA, have provided valuable insights by deconstructing geometric contributions, they often involve complex specimen preparation and have not been widely adopted for rapid material screening and preliminary designs.

Chapter 3

Experimental Methodology

3.1 Test Setup

The experiments detailed in this document were conducted in collaboration with ITW Test and Measurement Italia s.r.l. - Instron CEAST division at their facility in Pianezza, Italy. The instruments and tools used were provided by the company. Dynamic load tests were conducted using an Instron 9450 drop-weight impact testing machine, as shown in The Drop Tower was Figure 3.1. equipped with a standard tup holder, in which the weight could be loaded to achieve the desired load for testing. The force transducer used was a 90 kN strain gauge tup, mounted

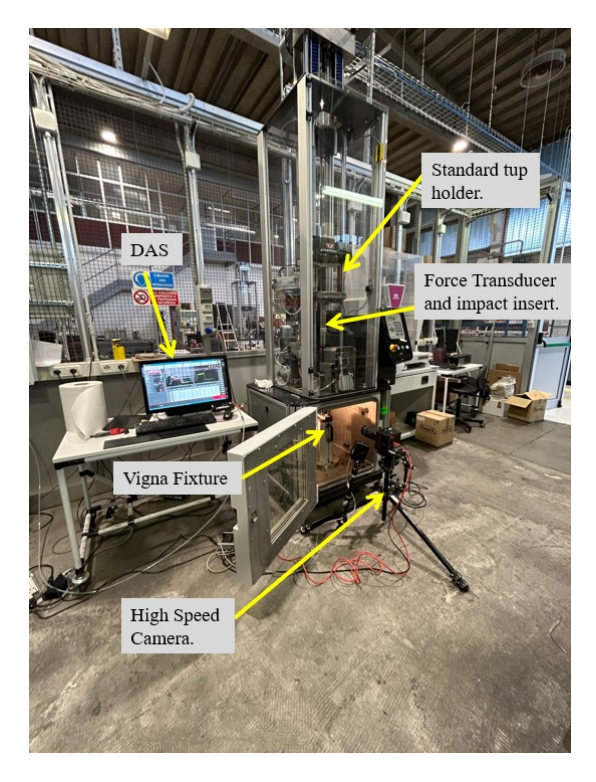


Figure 3.1: Drop Tower Setup for dynamic load tests

with a flat-faced insert of 70 [mm] in diameter. The main parameters of the machine are listed in Table 3.1.

To record the output of the experiments, there were two outputs: the data acquisition system (DAS) recorded the force as a function of time recorded by the force transducer, while a fast speed camera (FASTCAM Mini AX200)

Parameter	Value	Units
Energy Range	0.59 - 1800	[J]
Impact velocity	0.77 - 24	$[m \cdot s^{-1}]$
Mass Range	2.0 - 70.0	[kg]
Drop height	0.03 - 29.4	[m]
Mass increments	0.5	[kg]
Data Collection Rate	1	[MHz]

Table 3.1: Drop Tower technical specs.

with a sensor resolution of 1024×1024 pixels at 6400 [fps] and a maximum shutter speed of 900 [kfps] used to observe the failure mechanism. Both systems are triggered by a drop tower photocell that measures the impact velocity at a position defined by the user; the trigger must be activated just before the impact insert touches the specimen. Finally, a holding fixture was designed and manufactured using a 3D printer for the sinusoidal coupons. The main functionality was to hold the coupon from moving while the dynamic test was being performed, as shown in Figure 3.2.



Figure 3.2: Sinusoidal coupon holder.

3.2 Coupons and Materials

The coupons tested were manufacture, cure and provided by the Leibniz-Institut für Verbundwerkstoffe GmbH (IVW) according to specification of the Geometry described in the figure 2.13 for the Flat coupons while the

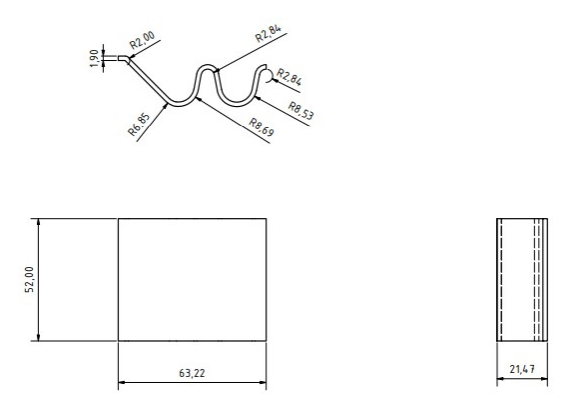


Figure 3.3: Technical drawing for the IVW coupon geometry.

sinusoidal coupons followed the internal (IVW) design 3.3, in total there were 6 type of composite materials evaluated varying the three main parameters fibers composition, Matrix material and disposition of the fibers, here described in deep detail each of the materials:

Material	Fibers Material	Matrix Material	Fibers Layup	Density $[g \cdot cm^{-3}]$
CF-PC	Carbon Fiber	Polycarbonate	$(90/0)_6$	1.44
CF-PA6	Carbon Fiber	Polycaprolactam / Nylon 6	$(90/0)_6$	1.49
CF-PA66	Carbon Fiber	Nylon 66	Woven - 6 Layer	1.55
CF-E3-150	Carbon Fiber	E3-150 - Epoxy	Woven - 6 Layer	1.37
GF-PP	Glass Fiber	Polypropylene	$(90/0)_6$	1.71
GF-TEPEX	Glass Fiber	Thermoplastic Polymers	Woven - 6 Layer	1.66

Table 3.2: Properties of the investigated composite materials.

The coupons were prepared by measuring their characteristics, specifically their dimensions and weights. for the coupons for which the matrix was made of polyamide (Nylon 6 and Nylon 66). Because the water content affects the mechanical properties of the material, an additional procedure of drying out the coupons was performed using an oven with the capability of operating at a controlled vacuum until the measured weight of the specimens changed by less than 0.05 [%] between two consequent drying cycles.

The coupons exhibited a trigger characterized by a buffer zone of 5 [mm] and a set of equilateral triangles with a base of 5 [mm]. For the flat coupons, this trigger was manufactured when the coupons were water-cut from the plates, whereas the trigger for the sinusoidal coupons was cut using a hand-saw.







Figure 3.4: From left to right: (a) The oven and vacuum pump, (b) Coupons inside the drying process and (c) Balance and weight of the specimens

3.3 Test Procedure

The primary objective of this study was to evaluate six different types of composite materials by varying the three main parameters that constitute them. To achieve this, a test plan was developed in collaboration with IVW, the institution responsible for providing and manufacturing the coupons, as detailed in Table 3.3:

Material	Splaying Test	Tearing Test	Corrugated IVW	Corrugated Instron
CF-Epoxy	5 Flat Coupons	5 Flat Coupons	-	5 Coupons
	Tested at Instron	Tested at Instron		
CF-PA6	5 Flat Coupons	5 Flat Coupons	5 Coupons	5 Coupons
	Tested at Instron	Tested at Instron		
CF-PA66	5 Flat Coupons	5 Flat Coupons	-	5 Coupons
	Tested at Instron	Tested at Instron		
CF-PC	5 Flat Coupons	5 Flat Coupons	5 Coupons	-
	Tested at Instron	Tested at Instron		
GF-TEPEX	5 Flat Coupons	5 Flat Coupons	-	5 Coupons
	Tested at Instron	Tested at Instron		
GF-PP	5 Flat Coupons	5 Flat Coupons	5 Coupons	5 Coupons
	Tested at Instron	Tested at Instron		

Table 3.3: Test plan for materials and institutions of testing.

It is important to clarify that the corrugated coupons tested at IVW differed in geometry from those tested by Instron. However, the differences were not substantial, as the primary distinction was that the coupon used by Instron was an IVW specimen cut in half. This variation was due to the testing setup and the equipment available at each institution. Consequently,

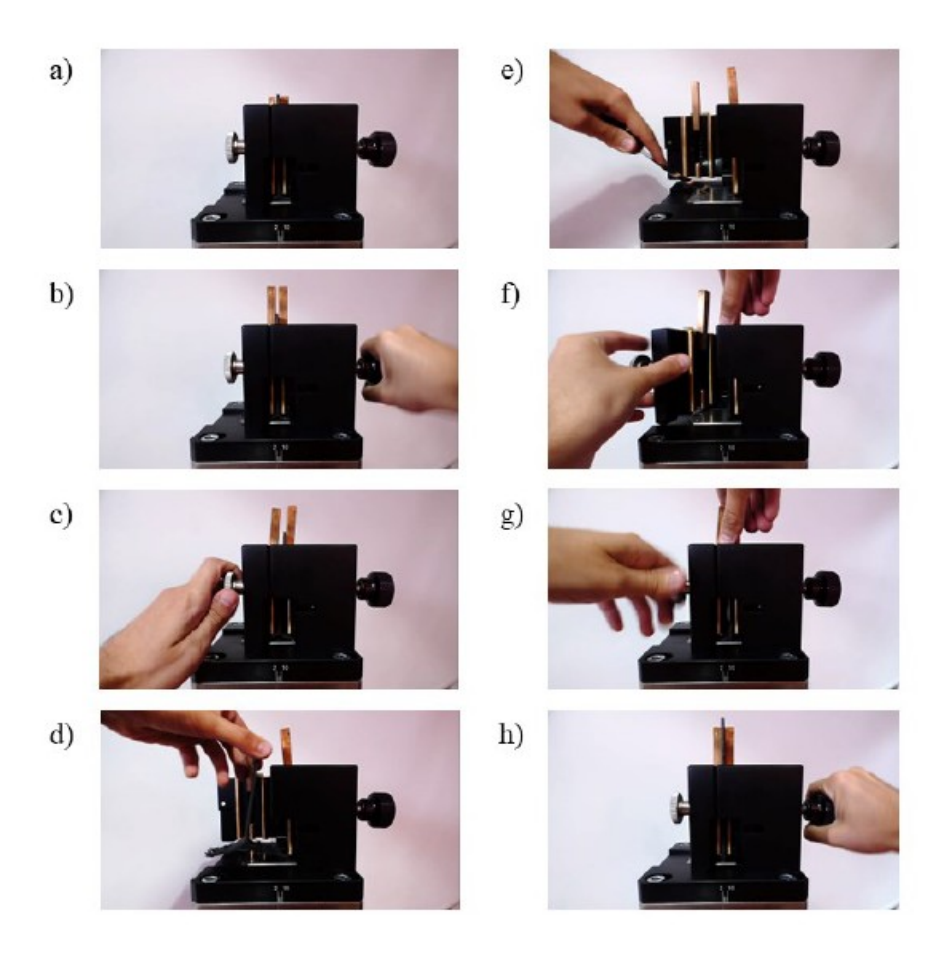


Figure 3.5: Process for loading the Vigna Fixture, a) fixture after the end of the test; b) unclamping the specimen rotating the handle on the right; c) opening the door on the left side; d) extraction of the specimen; e) removal of the debris and powders; f) positioning a new specimen and door closing; g) fastening the door using the handle on the left side; h) clamping the specimen using the torque-limited handle on the right side.[28]

the CF-PA6 and GF-PP materials underwent dual testing at both institutions to ensure that the results were statistically reproducible. Owing to a lack of material, the corrugated coupons for polyamide PA66 were manufactured using PA6 because the mechanical properties are similar; thus, it was assumed that the behavior of the final composite material properties were comparable.

As described by Vigna [28] the test procedure for loading the fixture for flat coupons can be observed in Figure 3.5 For the flat coupons, this procedure was followed when testing the Splaying and Tearing procedures, while for the corrugated coupons, they were mounted on the fixture described in Figure 3.2, and then the drop tower was ready for the test.

Finally, the parameters for testing are described in Table 3.4, the main

fixed parameter of the testing procedure was the velocity of impact, while the mass varied according to the amount of material derived from the crosssection of the specimen. The main objective is to achieve a good stable phase after the trigger is surpassed to finely characterize the SEA and not be influenced by velocity.

Material	Splaying Test	Tearing Test	Corrugated IVW	Corrugated Instron
CF-Epoxy	$7.47 \ [m \cdot s^{-1}]$	$7.47 \ [m \cdot s^{-1}]$	-	$7.15 \ [m \cdot s^{-1}]$
	10.750 [kg]	10.750 [kg]		15.750 [kg]
	300 [J]	300 [J]		400 [J]
CF-PA6	$7.47 \ [m \cdot s^{-1}]$	$7.47 \ [m \cdot s^{-1}]$	$7.56 \ [m \cdot s^{-1}]$	$7.47 \ [m \cdot s^{-1}]$
	10.750 [kg]	10.750 [kg]	59.46 [kg]	18.000 [kg]
	300 [J]	300 [J]	1922 [J]	502 [J]
CF-PA66	$7.47 \ [m \cdot s^{-1}]$	$7.47 \ [m \cdot s^{-1}]$	-	$7.47 \ [m \cdot s^{-1}]$
	10.750 [kg]	10.750 [kg]		21.000 [kg]
	300 [J]	300 [J]		585 [J]
CF-PC	$7.47 \ [m \cdot s^{-1}]$	$7.47 \ [m \cdot s^{-1}]$	$7.5 \ [m \cdot s^{-1}]$	-
	10.750 [kg]	10.750 [kg]	57.0 [kg]	
	300 [J]	300 [J]	1603 [J]	
GF-TEPEX	$7.47 \ [m \cdot s^{-1}]$	$7.47 \ [m \cdot s^{-1}]$	-	$7.47 \ [m \cdot s^{-1}]$
	10.750 [kg]	10.750 [kg]		10.750 [kg]
	300 [J]	300 [J]		300 [J]
GF-PP	$7.47 \ [m \cdot s^{-1}]$	$7.47 \ [m \cdot s^{-1}]$	$7.5 \ [m \cdot s^{-1}]$	$7.47 \ [m \cdot s^{-1}]$
	10.750 [kg]	10.750 [kg]	35.0 [kg]	10.750 [kg]
	300 [J]	300 [J]	984 [J]	300 [J]

Table 3.4: Test parameters for the test plan.

3.4 Data Processing and Analysis

The Instron Bluehill Universal software integrated into the drop tower machine, where the testing procedures were performed, was used to plot and export the force signals. The output data from the force transducer are the force in [N] and time in [ms] at a 1 [MHz] rate. The DAS starts to record data as soon as the trigger is activated; however, the software defines the starting point as 0, which is when the impact insert touches the coupon. With this information, the software computes the Velocity, Energy, Displacement and Impulse, as described in the following formulas:

$$\ddot{z_{(t)}} = g - \frac{F_{(t)}}{m} \tag{3.1}$$

$$\dot{z_{(t)}} = g \cdot t - \frac{F_{(t)} \cdot t}{m} + v_0$$
 (3.2)

$$z_{(t)} = g \cdot t^2 - \frac{F_{(t)} \cdot t^2}{m} + v_0 \cdot t \tag{3.3}$$

$$E_{(z)} = \int F_{(t)} dz \tag{3.4}$$

$$J_{(t)} = \int F_{(t)} dt (3.5)$$

where:

- $z_{(t)}$ Acceleration at impact insert
- \bullet g Gravity acceleration
- \bullet $F_{(t)}$ Force measure by the force transducer
- m Impact mass
- \bullet t time
- v_0 Impact velocity
- \bullet $E_{(z)}$ Cumulative energy transferred
- $J_{(t)}$ Momentum the force imparts.

The rationale for data processing and analysis was to comprehend the data output derived from the testing of materials and to assess whether the obtained data followed a specific trend or were adjusted to a particular fitting model. Therefore, MATLAB was employed for data processing, and scripts were developed to address these requirements. As illustrated in the diagram presented in Figure 3.6, the initial task involves filtering the white noise present in the test data. To achieve this, a combination of a Savitzky-Golay smoother and a bandstop filter was applied in MATLAB. The Savitzky-Golay filter effectively reduces high-frequency noise while preserving essential

features by utilizing a large window to capture slow trends. Subsequently, the bandstop filter removes specific frequency bands to eliminate any remaining interferences.

Following the removal of white noise from the data, the objective was to assess the Specific Energy Absorption (SEA). For this purpose, the input comprised CSV files obtained from the drop tower and the parameters of the specimen measured during the preparation phase. The methodology for evaluating the SEA is described in Equation 2.2. As the impact insert was subjected to reaction forces from the coupon resisting the impact, it experienced deceleration. This test recorded the variation in reaction forces as the velocity changed, prompting an inquiry into whether the velocity influences the behavior of the SEA. A detailed explanation is provided in Chapter 4.

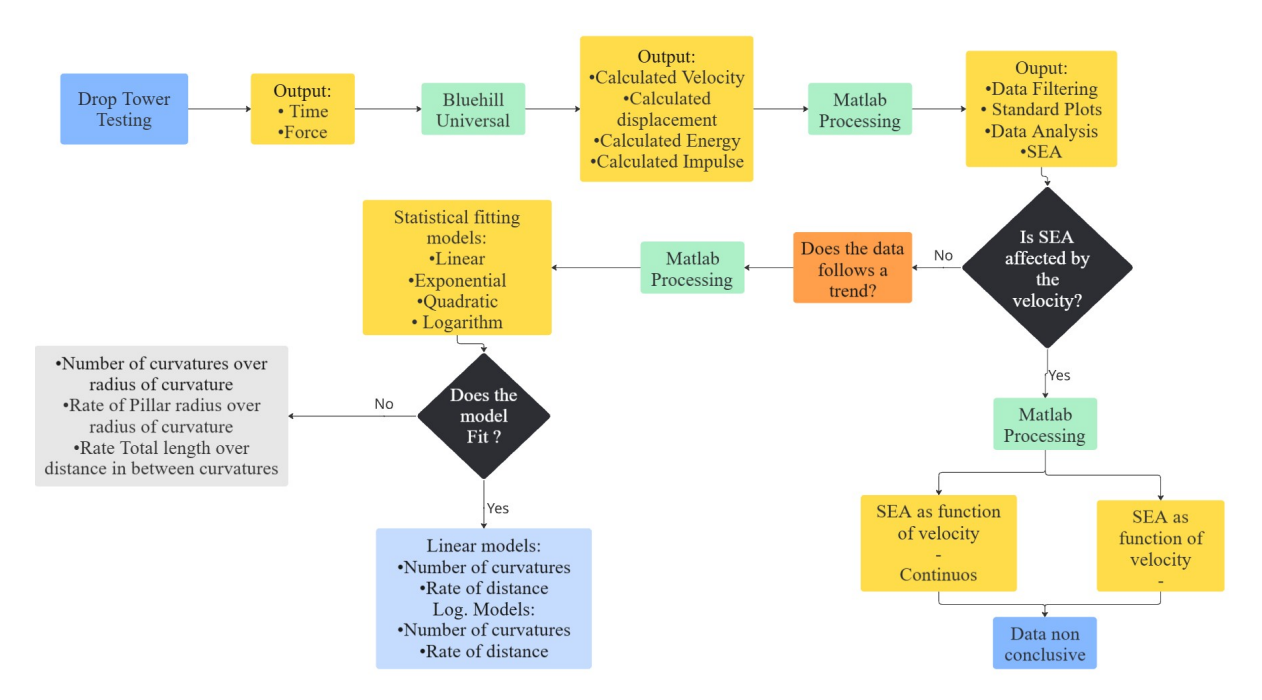


Figure 3.6: Diagram for data analysis of the Flat and corrugated coupons.

To determine whether the coupon data exhibited a specific trend, several statistical fitting models were employed to determine the existence of a correlation between the flat and corrugated coupons. The primary challenge in relating flat coupons to corrugated coupons is the absence of a common variable that facilitates their comparison. Therefore, the following parameters were considered for comparison:

- 1. Number of curvatures
- 2. Rate of number of curvatures and radius of curvature
- 3. Rate of Pillar radius over radius of curvature
- 4. Rate of total length over distance in between fixing points
- 5. Rate Total length over distance in between curvatures

All parameters were subjected to statistical fitting models to assess their suitability within the Linear, Exponential, Quadratic, and Logarithmic frameworks. As elaborated in the subsequent chapter, only two parameters were significant for data fitting. These data fitting parameters were used for the prediction models. The reason for creating This analysis was performed to understand the main parameters that govern the behavior of composite materials.

3.5 Validation and Prediction

Given that the tests were developed by two distinct institutions and conducted under varying geometrical conditions, there is a concern regarding the reproducibility of the data being compared. To address this issue, as previously explained, two materials were tested twice at both institutions to facilitate statistical analysis for comparison. The statistical tool employed for this comparison was a statistical power analysis, Type I Error (α) , and Type II Error (β) , with the primary objective of verifying the statistical validity of the comparison between the two datasets. The statistical distribution employed was the Student's t-distribution, as the sample size was fewer than 30. The observations were independent of one another, the same material was tested across different machines and geometries, and it was assumed that the data followed a normal distribution. The test requires a significance level defined by the researcher fixing one type of error (α) or (β) . The non-fixed significance level is a function of the degrees of freedom, standard deviation, and statistical distribution. The analysis requires a null

hypothesis (h_0) and an alternative hypothesis (H_1) capable of accepting only one of the hypotheses.

- Type error I Rejecting the null hypothesis (H_0) when it is actually true.
- Type error II Failing to reject the null hypothesis (H_0) when it is actually false.

Following the validation and statistical assessment of the experimental data to ensure consistency across different testing conditions, the focus of this study shifted toward the development of predictive models for Specific Energy Absorption (SEA). The construction of these models is grounded to accurately predict the Specific Energy Absorption (SEA) of corrugated coupons using linear and logarithmic regression models departing from the data obtained at the Splaying and Tearing for the two models (number of curvatures and rate of distance) parameters derived from curve-fitting procedures applied during the data processing phase, which demonstrated strong correlations between the flat and corrugated coupons. By exploiting these empirical relationships, the objective is to formulate predictive frameworks capable of estimating the energy absorption of complex geometries under dynamic loading conditions, departing from simpler flat coupons to more complex geometries.

The methodological framework guiding the construction of the predictive models is depicted in Figure 3.7, which summarizes the logical sequence of the steps undertaken throughout the analysis. The models were implemented using a MATLAB script, resulting in a single output value that determined the most probable Specific Energy Absorption (SEA) value for a corrugated coupon. In this study, this value was considered as the predicted mean of SEA. Given the complex behavior of composites and the potential variability in performance across tests, establishing a prediction range is more appropriate. To achieve this, predicting the standard deviation is necessary in these predictive models, and two primary models were developed for this purpose.

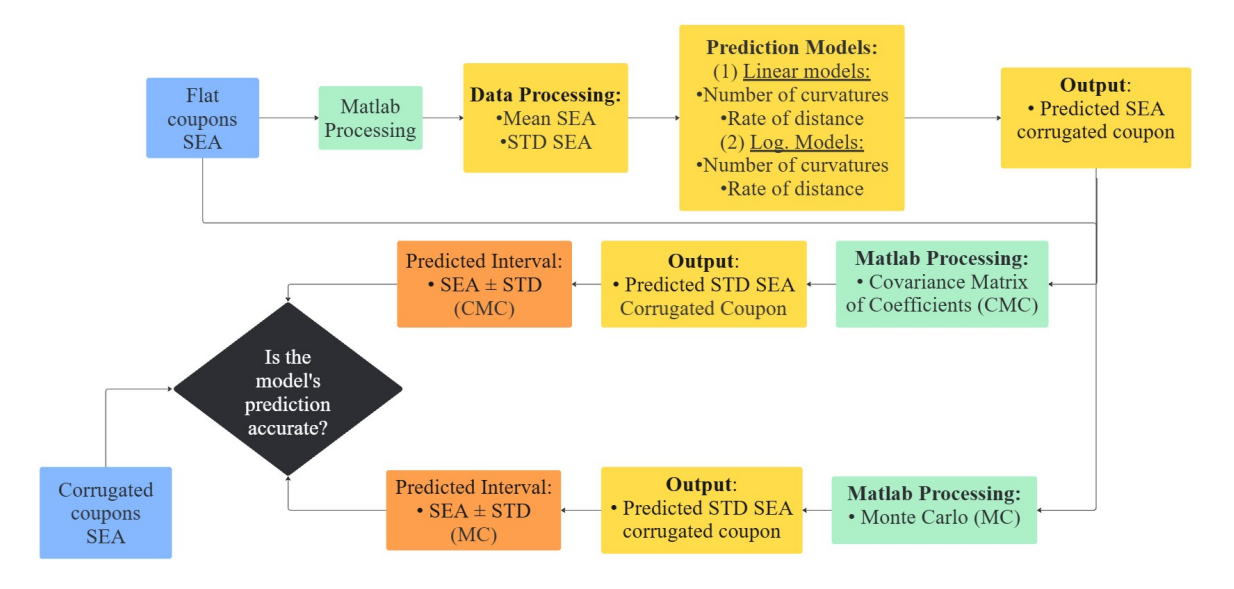


Figure 3.7: Diagram for building the prediction models

- 1. Covariance Matrix of Coefficients (CMC) This method is grounded in regression analysis, where the covariance matrix represents the variances and covariances of the estimated coefficients. It provides a comprehensive perspective on how a change in one coefficient may be related to changes in the other coefficients. Given the complex behavior of composite materials, the CMC is a valuable statistical tool for constructing confidence intervals.
- 2. Monte Carlo Method (MC) This stochastic model offers an alternative to traditional analytical approaches by conducting 10,000 runs through random sampling predictions of SEA to a fitted regression model. Once the input data were processed, the distribution of the confidence interval was generated. It is important to note that this model accounts for nonlinearities and complex interactions that may not be captured by analytical methods.

Following the construction of models for predicting the SEA within a specified range, it is essential to evaluate their efficacy in accurately predicting the SEA of different sinusoidal specimens. This framework is illustrated in Figure 3.8, which shows the evaluation process of the models. This evaluation employed the same methodology used for validating the data from both institutions, as the parameters of both flat and corrugated coupons aligned

well with the hypothesis testing using the t-distribution.

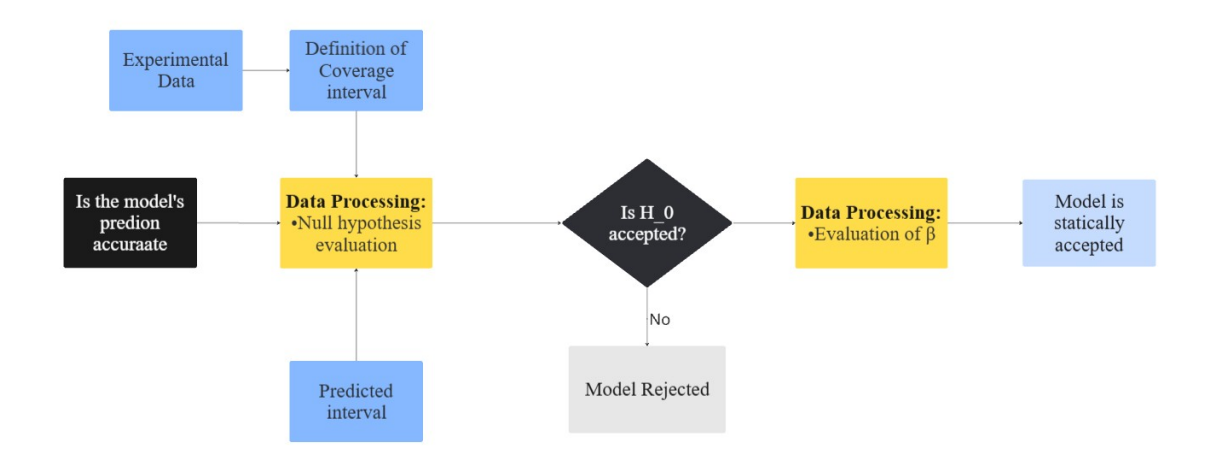


Figure 3.8: Diagram for the statistical evaluation of the models.

To perform this hypothesis testing, the computation of a t-student test is needed to assess if it falls into the confidence of interval of (α) and (β) ; for this, the following formula is used:

$$t = \frac{(\bar{x} - \mu_0)}{s} \cdot \sqrt{n} \tag{3.6}$$

where:

- \bullet t t-student test
- \bullet \bar{x} Predicted SEA mean
- μ_0 Experimental SEA mean
- \bullet s Predicted STD
- \bullet *n* Sample size

3.6 Limitations

Despite the extensive efforts undertaken in this study, certain assumptions are inherently linked to the methodology employed and must be considered when interpreting the results obtained. These limitations are as follows:

• Small Sample Size - The number of specimens tested per configuration limits the statistical power of the analysis. With small sample sizes, the

variability in the composite behavior may not be fully captured, reducing the confidence in the extrapolations.

- **Fixture Influence** Although the Testing fixture for flat specimens was designed to isolate failure modes, its constraint conditions may still introduce boundary effects, especially in flat coupon tests, which can affect failure mode development and energy dissipation.
- Inter-Institutional Variability Tests were performed at different institutions (IVW and Instron), with slight differences in equipment and coupon geometries. Although statistical tests were used to assess reproducibility, subtle procedural variations may still affect the results.
- Assumption of Normality Statistical comparisons and predictions were based on the assumption of normal data distribution. Given the small sample sizes and material variability, this assumption may not always be valid.
- Prediction Model Generalization The prediction models (linear and logarithmic regressions) rely on curve fitting from a limited data set and geometry. Their extrapolation to broader configurations may not be reliable without further validation.

Chapter 4

Experimental Testing and Analytical Framework

This chapter describes the experimental findings derived from Crashworthiness assessments conducted on six distinct fiber-reinforced composite materials. Each material was evaluated under three specific configurations—splaying, tearing, and corrugated—to identify the predominant failure mechanisms and assess the energy absorption characteristics under dynamic loading conditions. The resultant data were analyzed using force-displacement and cumulative energy transfer curves, offering insights into the mechanical response of the materials and the impact of the test setup and geometry. The subsequent sections provide a detailed description and interpretation of these results, material by material, to establish a coherent framework for evaluating the Specific Energy Absorption (SEA) and failure modes.

4.1 Crash testing

In accordance with the methodology outlined in chapter 3, the dynamic testing procedure was conducted. The results and any occurrences during the experimental testing are detailed for each material. Because all the tests were independent of each other, the testing conditions are presented in detail.

4.1.1 CF-PA6

For the CF-PA6 material, the drying process was performed before testing the coupons to ensure that the water absorption of the materials did not influence the performance of the composite; the drying process and methodology are explained in detail in the previous chapter.

Splaying

Figure 4.1 shows the force as a function of displacement for CF-PA6 under the splaying setup. The curve exhibited a sharp initial peak, followed by a relatively steady plateau, indicating a stable progressive crushing behavior after the trigger zone. Two Coupons PA6-F-1 and PA6-F-3, exhibited an underperformance behavior in the stable progressive region.

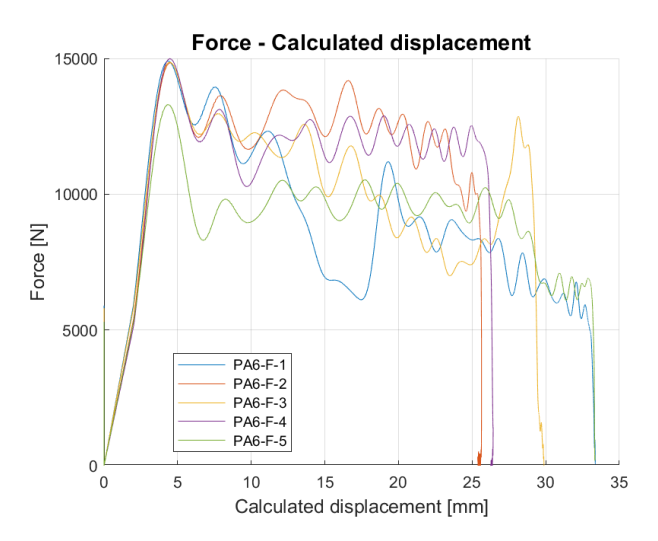


Figure 4.1: Force as function of displacement results for Splaying setup of CF-PA6.

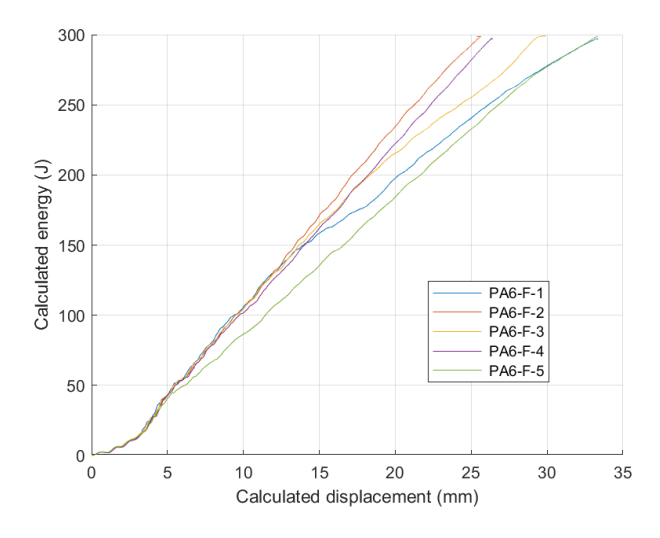


Figure 4.2: Cumulative energy transferred as function of displacement results for Splaying setup of CF-PA6.

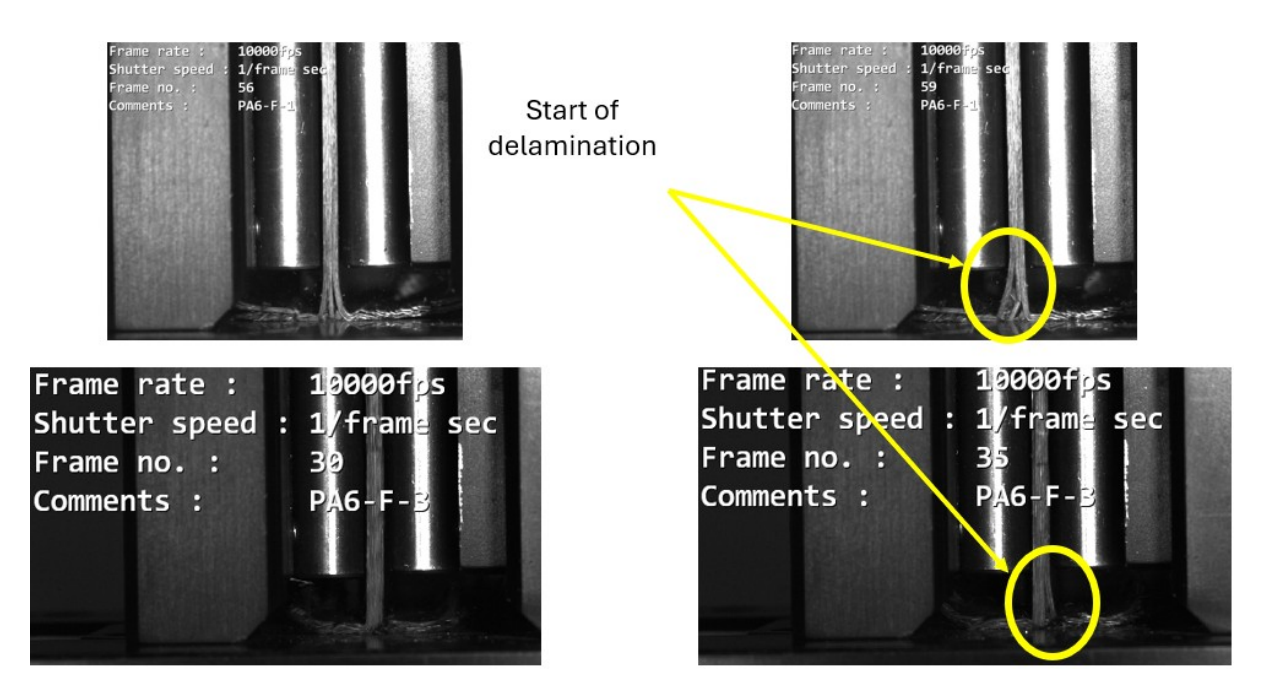


Figure 4.3: Delamination failure mode on coupons PA6-F-1 (upper part) and PA6-F-3 (lower part).

Figure 4.2 illustrates the cumulative energy absorbed, which increases steadily, confirming the consistent energy dissipation during deformation. In this figure, the moment at which the coupons (PA6-F-1 and PA6-F-3) underperformed can be visible. This occurred because a delamination failure mode occurred during the testing, as shown in figure 4.3 at approximately 15 mm and 17 mm, respectively, the composite suffered delamination of a lamina followed by a sudden breakage, allowing the SEA to return to the original performance.

Tearing

Figure 4.4 shows the force as a function of displacement for CF-PA6 under the Tearing setup. The curve exhibited a sharp initial peak, followed by a relatively steady plateau, indicating a stable progressive crushing behavior after the trigger zone. Two Coupons PA6-F-7 and PA6-F-8, exhibited an abrupt stop before in the displacement of the total length of the coupon and as described in the figure 4.5 at this specific points the SEA behavior of the material abruptly changes as it can be explain due to a buckling failure mode occurred in the upper part of the coupon, described in the figure 4.6

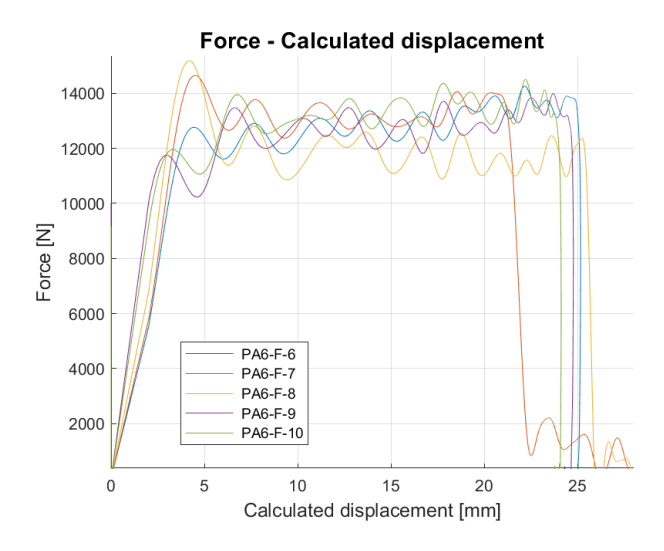


Figure 4.4: Force as function of displacement results for Tearing setup of CF-PA6.

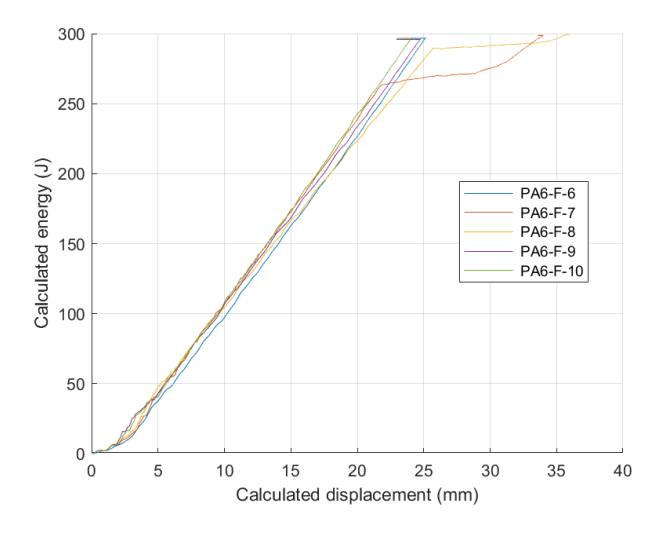


Figure 4.5: Cumulative energy transferred as function of displacement results for Tearing setup of CF-PA6.

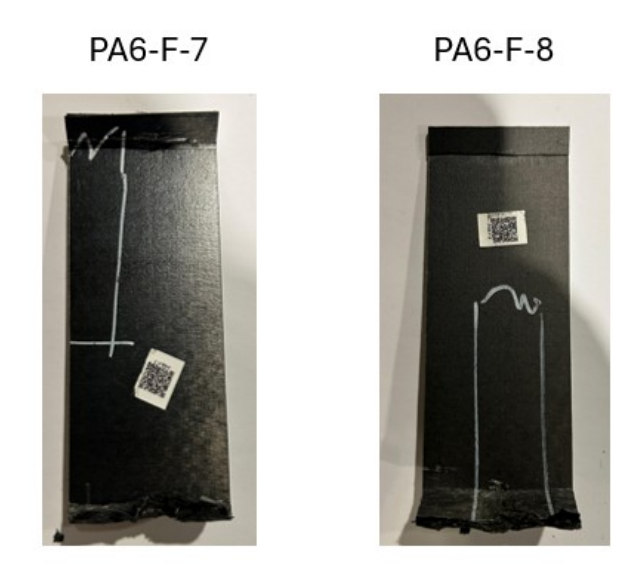


Figure 4.6: Buckling failure of the upper part of coupons PA6-F-7 and PA6-F-8

Corrugated

Figures 4.7 and 4.8 show the behavior of corrugated specimens. The force-displacement response was characterized by oscillations, suggesting alternating local failure modes and stress redistributions. The force was higher than that of both flat configurations, due to a higher cross-sectional profile compared to the flat coupons; during this test, all coupons were in order.

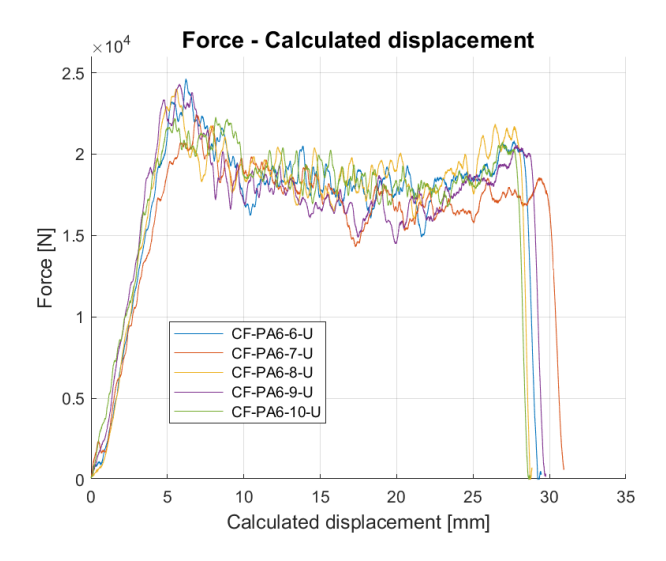


Figure 4.7: Force as function of displacement results for corrugated coupons of CF-PA6.

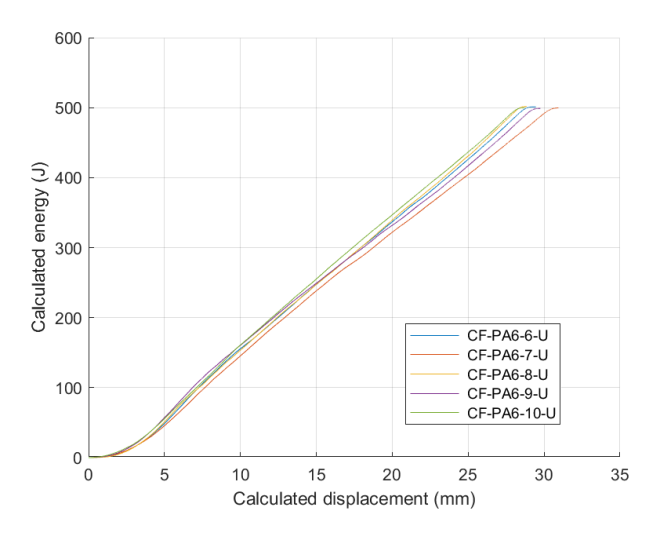


Figure 4.8: Cumulative energy transferred as function of displacement results for Corrugated coupons of CF-PA6.

4.1.2 CF-PA66

PA66 is relevant to the water content in the matrix; therefore, the drying process was performed before testing the coupons to ensure that the water

absorption of the materials did not influence the performance of the composite. The drying process and methodology are explained in detail in the previous section.

Splaying

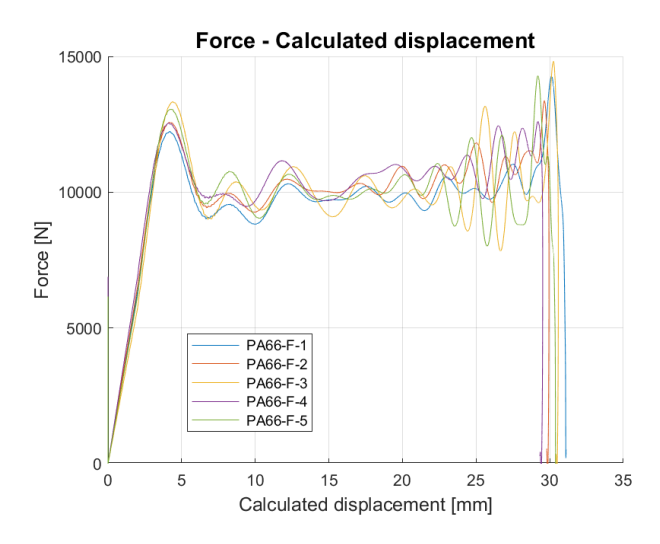


Figure 4.9: Force as function of displacement results for Splaying setup of CF-PA66.

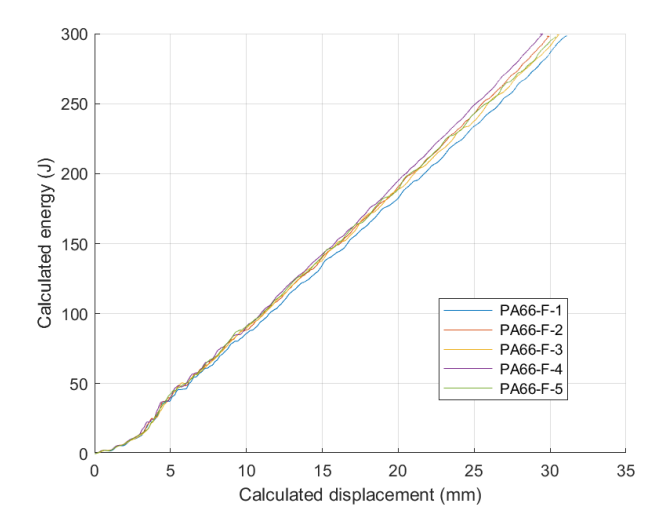


Figure 4.10: Cumulative energy transferred as function of displacement results for Splaying setup of CF-PA66.

The experimental testing for the splaying setup is shown in Figures 4.9 and 4.10. The first curve, force as a function of displacement, shows the typical behavior of crashworthiness testing, and the curve related to energy indicates that the coupons were tested in order. However, it is clear that the last part of the test has a clear sinusoidal excitation, suggesting that a mode shape may be exited at that part of the test, or that the material is

affected by the velocity of impact. This will be investigated further using a quasi-static analysis.

Tearing

The tearing setup exhibited different characteristics from the splaying setup in terms of the crashworthiness behavior of the coupon with higher forces owing to the enhanced failure of the fibers by the tearing setup and a growing force trend as the coupon absorbed the impact, as shown in Figure 4.11 Again, the sinusoidal excitation was present as the coupon stable region reached the end of the testing.

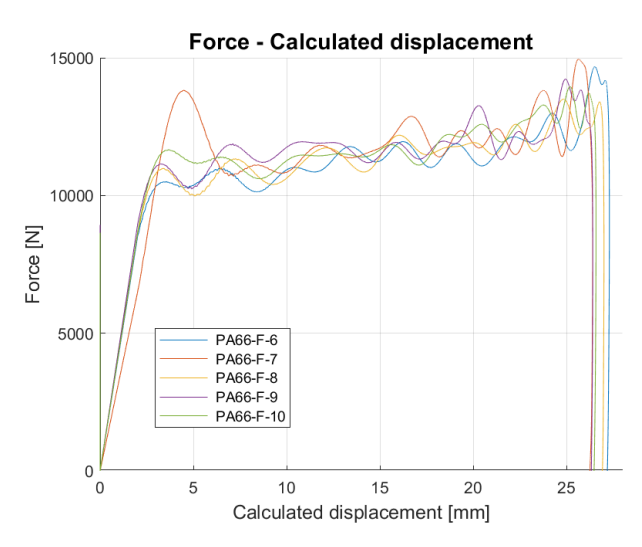


Figure 4.11: Force as function of displacement results for Tearing setup of CF-PA66.

Figure 4.12 illustrates the cumulative energy absorbed, which increased steadily, confirming consistent energy dissipation during deformation.

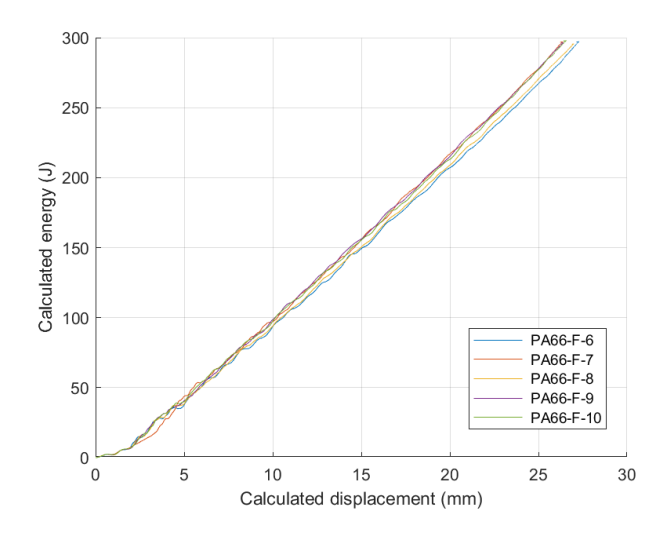


Figure 4.12: Cumulative energy transferred as function of displacement results for Tearing setup of CF-PA66.

Corrugated

Figures 4.13 and 4.14 illustrate the experimental testing of CF-PA66 coupons, and the curve related to the force as a function of displacement is characterized by oscillations along the curve, suggesting a sum of many factors, such as local failure modes, mode shapes, or stress redistribution. It is important to note that there is no specific sinusoidal behavior at the low-velocity part of the test and that the growing trend of the force increases as the velocity decreases.

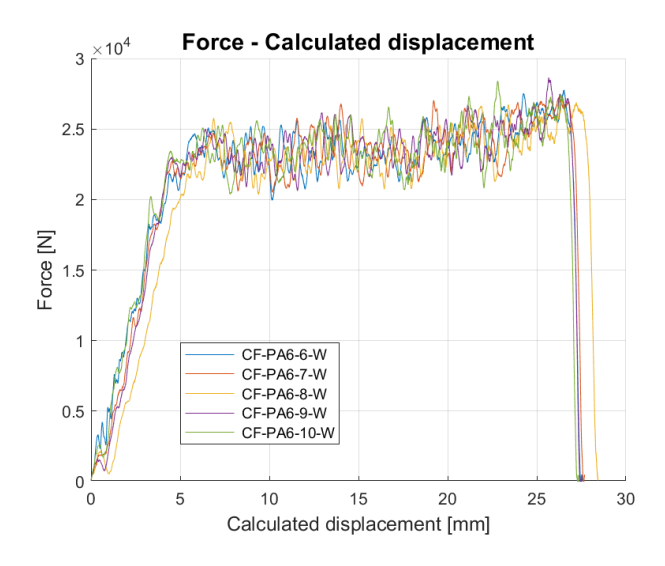


Figure 4.13: Force as function of displacement results for corrugated coupons of CF-PA66.

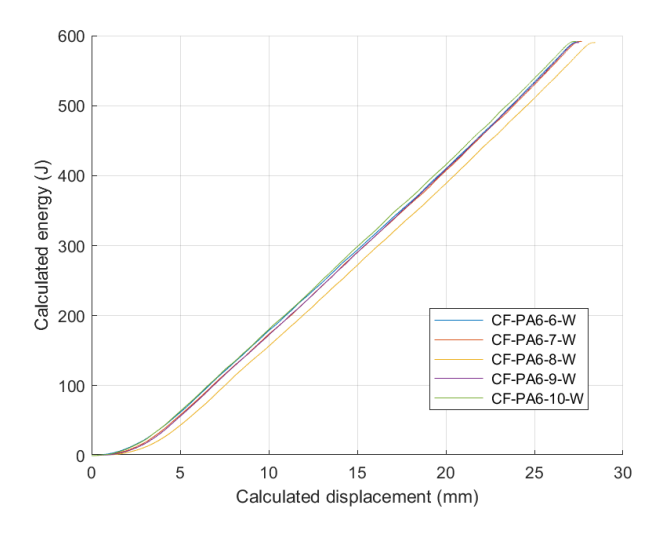


Figure 4.14: Cumulative energy transferred as function of displacement results for Corrugated coupons of CF-PA66.

4.1.3 CF-PC

Splaying

Figure 4.15 shows the force as a function of displacement for the CF-PC composite; the curve exhibits a fluctuating plateau in the crushing region at approximately 7–8 [kN] indicating progressive interlaminar delamination and fiber pull-out. This behavior occurred with the dominance of interfacial failure with limited fiber breakage, consistent with the splaying failure mode.

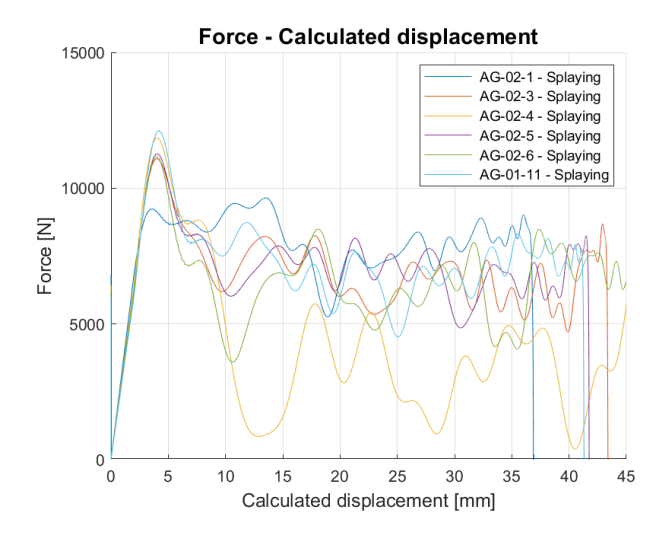


Figure 4.15: Force as function of displacement results for Splaying setup of CF-PC.

Figure 4.16 illustrates the cumulative energy absorption. The gradual and continuous increase without sudden jumps reflects a relatively controlled failure process.

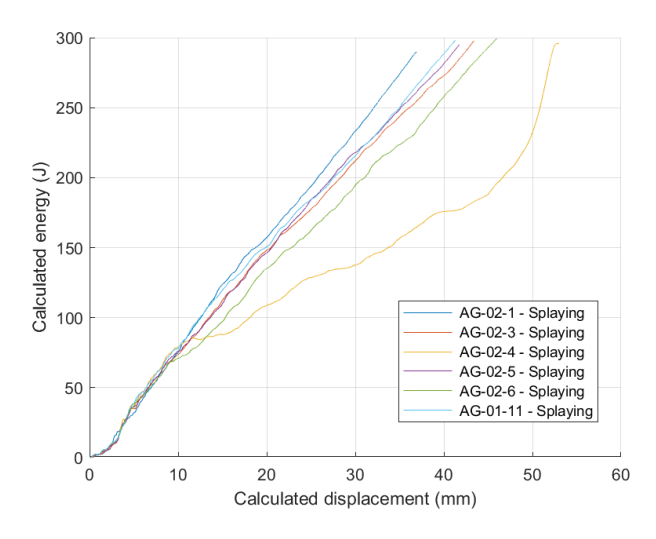
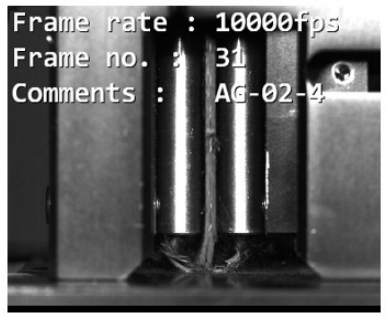


Figure 4.16: Cumulative energy transferred as function of displacement results for Splaying setup of CF-PC.

For both figures 4.15 and 4.16 the specimen AG-02-4 exhibit an underperformance behavior not following the gradient for the rest of the coupons tested, a deeper look at the crushing test shown at figure 4.17 can be seen that the specimen suffer critical delamination failure mode with a buckling failure mode, this was the reason for its critical under-performance because of the simultaneous double failure mode the drop of reaction forces is generated, reaction forces are raise after the buckled part of the coupon touch again the impact surface, to avoid any type of manufacturing defects another coupon was tested to replace this one and keep the statistical conformity.





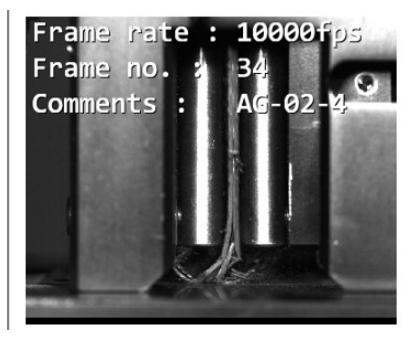


Figure 4.17: Experimental Test of coupon AG-02-4 experiencing delamination and buckling failure modes.

Tearing

The CF-PC Tearing configuration testing results are shown in figure 4.18. For the splaying condition, the plateau region was characterized by irregular oscillations, indicating unstable crack propagation and a higher degree of

fiber and matrix fracture. Compared to the splaying configuration, the mean force is higher because of fiber failure.

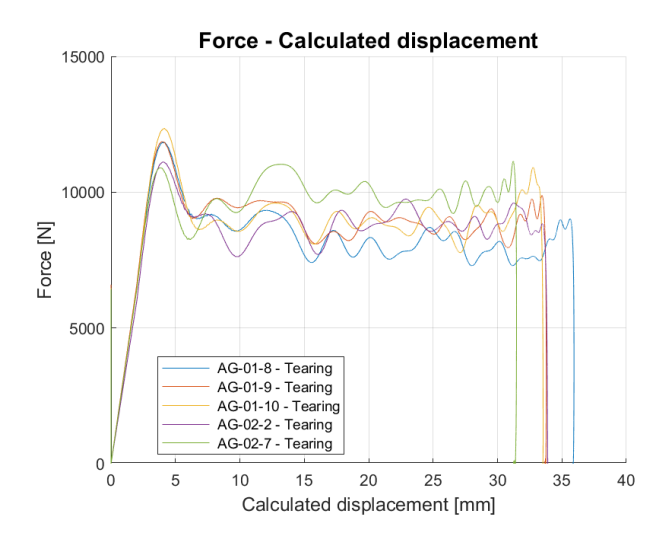


Figure 4.18: Force as function of displacement results for Tearing setup of CF-PC.

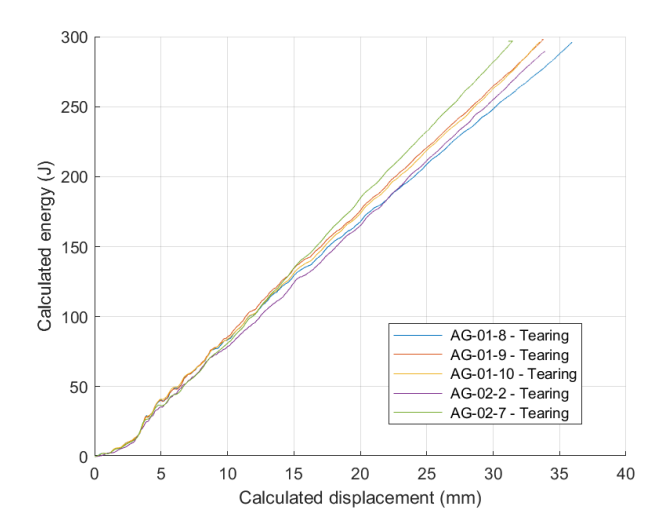


Figure 4.19: Cumulative energy transferred as function of displacement results for Tearing setup of CF-PC.

Figure 4.19 confirms this behavior with a steeper energy accumulation profile than that of the splaying setup, implying more aggressive material failure and enhanced energy absorption due to matrix cracking and fiber rupture.

Corrugated

The corrugated tests were carried out by IVW, as illustrated in figure 4.20 showing the force-displacement curve, which exhibits a sequence of load drops and recoveries, typical of local buckling and progressive collapse mech-

anisms. These oscillations suggest localized crushing events, where energy is dissipated through a combination of fiber fractures and matrix failures. Additionally, a trend can be observed in which the mean force at the steady plateau decreases as the velocity of the impact decreases.

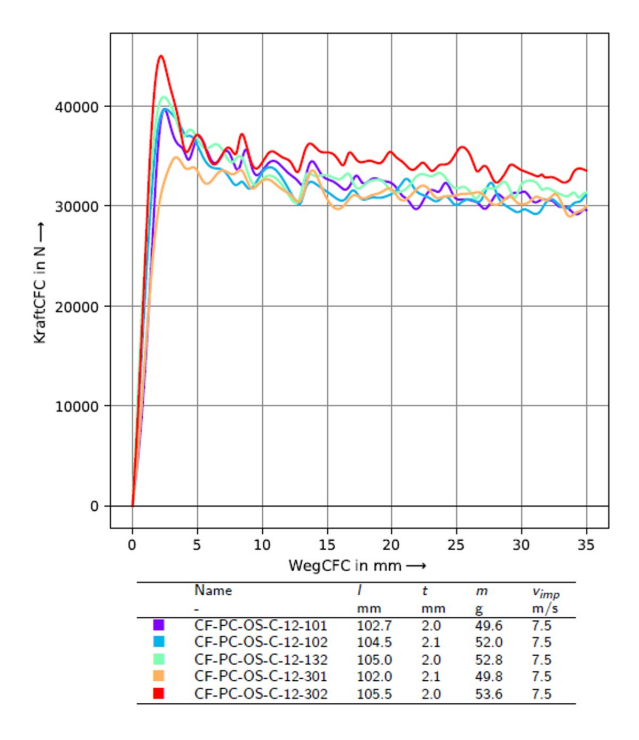


Figure 4.20: Force as function of displacement results for corrugated coupons of CF-PC.

4.1.4 GF-PP

Splaying

Figure 4.21 shows the force-displacement curve for the splaying conditions. The curves are characterized by an abrupt initial peak of force related to the trigger, followed by a large drop in the reaction forces, with an unsteady plateau at approximately 500 [N]. The coupons were unable to withstand the impact energy, as shown in Figure 4.22 only reaching a cumulative energy absorption of approximately 40 [J], indicating low overall energy absorption dominated by friction and interfacial failure. This behavior is consistent with a low-efficiency splaying mode; however, it is not relatable to other composite materials for this testing setup. Additionally, because the coupons could not withstand the impact, the testing figure received the additional energy supplied by the drop tower; therefore, both curves were cut at the maximum displacement of the fixture.

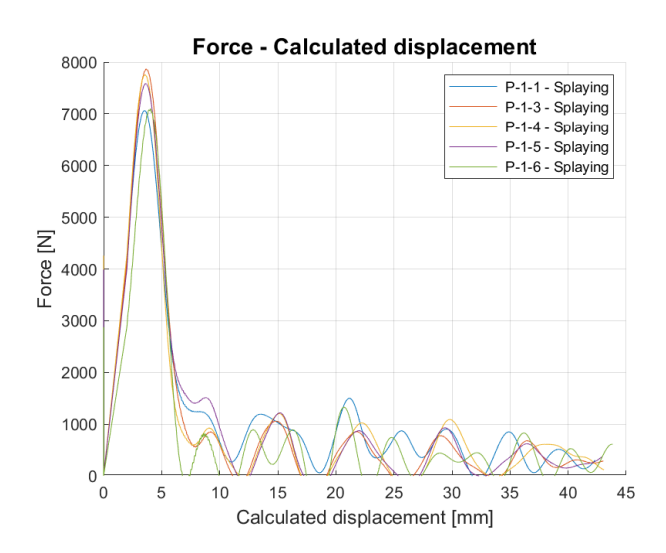


Figure 4.21: Force as function of displacement results for Splaying setup of GF-PP.

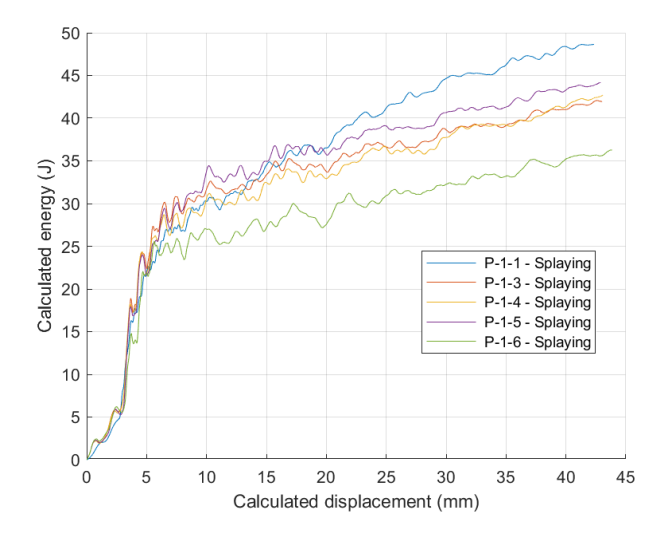


Figure 4.22: Cumulative energy transferred as function of displacement results for Splaying setup of GF-PP.





Figure 4.23: GF-PP Flat coupons after Crashworthiness Splaying test, delamination in multiple layers can be observed.

As illustrated in Figure 4.23, the tested specimens did not exhibit any failure modes associated with fiber failure or brittle matrix failure. The GF-PP demonstrated distinct behavior following the trigger event. During the trigger phase, multiple failure modes were observed in the composite materials. However, immediately after the conclusion of the trigger geometry, a sudden delamination occurred across several layers of the composite, which began propagating. This left friction and delamination forces as the sole mechanisms for energy absorption, as evidenced by the suboptimal performance of the tests.

Tearing

The tearing test exhibited markedly different behavior compared to the splaying condition, as illustrated in Figure 4.24. The Force-Displacement curve revealed several notable characteristics. Following the trigger, a significant drop in the reaction forces was observed, succeeded by an increasing trend in the mean force within the crushing zone, where a plateau was typically located. Pronounced oscillations were observed in this region. Compared with other materials, the performance in resisting crushing is lower.

Figure 4.25 shows a more linear and steeper energy absorption curve than that in the splaying case, indicating a moderately improved performance.

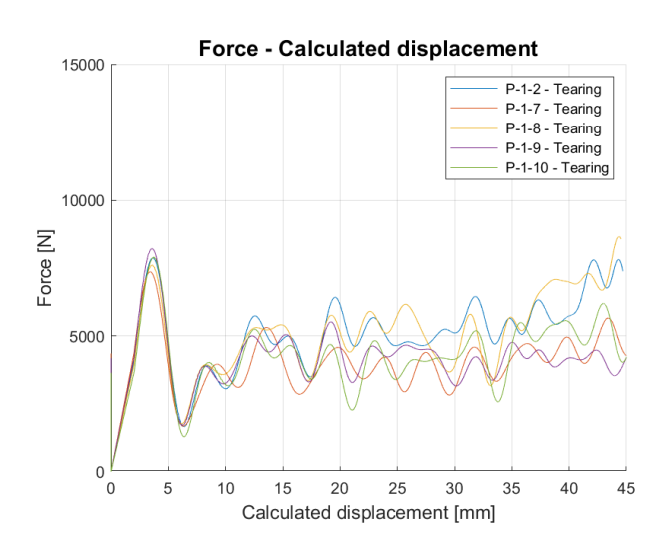


Figure 4.24: Force as function of displacement results for Tearing setup of GF-PP.

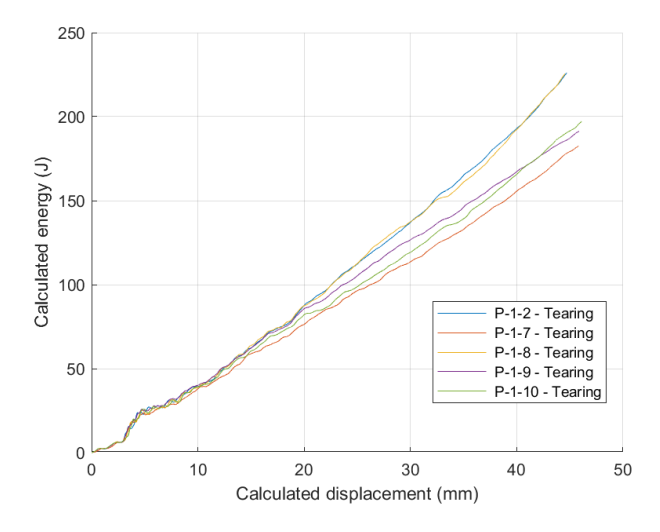


Figure 4.25: Cumulative energy transferred as function of displacement results for Tearing setup of GF-PP.

However, it can be seen again that the coupons were not able to withstand the total amount of energy in the test; therefore, the data were cut up to the maximum displacement of the fixture.





Figure 4.26: GF-PP Vigna coupons after Crashworthiness Tearing test, multiple failure modes are observed.

The coupons exhibited a mix of multiple failure modes, as shown in Fig. 4.26. It can be observed that the specimens suffered delamination along many of their layers; however, owing to the tearing setup, which forces the failure of the fibers by blocking the path for the material, it can also be observed how the matrix suffers brittle failure, as for the fibers.

Corrugated

Figure 4.28 shows the force–displacement curve for the coupons tested at Instron. The experimental testing was characterized by some phenomena from the previous testing setups. A significant drop in the reaction forces was observed, followed by an increasing trend in the mean force within the crushing zone, achieving higher forces than at the trigger phase, which is an atypical phenomenon.

The cumulative energy absorbed is presented in Fig. 4.28 exhibits particular behavior showing a non linear trend along its curve and having the highest slope at the end of the test.

The IVW test is illustrated in Fig. 4.29 the curve exhibits force-displacement of the experimental testing it shows the characteristic drop of force after the trigger phase and the incremental trend of the mean force, however the oscillations are not as relevant as for Instron coupons. The delta of the forces between the corrugated coupons can be explained by the difference in the

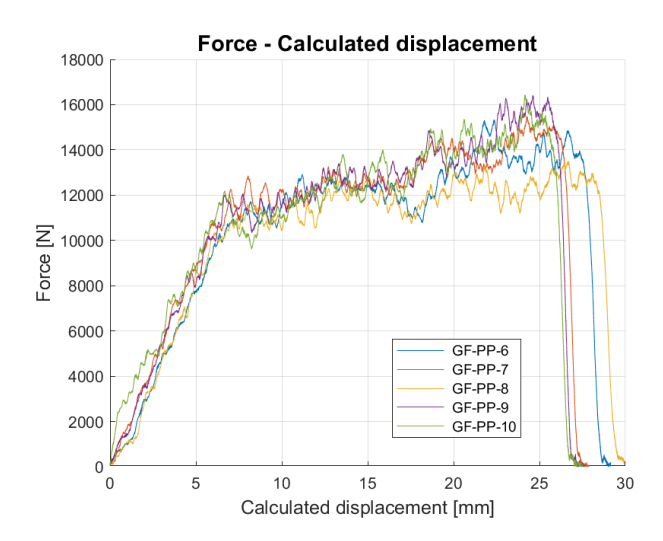


Figure 4.27: Force as function of displacement results for short corrugated coupons of GF-PP. (Instron tested)

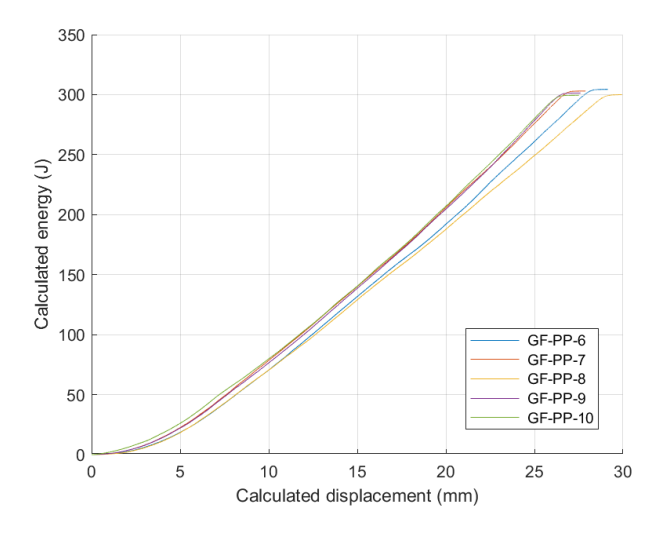


Figure 4.28: Cumulative energy transferred as function of displacement results for Corrugated coupons of GF-PP.

cross-section, with the IVW being the largest.

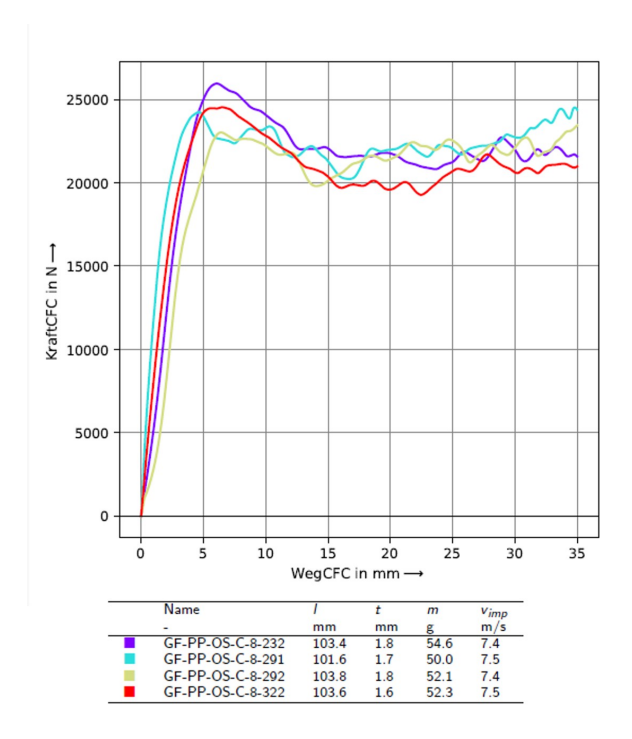


Figure 4.29: Force as function of displacement results for corrugated coupons of GF-PP. (IVW tested)

4.1.5 **GF-TEPEX**

Splaying

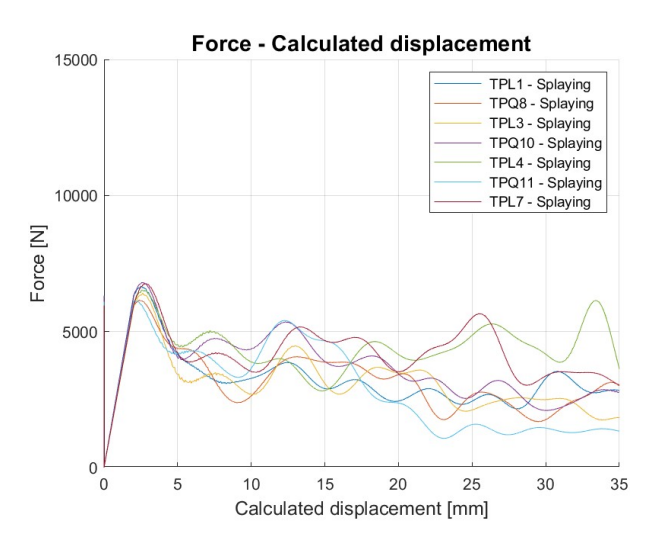


Figure 4.30: Force as function of displacement results for Splaying setup of GF-TEPEX.

Figure 4.30 presents the force as a function of the displacement for the GF-TEPEX composite. The curve is characterized by a steady plateau after the trigger effect at approximately 4 [kN] which corresponds to a displacement of approximately 20 [mm] there is a decreasing trend with a broader dispersion

of force.

Tearing

The force-displacement curve for the tearing setup is presented in Figure 4.31, which is characterized by an increase in the Force after the trigger effect, ranging from 4.5 [kN] to 7.5 [kN], with a more uniform dispersion of the force.

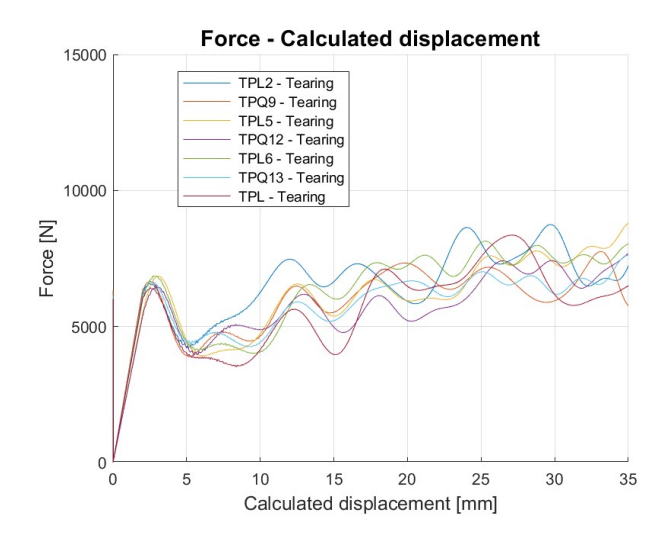


Figure 4.31: Force as function of displacement results for Tearing setup of GF-TEPEX.

Corrugated

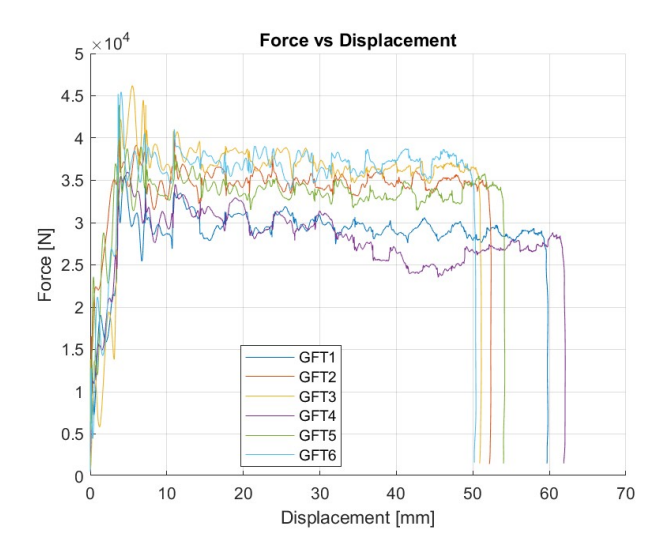


Figure 4.32: Force as function of displacement results for Corrugated setup of GF-TEPEX.

Figure 4.32 presents the force-displacement curve, which is characterized by a steady plateau after the trigger effect at approximately 3.5 [kN], except

for coupons GFT1 and GFT4, which exhibited an underperformance with a plateau at approximately 3[kN].

4.1.6 **CF-Epoxy**

Splaying

The Force-displacement curve for the splaying setup is presented in Figure 4.33 which is characterized by a decrease in performance after the trigger effect passing from approximately 11 [kN] to at the first part of the coupon to a range of 9[kN] at the last part of the coupons.

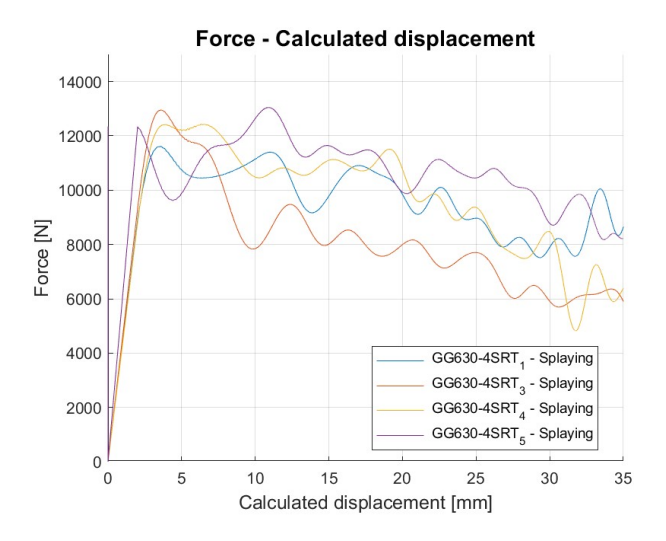


Figure 4.33: Force as function of displacement results for Splaying setup of CF-EPOXY.

Tearing

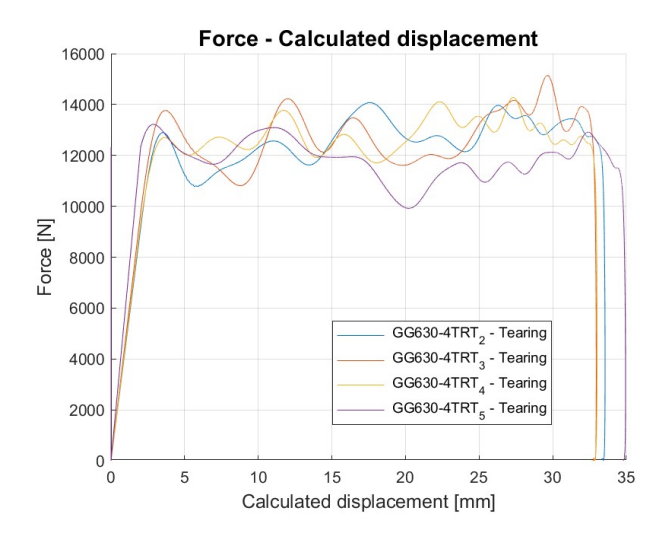


Figure 4.34: Force as function of displacement results for Tearing setup of CF-EPOXY.

For the tearing setup, a behavior close to what the failure theory predicts

is described by this composite characterized by a stable plateau around 12 [kN] after the trigger effect, as shown in Figure 4.34.

Corrugated

Figure 4.35 presents the force-displacement curve, which is characterized by a minimum influence of the trigger effect and a stable plateau at approximately 2.3 [kN] The dispersion of the force is relatively small, and coupon GG630F-B3RT-1 exhibited a not-in-order test, for which only will be considered in its stable region up to 14[mm].

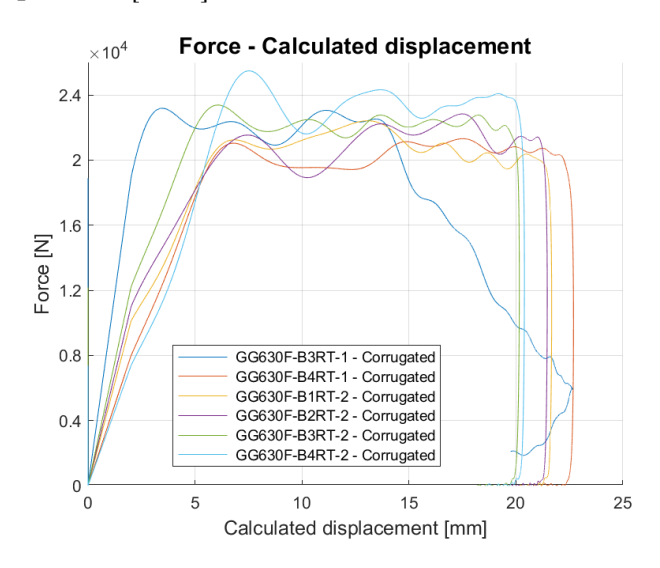


Figure 4.35: Force as function of displacement results for corrugated setup of CF-EPOXY

4.1.7 Variable velocity Crash testing

During the testing phase, certain materials exhibited behaviors suggesting that the nature of dynamic loading may significantly influence material performance. Consequently, further studies were conducted to ascertain whether the impact velocity was the factor triggering variations in performance. This new series of tests comprises both quasi-static and variable-speed testing, contingent upon the material in question.

Material	Quasi-Static test	Variable Velocity test
CF-PA66	Tested	X
CF-PC	Tested	X
GF-PP	Tested	Tested

Table 4.1: Test conducted for variable velocity.

For the quasi-static testing, an Instron 6800 Series Universal Testing System with a force range of 300 [kN] was employed. The system facilitated data acquisition rates of up to 5 [kHz] with an accuracy of $\pm 0.5\%$. The compression rate for testing was set at 0.0165 [s^{-1}] for CF-PA66 and CF-PC. Only splaying conditions were examined for these materials, whereas for GF-PP, both splaying and tearing conditions were assessed under quasi-static conditions due to the experimental testing requirements.



Figure 4.36: 300 [kN] Instron 6800 Series Universal Testing Machine setup.

CF-PA66

Dynamic experimental testing revealed atypical behavior, which was likely attributable to the activation of a mode shape during the crash test. To enhance our understanding of whether the material was affected by the dynamic nature of the test and due to the paucity of comprehensive studies on mode shapes in the material, a quasi-static splaying test was conducted. As shown in Figure 4.37, the quasi-static test was compared with a dynamic test under splaying conditions. Both tests exhibited a similar peak during the trigger phase and a comparable mean force in the plateau crushing zone.

However, a notable distinction was the absence of sinusoidal behavior in the quasi-static test. This observation suggests that dynamic phenomena influence the performance of this material; however, further investigation into the mode shape activation is necessary.

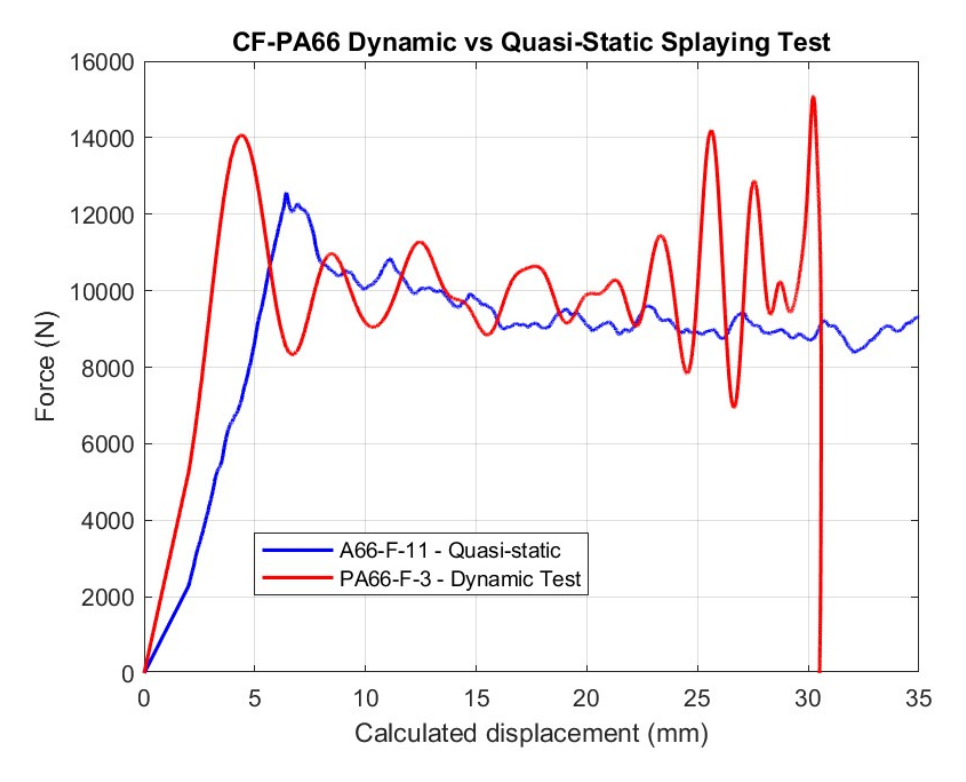


Figure 4.37: Quasi-static and Dynamic test comparison of a Splaying setup of a CF-PA66 coupons.

In Figure 4.38, a pure splaying mode is observed, with debris accumulating at the center of the specimen and acting as wedges for the delamination of the composite. The matrix did not suffer any brittle failure, and a minimum failure of the fibers was evident, indicating a typical splaying failure mode.

CF-PC

Carbon Fiber Polycarbonate demonstrated experimental results characterized by significant white noise and unstable behavior. The test coupons exhibit multiple failure modes, including brittle matrix failure, splaying failure, and transverse shearing. However, an analysis of the tests using high-speed cameras revealed interactions among these failure modes during crash testing. Consequently, quasi-static testing is pertinent to determine whether the interaction between failure modes is inherent to dynamic testing or attributable to the characteristics of the material.



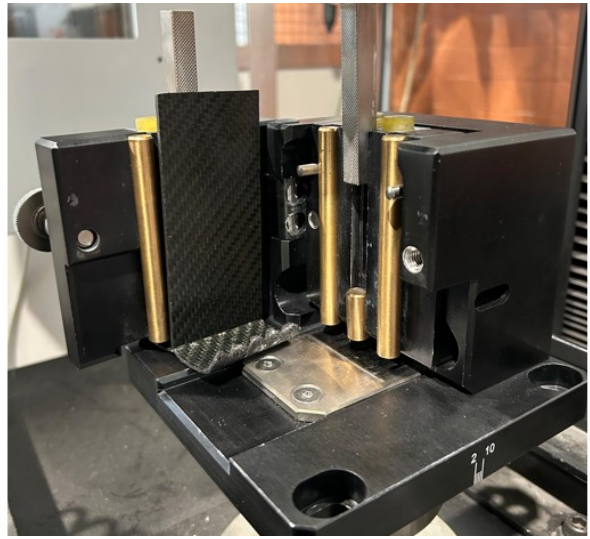


Figure 4.38: From left to right, (A) Bottom part of quasi-static CF-PA66 coupon. (B) CF-PA66 in the testing bench.

Figure 4.39 shows the force-displacement curves for both the dynamic and quasi-static splaying tests. Both tests exhibited a low peak of the trigger, which was almost nonexistent, and the crash test exhibited unstable behavior in the plateau of the crushing zone, given the multiple failure modes occurring in the dynamic load. However, the quasi-static test exhibited similar behavior in terms of the failure modes and reaction forces acting on the splaying-compression tests. Given the experimental data and Figure 4.40 where the same failure modes as those for a crash test are exhibited, it can be understood that the dynamic tests were representative and not related to the dynamic loads.

GF-PP

During all experimental tests, GF-PP exhibited anomalous behavior, prompting further investigation to better understand the underlying causes of the performance of the flat coupons. This study aimed to determine whether the observed behavior was related to the dynamic loads or geometry of the Vigna coupons, which may have led to a specific delamination failure mode. Consequently, a new series of tests was designed to assess the performance of the Vigna coupon geometry under various test conditions. The following test plan, as illustrated in Table 4.2, was developed and implemented.

As outlined in the test plan, the objective was to deliver an equivalent

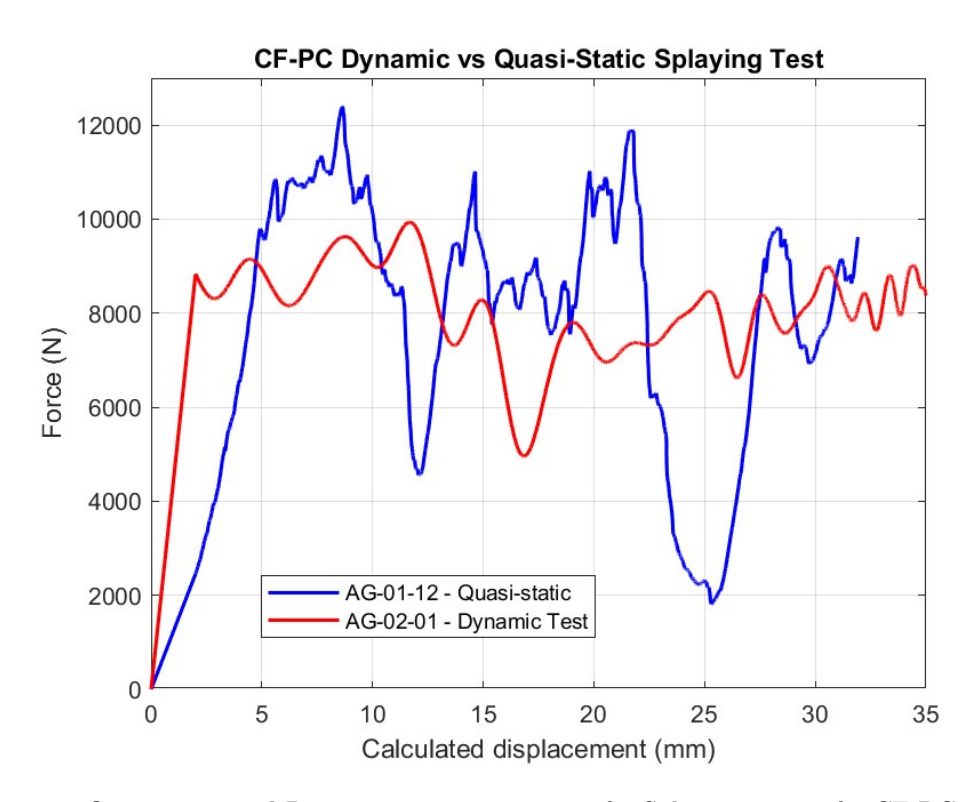


Figure 4.39: Quasi-static and Dynamic test comparison of a Splaying setup of a CF-PC coupons.



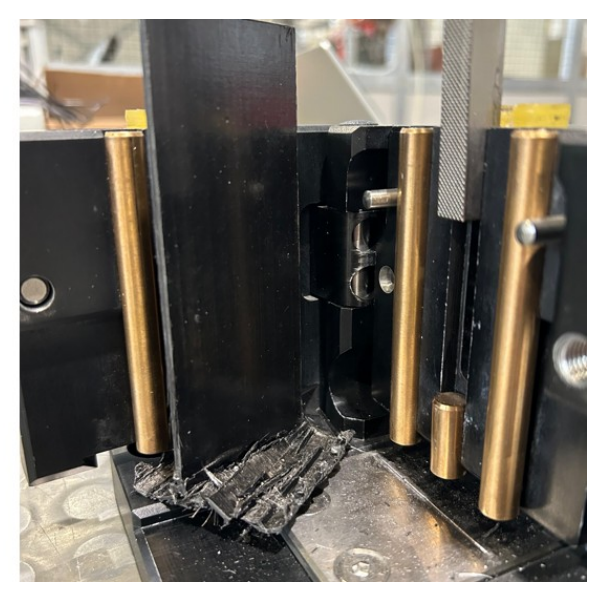


Figure 4.40: From left to right, (A) Bottom part of quasi-static CF-PC coupon. (B) CF-PC in the testing bench.

Test Condition	Splaying Test	Tearing Test
Quasi-Static	$0.0165 [s^{-1}]$	$0.0165 [s^{-1}]$
Low Velocity	$3.02 [m \cdot s^{-1}]$	$3.02 \ [m \cdot s^{-1}]$
	65.750 [kg]	65.750 [kg]
	300 [J]	300 [J]
Reference Velocity	$7.47 \ [m \cdot s^{-1}]$	$7.47 \ [m \cdot s^{-1}]$
	10.750 [kg]	10.750 [kg]
	300 [J]	300 [J]
High Velocity	$10.22 \ [m \cdot s^{-1}]$	$10.22 \ [m \cdot s^{-1}]$
	5.750 [kg]	5.750 [kg]
	300 [J]	300 [J]

Table 4.2: Test parameters for the variable velocity test plan.

amount of energy to the coupons by varying the velocity and mass of the crash test. Because this new test plan was not part of the initial study, a new batch of coupons was manufactured by IVW. To ensure that the behavior was representative, a reference test was performed to validate the data against previous results. Two coupons were tested under each setup for the quasi-static, low-velocity, and high-velocity tests.

The Quasi-Static Splaying setup experimental testing exhibited in figure 4.41 shows a force-displacement curve, which contains a dynamic vs quasi-static test, and clearly shows severe differences in the performance and behavior of both specimens. The quasi-static test (blue) exhibited a higher force peak at the trigger phase, and a clear stable plateau was observed during the crush zone, characterized by a decremental trend as the coupon was crushed. This comparison helps in understanding the impact of dynamic loading on the material, which clearly underperforms compared to a non-dynamic test.

Figure 4.42 shows the results of the quasi-static splaying test. The coupons showed typical delamination with debris forming a wedge in the center of the coupon; however, the interlaminate delamination phenomenon was not present, and there was no evidence of propagation of the delamination inside the coupon, demonstrating that the material behavior was affected by the dynamic loads. The proper influence will be studied in variable velocity tests.

Figure 4.43 shows the force-displacement curve, illustrating the behavior

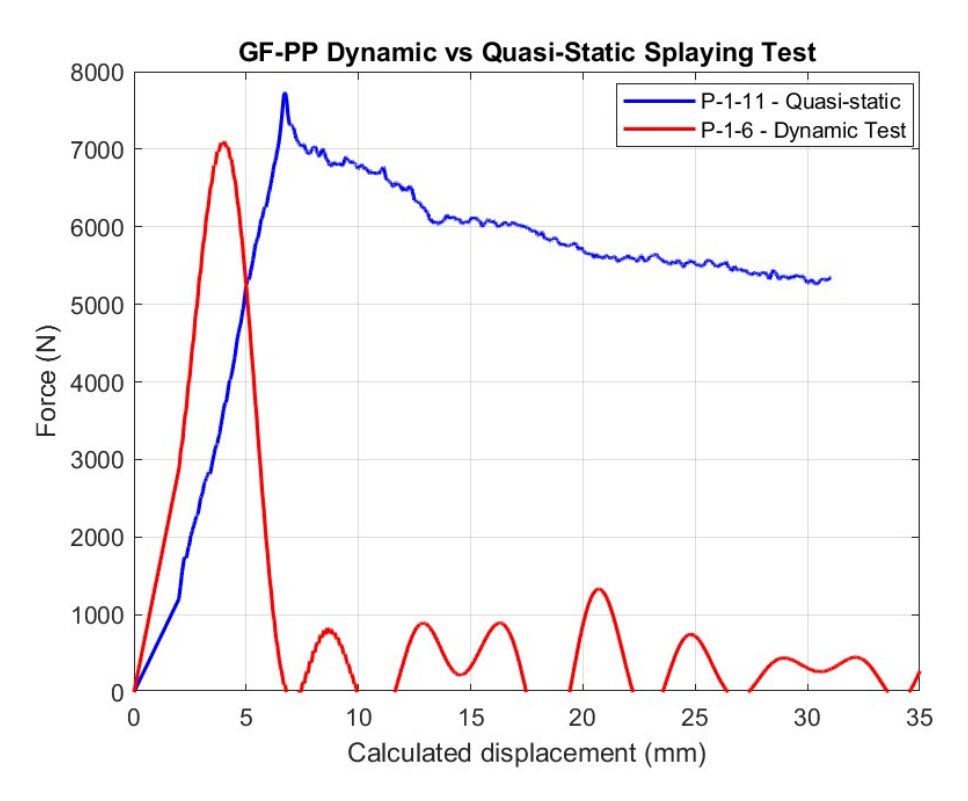


Figure 4.41: Quasi-static and Dynamic test comparison of a Splaying setup of a GF-PP coupons.

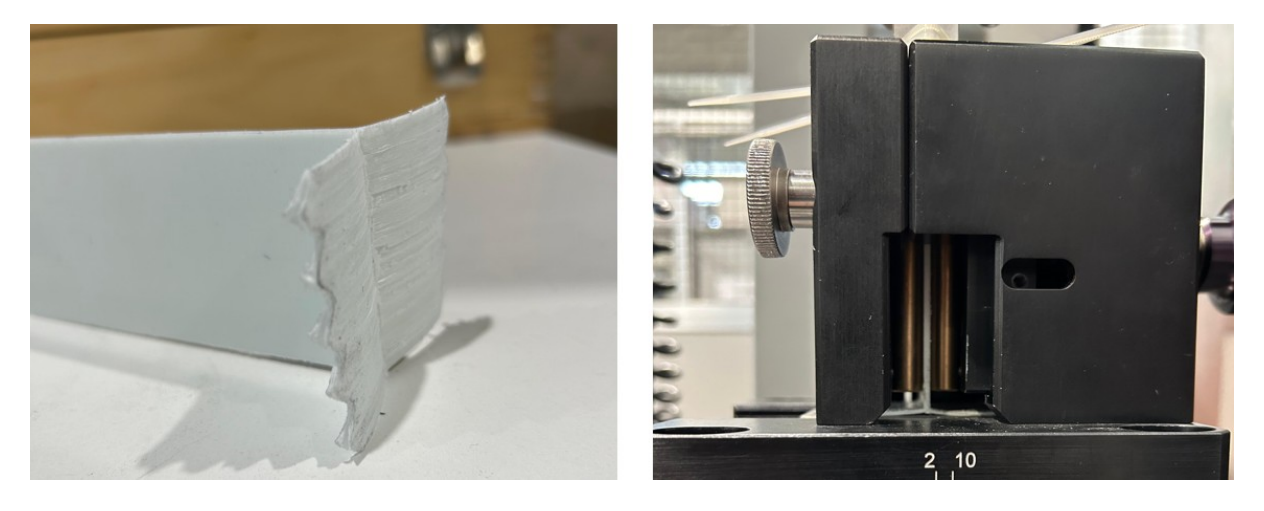


Figure 4.42: From left to right, (A) Bottom part of quasi-static GF-PP coupon. (B) GF-PP in the testing bench.

of both dynamic and quasi-static tests. The characteristics of the quasistatic coupon (blue line) were completely different from those of the dynamic coupon, with a null trigger peak and more than doubling the mean force during the plateau of the crushing zone. In addition, the sinusoidal behavior is reduced, and the material does not exhibit large sudden drops in reaction forces. This curve clearly exhibits a mismatch characteristic as a function of the type of load applied.

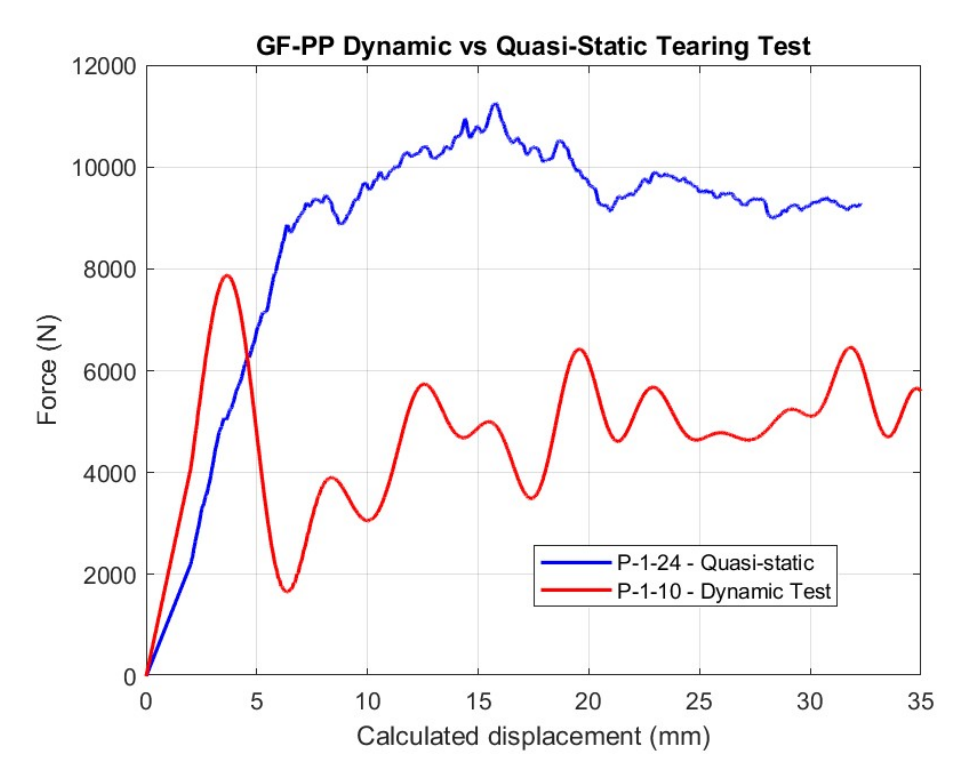


Figure 4.43: Quasi-static and Dynamic test comparison of a Tearing setup of a GF-PP coupons.

Following the quasi-static test analysis, a variable velocity test was conducted to gain a deeper understanding of the impact dynamics, with velocity as the primary variable. This study aimed to determine whether a correlation exists between performance deficiencies and impact velocity. The subsequent two images illustrate these tests.

Figure 4.44 presents the force-displacement curve obtained from the variable velocity test under the splaying setup conditions. Two main characteristics can be observed: the trigger peak of the coupon increases as the velocity increases in a noticeable manner, and the mean force at the crushing zone in a marginal approach is lower at higher velocities. Most probably, the inter-delamination of the coupon has a correlation with the velocity of

the impact; however, due to the lack of coupons, this study is not conclusive, and further development is required.

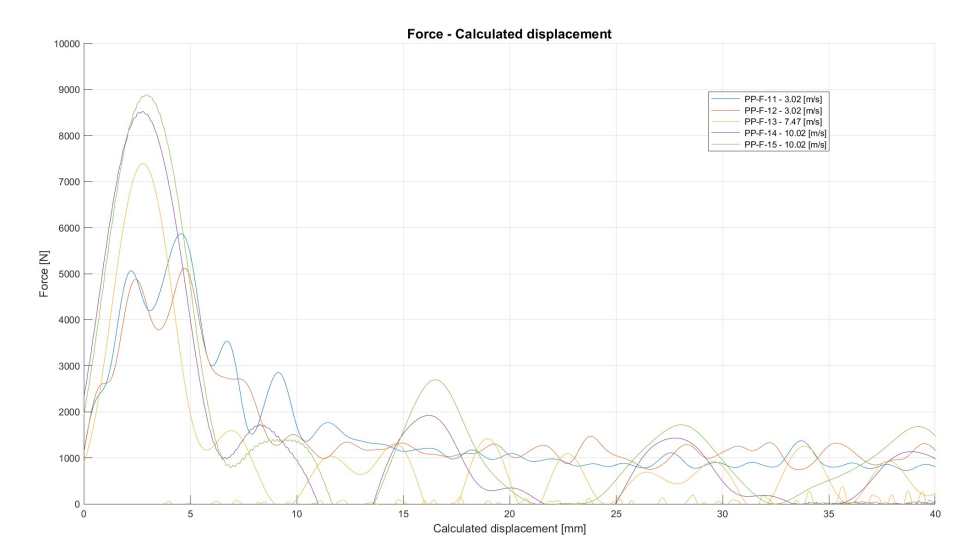


Figure 4.44: Force-displacement curve for splaying setup of variable velocity tests on GF-PP.

For the tearing setup, characteristics similar to those of the splaying conditions were found regarding the behavior of the trigger peak and the mean force under the crushing zone, with the remark that a stronger sinusoidal and force drop behavior was found to be more difficult to differentiate if there was a real difference in performance as a function of the impact velocity, as shown in Figure 4.45.

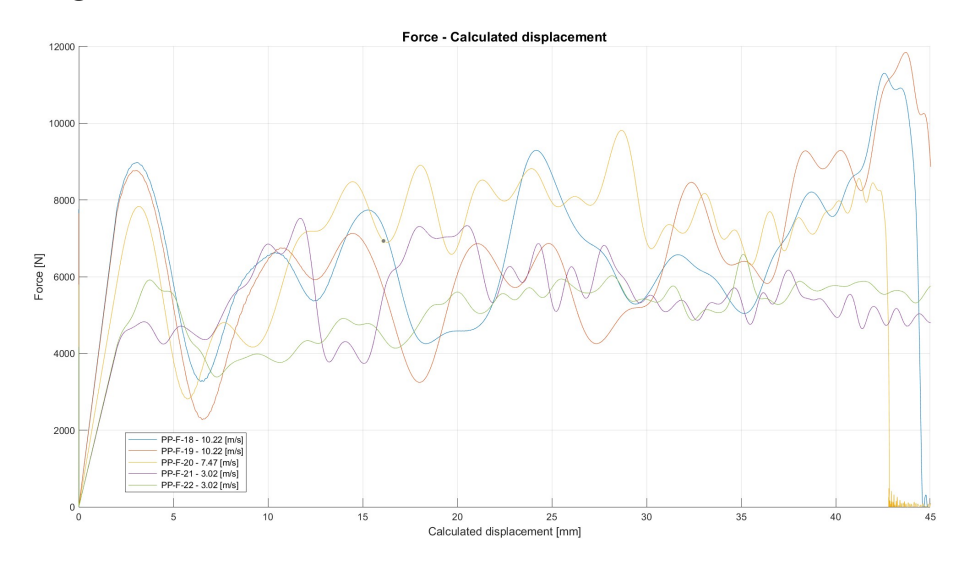


Figure 4.45: Force-displacement curve for tearing setup of variable velocity tests on GF-PP.

4.2 SEA Evaluation

Following the execution of the experimental testing and acquisition of data, the processing and evaluation of the Specific Energy Absorption (SEA) can be conducted. For this purpose, a specific MATLAB script was developed, considering the data input to establish a standardized method for selecting data from the crushing zone. Given that the tested coupons exhibited non-uniform displacement, the methodology for determining the crushing volume was defined with the starting point set at 5 mm after the peak of the trigger phase and the endpoint defined as 80 % of the total displacement. This method ensures that the selected plateau is as unbiased as possible, regardless of the material. The selection of a crushing plateau zone is the most traditional methodology used in the state-of-the-art literature and is the one chosen for this study.

The subsequent sections describe a novel approach to Specific Energy Absorption (SEA). As previously mentioned, the nature of dynamic loads may affect certain composite materials. Therefore, examining the SEA as a function of velocity presents an intriguing avenue for investigation.

4.2.1 SEA

Specific Energy Absorption (SEA) remains the cornerstone metric for crash-worthiness assessment, quantifying a material's capacity to dissipate kinetic energy per unit mass as defined in Equation 2.2 Building on experimental observations (Section 4.1), this section rigorously evaluates SEA across all materials and configurations (splaying, tearing, corrugated) using the data processing framework established in Section 3.4.

The traditional methodology involves selecting an unbiased crushing zone, under which the volume is examined in accordance with the SEA, as described at the beginning of this chapter. After processing the data for each coupon tested, they were plotted for each material using a box plot and a MATLAB script to better understand the data distribution and begin identifying any potential trends that the data may exhibit.

Figure 4.46 shows a set of box plots of the SEA results for CF-PC, CF-epoxy, and CF-PA6, with the type of test performed on the abscissa in the following order: Spaying, Tearing, and Corrugated. The first two materials

(CF-PC and CF-epoxy) displayed in this figure exhibited the lowest SEA values in the splaying setup condition, intermediate performance in the tearing setup, and the best results in the corrugated coupons. Owing to the failure mode mechanisms acting in each coupon, this trend is coherent with the theory behind the SEA mechanism of composite materials. For the last curve referring to CF-PA6, the data behavior exhibited a decay in the SEA for the corrugated coupons and a splaying data with a large standard deviation as a reference. It is important to note that during the experimental testing, this material had failure modes of fiber failure and matrix brittle fractures during splaying setup conditions, which ensured a good performance at SEA.

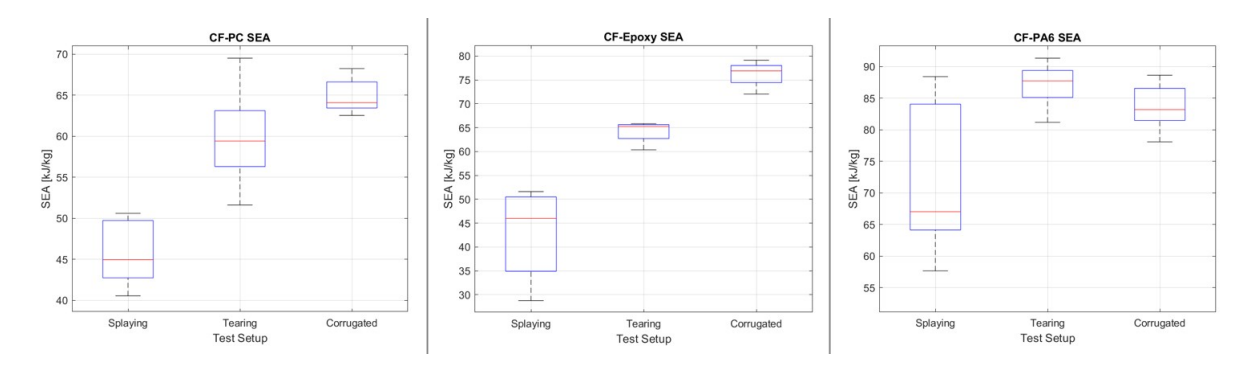


Figure 4.46: SEA obtain from experimental data of CF-PC, CF-Epoy and CF-PA6 (From left to right).

The remaining materials tested are shown in Figure 4.47. As for the previous curves, all of the materials in these box plots (GF-TEPEX, CF-PA66, and GF-PP) exhibited a behavior that was coherent with the theory of composites, with the splaying setup having the lowest performance, the tearing setup being intermediate, and the corrugated setup having the best performance for all three of them. Another characteristic relevant for a remark is the consistency of the corrugated coupons, which is the type of test with the lowest standard deviation with respect to the other setups for each material.

The results of the processed data for the mean SEA and their respective standard deviations are presented in Table 4.3. This behavior was consistent with the expected outcomes based on the failure mode theory for composite materials, except for CF-PA6. In addition to the previously mentioned comments, this material exhibited a decline in performance for short corrugated coupons. This issue will be further discussed in the validation statistical analysis section.

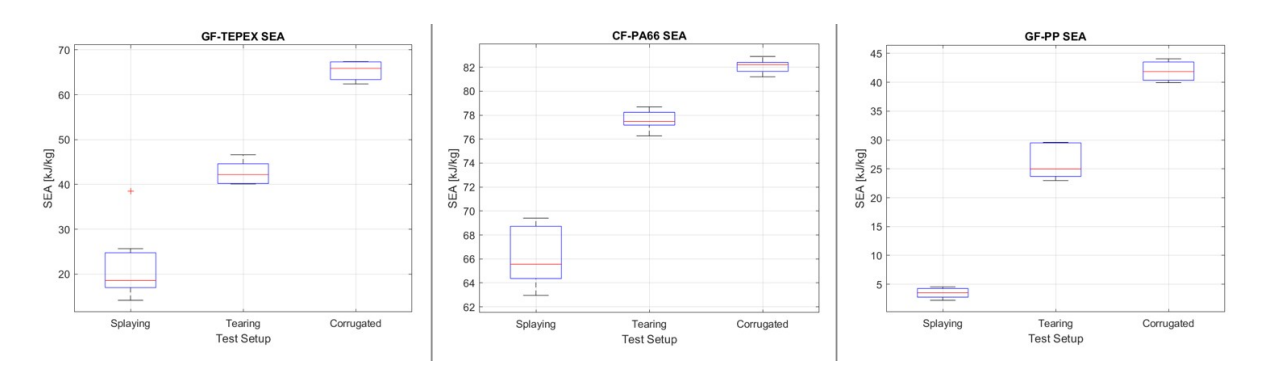


Figure 4.47: SEA obtain from experimental data of GF-TEPEX, CF-PA66 and GF-PP (From left to right).

Material	Splaying Setup	Tearing Setup	IVW Corrugated	Short Corrugated
CF-Epoxy	$43 \pm 9.6 [kJ \cdot kg^{-1}]$	$64 \pm 2.6 [kJ \cdot kg^{-1}]$	$76 \pm 3.0 [kJ \cdot kg^{-1}]$	-
CF-PA6	$72 \pm 12.7 [kJ \cdot kg^{-1}]$	$87 \pm 3.8 [kJ \cdot kg^{-1}]$	$84 \pm 3.4 [kJ \cdot kg^{-1}]$	$60 \pm 2.3 [kJ \cdot kg^{-1}]$
CF-PA66	$66 \pm 2.7 [kJ \cdot kg^{-1}]$	$78 \pm 0.9 [kJ \cdot kg^{-1}]$	-	$82 \pm 0.6 [kJ \cdot kg^{-1}]$
CF-PC	$46 \pm 4.2 \left[kJ \cdot kg^{-1} \right]$	$60 \pm 6.5 [kJ \cdot kg^{-1}]$	$65 \pm 2.2 [kJ \cdot kg^{-1}]$	-
GF-TEPEX	$22 \pm 7.8 \left[kJ \cdot kg^{-1} \right]$	$43 \pm 2.8 [kJ \cdot kg^{-1}]$	$65 \pm 2.2 [kJ \cdot kg^{-1}]$	-
GF-PP	$4 \pm 0.9 [kJ \cdot kg^{-1}]$	$26 \pm 3.1 [kJ \cdot kg^{-1}]$	$55 \pm 1.9 [kJ \cdot kg^{-1}]$	$43 \pm 2.4 [kJ \cdot kg^{-1}]$

Table 4.3: Mean SEA values with their respective standard deviation.

4.2.2 SEA as function of velocity

Experimental testing has demonstrated that reaction forces may be influenced by velocity, potentially affecting the Specific Energy Absorption (SEA). This is evident in various curves, such as the Force-Displacement and Crushing Velocity-Displacement curves, where the material behavior does not exhibit a stable plateau or linear pattern. This observation suggests that SEA, as a dynamic load parameter, may be influenced by the velocity. As illustrated in Figure 4.48, a change in behavior is observed in the left curve representing the crushing velocity-displacement, while the mean force remains on the crushing plateau with negligible changes in the right curve, force-displacement. It is logical to consider that the dynamic component of velocity can influence this parameter, and incorporating this consideration could provide a more legitimate approach compared with traditional methods. Consequently, two different approaches were considered to gain a comprehensive understanding of the impact of velocity on SEA.

• Discrete, this approach defines a threshold from the Crushing velocitydisplacement at the point were the linear behavior from the velocity changes to a non-linear behavior, it can be observed at the figure 4.48 which exhibit the main principle defining a threshold and computing the SEA for each of them.

• Continuous, this approach takes discrete idea but transforms it into an integral approach to the Energy-Displacement curve from the experimental testing taking every step from the data acquisition system to evaluate under the equation 2.2 and then obtain a curve SEA-Displacement, this process was perform developing a scrip in Matlab.

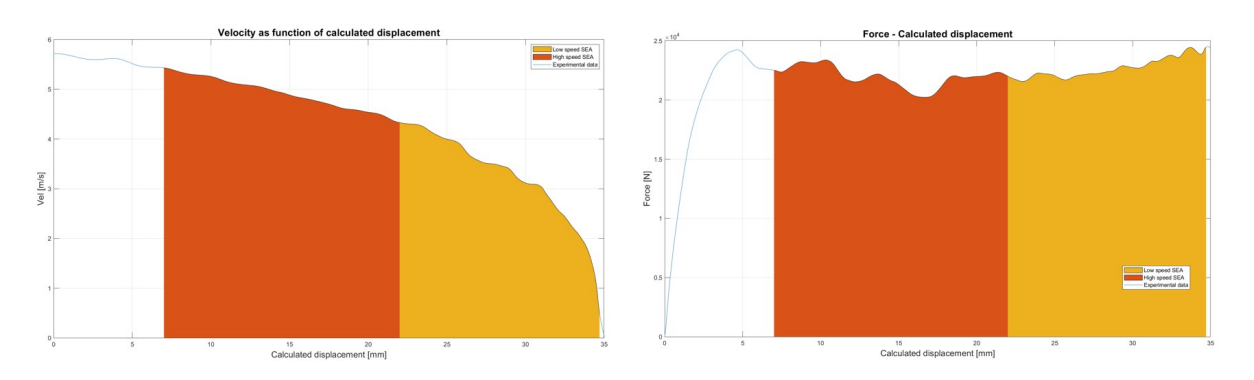


Figure 4.48: CF-PC Splaying test, (A) Velocity-displacement curve (B) Force-displacement curve.

SEA as function of velocity discrete approach

CF-Epoxy

Figure 4.49 illustrates the SEA evaluated in the two regimes of the high-speed (HS SEA) and low-speed (LS SEA) regions of each coupon tested under the different setups. It was observed that for splaying and tearing conditions, the effect of the crushing velocity on the material was negligible and inconsistent; for the splaying condition, the LS SEA had a negligible better performance; however, at the Tearing setup, this behavior was inverted.

Table 4.4 presents the statistics of the $SEA_{(\dot{x})}$ for all the setup conditions. For the splaying setup, the standard deviation (STD) was too high to assess the real difference between the two regions, for the tearing setup, the influence of the crushing velocity on the SEA was negligible, and both values fell within the range of traditional SEA values, as shown in Table 4.3, indicating that the crushing velocity influence is negligible to the crushing energy capacity of this material.

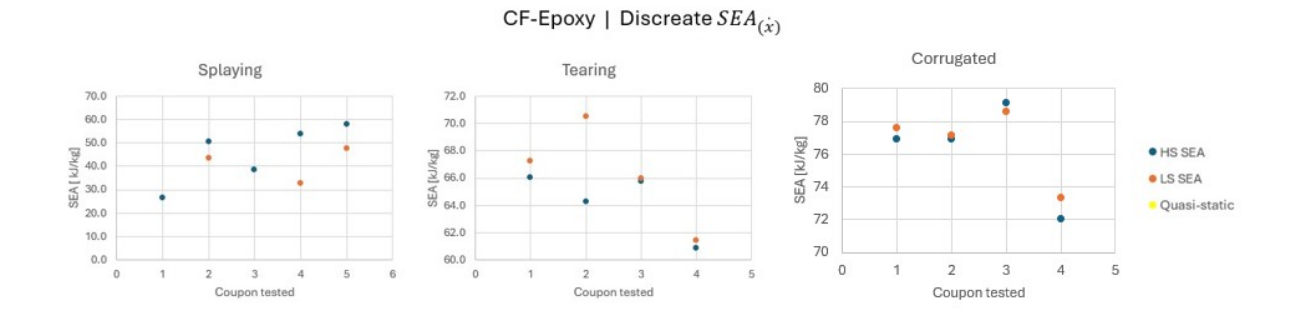


Figure 4.49: From left to right, Splaying, Tearing and corrugated results of SEA evaluation under high and low speed evaluation for CF-Epoxy coupons.

CF-Epoxy			
SEA Region	Splaying	Tearing	Corrugated
Mean HS	$45 \ [kJ \cdot kg^{-1}]$	$64 \ [kJ \cdot kg^{-1}]$	$76 \ [kJ \cdot kg^{-1}]$
STD HS	$12.7 \ [kJ \cdot kg^{-1}]$	$2.4 \ [kJ \cdot kg^{-1}]$	$3.0 [kJ \cdot kg^{-1}]$
Mean LS	$41 \ [kJ \cdot kg^{-1}]$	$66 \ [kJ \cdot kg^{-1}]$	$77 [kJ \cdot kg^{-1}]$
STD LS	$7.7 \ [kJ \cdot kg^{-1}]$	$3.8 [kJ \cdot kg^{-1}]$	$2.31 \ [kJ \cdot kg^{-1}]$

Table 4.4: $SEA_{(\dot{x})}$ results for CF-Epoxy.

CF-PA6

Figure 4.50 presents the results for each coupon evaluation of SEA under HS and LS regions to evaluate the effect of crushing speed on the SEA and whether it influences the SEA of the material. The figure shows the three setups from left to right: splaying, tearing, and corrugated. The material did not exhibit a trend for the data under the LS or HS results, with mixed data points across the different setups.

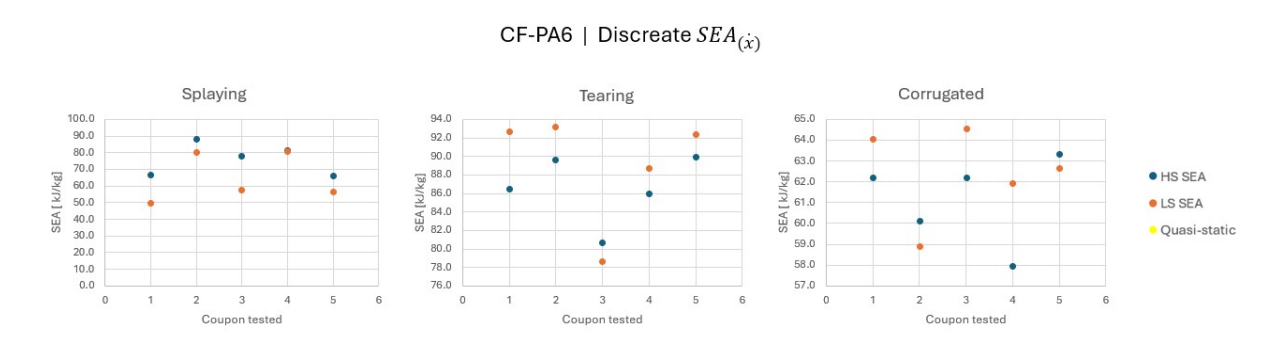


Figure 4.50: From left to right, Splaying, Tearing and corrugated results of SEA evaluation under high and low speed evaluation for CF-PA6 coupons.

Table 4.5 presents the statistics for the HS and LS regions for the different

setups for CF-PA6. For the splaying setup, it is noticeable how the $SEA_{(\dot{x})}$ decays in performance for the LS region, considering that the traditional approach exhibits a value that is in the middle of both the HS and LS regions, suggesting an influence of this testing setup. For the Tearing and Corrugated setups, the results present a negligible influence of the crushing speed on the SEA.

CF-PA6			
SEA Region	Splaying	Tearing	Corrugated
Mean HS	$76 \ [kJ \cdot kg^{-1}]$	$87 [kJ \cdot kg^{-1}]$	$61 \ [kJ \cdot kg^{-1}]$
STD HS	$9.5 [kJ \cdot kg^{-1}]$	$3.7 [kJ \cdot kg^{-1}]$	$2.1 \ [kJ \cdot kg^{-1}]$
Mean LS	$65 [kJ \cdot kg^{-1}]$	$89 [kJ \cdot kg^{-1}]$	$62 \ [kJ \cdot kg^{-1}]$
STD LS	14.6 $[kJ \cdot kg^{-1}]$	$6.1 \ [kJ \cdot kg^{-1}]$	$2.2~[kJ\cdot kg^{-1}]$

Table 4.5: $SEA_{(\dot{x})}$ results for CF-PA6.

CF-PA66

The material CF-66 exhibits a trend of improve performance at the LS region evaluation of the SEA, for the three different setups shown at the figure 4.51 at the splaying setup since the predominant failure mode is the delamination and matrix brittle failure the effects are less evident however for both tearing and corrugated setup due to the more complex failure mode, combining the fibers failure and the geometry this performance becomes more evident, it is important to remark that the experimental results 4.9, 4.11, 4.13 exhibit an incremental trend at the last part of the test and a sinusoidal excitation which can bring an explanation to this improvement in performance.

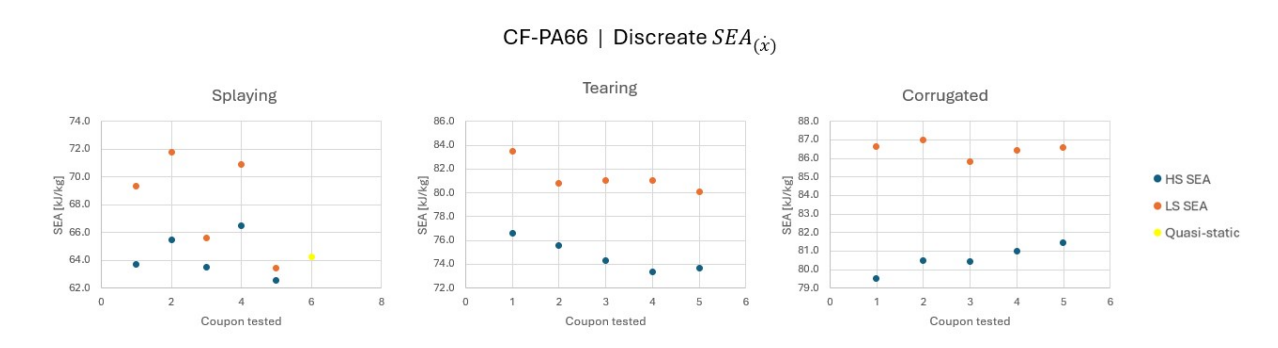


Figure 4.51: From left to right, Splaying, Tearing and corrugated results of SEA evaluation under high and low speed evaluation for CF-PA66 coupons.

Table 4.6 presents the statistics for the splaying, tearing, and corrugated setups for $SEA_{(\dot{x})}$. In this table, there is a clear difference in the SEA function of the crushing velocity, showing that this material increases its performance as the crushing velocity decreases. In addition, because the failure mode is more related to the fibers, this enhancement increases.

CF-PA66			
SEA Region	Splaying	Tearing	Corrugated
Mean HS	$64 \ [kJ \cdot kg^{-1}]$	$75 \ [kJ \cdot kg^{-1}]$	$81 \ [kJ \cdot kg^{-1}]$
STD HS	$1.6 \ [kJ \cdot kg^{-1}]$	$1.3 \ [kJ \cdot kg^{-1}]$	$0.7 [kJ \cdot kg^{-1}]$
Mean LS	$68 \ [kJ \cdot kg^{-1}]$	$81 \ [kJ \cdot kg^{-1}]$	$87 [kJ \cdot kg^{-1}]$
STD LS	$3.6 \ [kJ \cdot kg^{-1}]$	$1.3 [kJ \cdot kg^{-1}]$	$0.4 [kJ \cdot kg^{-1}]$

Table 4.6: $SEA_{(\dot{x})}$ results for CF-PA66.

CF-PC

Figure 4.52 shows the results of each coupon for the $SEA_{(\dot{x})}$ for the HS and LS regions for all setups. In the different scenarios, there was no noticeable trend, with mixed results for the Splaying and in Tearing conditions. The $SEA_{(\dot{x})}$ is mixed, whereas for the corrugated setup, there is a slight under performance of the LS SEA.

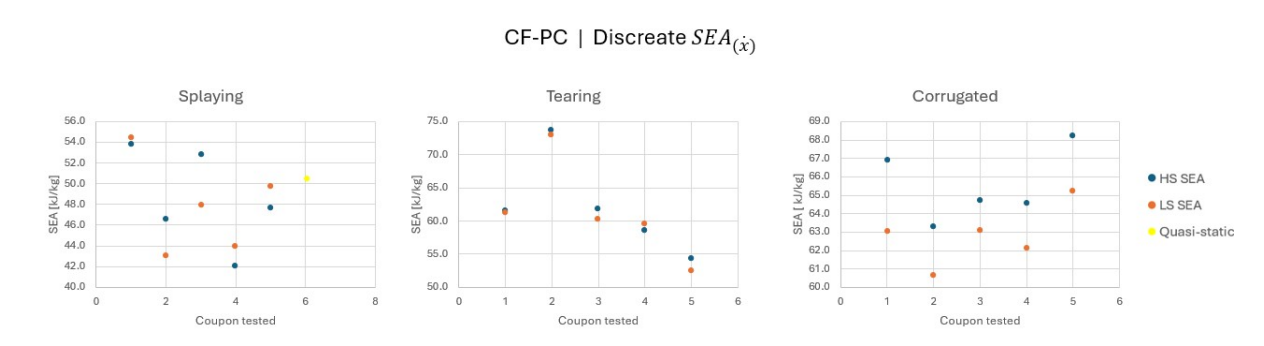


Figure 4.52: From left to right, Splaying, Tearing and corrugated results of SEA evaluation under high and low speed evaluation for CF-PC coupons.

Table 4.6 presents the statistics for the splaying, tearing, and corrugated setups for CF- PC $SEA_{(\dot{x})}$. As expected, there was no difference in the SEA for Splaying and tearing setups; however, there was a slight difference for the corrugated setup, which may indicate that the geometry may induce a change in performance as the crushing speed is reduced.

CF-PC			
SEA Region	Splaying	Tearing	Corrugated
Mean HS	$49 \ [kJ \cdot kg^{-1}]$	$62 \ [kJ \cdot kg^{-1}]$	$66 \ [kJ \cdot kg^{-1}]$
STD HS	$4.8 [kJ \cdot kg^{-1}]$	$7.3 [kJ \cdot kg^{-1}]$	$2.0 [kJ \cdot kg^{-1}]$
Mean LS	$48 \ [kJ \cdot kg^{-1}]$	$61 \ [kJ \cdot kg^{-1}]$	$63 \ [kJ \cdot kg^{-1}]$
STD LS	$4.6 \ [kJ \cdot kg^{-1}]$	$7.4 [kJ \cdot kg^{-1}]$	$1.7 [kJ \cdot kg^{-1}]$

Table 4.7: $SEA_{\ell}\dot{x}$) discrete approach for CF-PC

GF-PP

During experimental testing, this material exhibited a particular behavior related to the velocity and was not capable of withstanding the total impact energy. In Figure 4.53, for both splaying and tearing, the first two curves, which exhibit the crushing velocity-displacement curves, there is no transition for the crushing velocity sustaining during the whole test a linear behavior in a high speed regime for this reason there was no computation perform, however for the corrugated coupons observed in the right curve at figure 4.52 present a negligible difference in between the HS and LS regions.

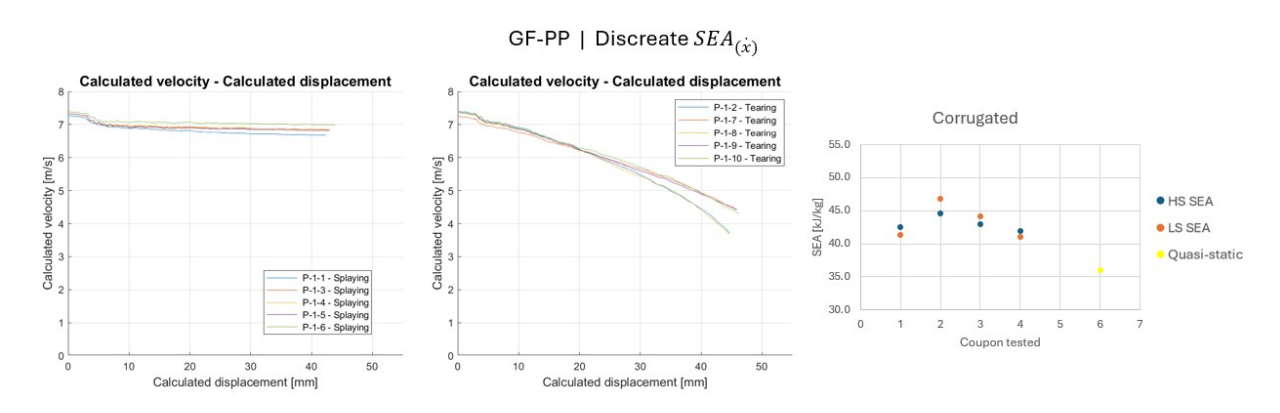


Figure 4.53: From left to right, Splaying and Tearing crushing velocity-displacement curve and corrugated results of SEA evaluation under high and low speed evaluation for GF-PP coupons.

This marginal difference is demonstrated in Table 4.8 which exhibits the statistics for $SEA_{(\dot{x})}$, with the corrugated geometry being the only relevant study. It shows a negligible change and mainly on the dispersion of the $SEA_{(\dot{x})}$ as the crushing speed decreases.

GF-PP				
SEA Region	Splaying	Tearing	Corrugated	
Mean HS	NA	NA	$43 \ [kJ \cdot kg^{-1}]$	
STD HS	NA	NA	$1.2 \ [kJ \cdot kg^{-1}]$	
Mean LS	NA	NA	$43 \ [kJ \cdot kg^{-1}]$	
STD LS	NA	NA	$2.7 \ [kJ \cdot kg^{-1}]$	

Table 4.8: $SEA_{\ell}\dot{x}$) discrete approach for GF-PP.

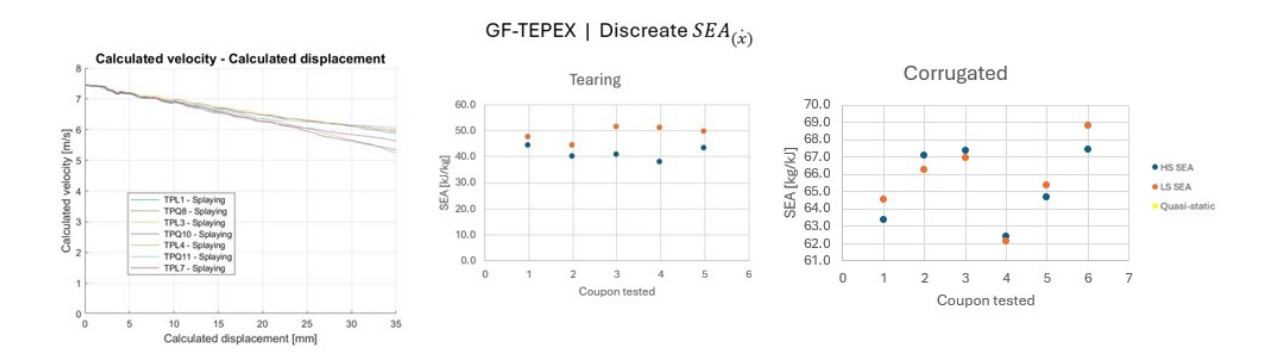


Figure 4.54: From left to right, Splaying crushing velocity-displacement curve, Tearing and corrugated results of SEA evaluation under high and low speed evaluation for GF-TEPEX coupons.

GF-TEPEX

This material exhibited a behavior similar to that of GF-PP in the splaying setup, with only a linear behavior crushing velocity throughout the test. For the tearing setup, the coupons evaluated in the HS and LS regions showed a marginal difference in performance improvement at the LS region.

Table 4.9 shows the statistics for the $SEA_{(\dot{x})}$; at the tearing evaluation, a difference is noticeable for the two different regions, indicating that there might be an influence on the SEA related to the crushing velocity.

GF-TEPEX			
SEA Region	Splaying	Tearing	Corrugated
Mean HS	NA	$41 \ [kJ \cdot kg^{-1}]$	$65 \ [kJ \cdot kg^{-1}]$
STD HS	NA	$2.4 [kJ \cdot kg^{-1}]$	$2.2~[kJ\cdot kg^{-1}]$
Mean LS	NA	$47 [kJ \cdot kg^{-1}]$	$66 \ [kJ \cdot kg^{-1}]$
STD LS	NA	$4.1 [kJ \cdot kg^{-1}]$	$2.3 \ [kJ \cdot kg^{-1}]$

Table 4.9: $SEA_i(\dot{x})$ discrete approach for GF-TEPEX.

SEA as function of velocity continuous approach

In the study of (\dot{x}) using a continuous approach, the SEA-crushing velocity curve was employed. Unlike traditional SEA curves, such as force-displacement curves, where the data begin at the origin, the SEA-crushing velocity curve begins with initial data at the impact velocity. As the material undergoes crushing, data are recorded, resulting in the reading of the crushing test proceeding from right to left.

CF-Epoxy

The analysis of the SEA as a function of velocity with a continuous approach is appreciated in the SEA-Velocity curve presented in Figure 4.55, where the splaying results are characterized by a broad range of SEA values and a stable plateau of SEA, whereas the tearing setup also presents the plateau but exhibits a narrower distribution of the SEA.

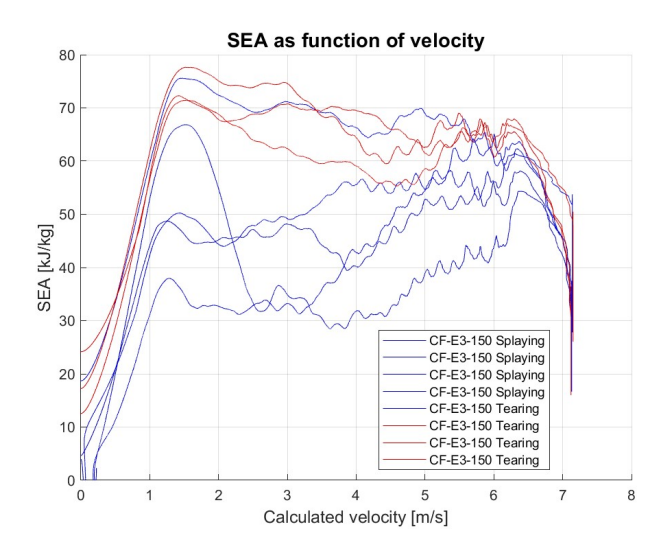


Figure 4.55: SEA(x)-Crushing velocity curve for splaying and tearing setup CF-Epoxy.

Figure 4.56 shows a steady behavior in the crushing plateau in the SEA-velocity curve, indicating that this material is not affected by the crushing velocity.

CF-PA6

Figure 4.57 presents the $SEA_{(\dot{x})}$ in a continuous approach. It is important to note that during the experimental testing, the PA6-F-7 and PA6-F-8 specimens exhibited an n.i.O. test, and the last part of the test was not

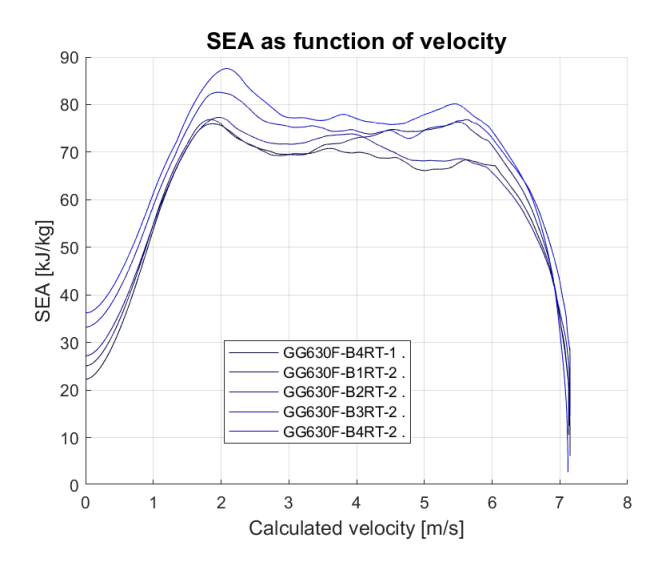


Figure 4.56: $SEA(\dot{x})$ -Crushing velocity curve for corrugated setup CF-Epoxy.

considered. In this curve, the effect of this failure is noticeable owing to an abrupt drop in the middle of crushing velocity.

In the curve, the specimens related to the splaying setup are shown in blue. The SEA does not follow a particular trend, having a broad dispersion, and at the end of the test, a small peak is reached at approximately $2 \ m \cdot s^{-1}$ followed by a decay in the SEA until the rushing velocity reaches 0. For the tearing condition, defined by the red curves, a consistent behavior was observed for all specimens; however, for the splaying conditions at a lower speed, a peak in the SEA was observed, followed by a decay as the crushing speed approached 0.

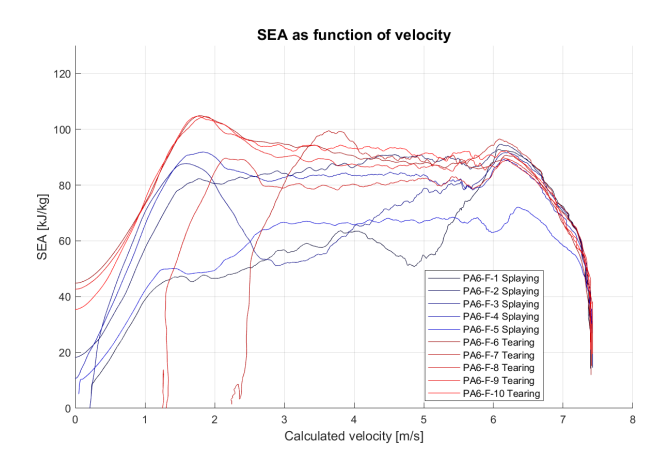


Figure 4.57: $SEA_{\ell}\dot{x}$)-Crushing velocity curve for splaying and tearing setup CF-PA6.

Figure 4.58 shows the SEA-crushing velocity curve for the corrugated specimens. A close distribution with a plateau after the trigger effect can be ob-

served. However, for the rest of the setups at the lower crushing speed, the coupons presented a peak at approximately $2 m \cdot s^{-1}$ followed by a decay in the SEA. This behavior was not noticeable in the $SEA_{\ell}(\dot{x})$ discrete approach.

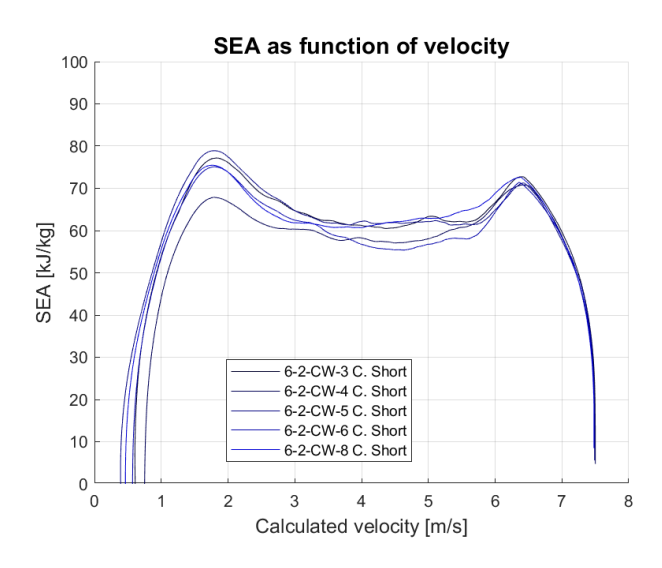


Figure 4.58: $SEA(\dot{x})$ -Crushing velocity curve for short corrugated setup CF-PA6.

CF-PA66

Figure 4.59 presents the SEA-crushing velocity curve for the splaying and tearing setups. The results for the splaying setup are shown in blue, and a uniform distribution was observed. After the trigger effect was surpassed, a clear trend was observed, showing an increase in the SEA as the crushing velocity was reduced to approximately $2 m \cdot s^{-1}$ followed by a decay in the SEA. For the tearing conditions exhibited in red, a similar behavior to the splaying setup can be appreciated with a higher SEA given the different failure modes related to the tearing setup.

For the corrugated setup, the results are presented in figure 4.60 in which a SEA-crushing velocity curve exhibits a small slope after the trigger effect has been surpassed, meaning that the SEA increases as the crushing velocity is reduced, adding a peak SEA at approximately 2 $m \cdot s^{-1}$ followed by a decay in the SEA.

Following the discrete approach results, it can be observed that the crushing velocity has an impact on this material, with lower crushing velocities being the zone where the CF-PA66 absorbs the most energy.

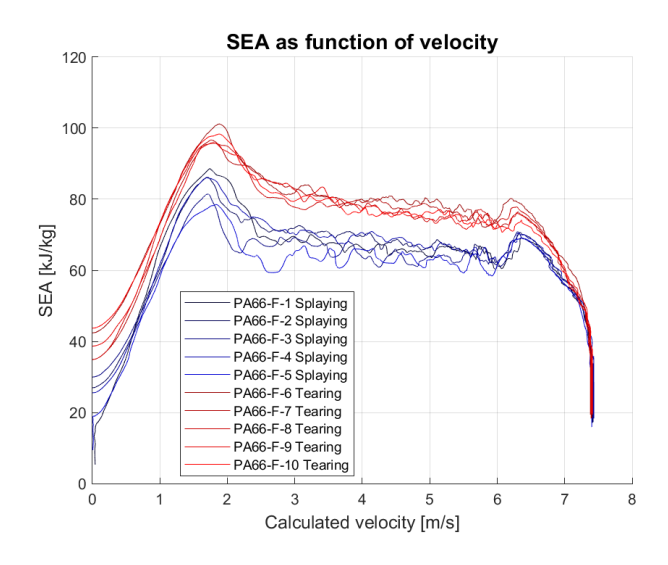


Figure 4.59: $SEA(\dot{x})$ -Crushing velocity curve for splaying and tearing setup CF-PA66.

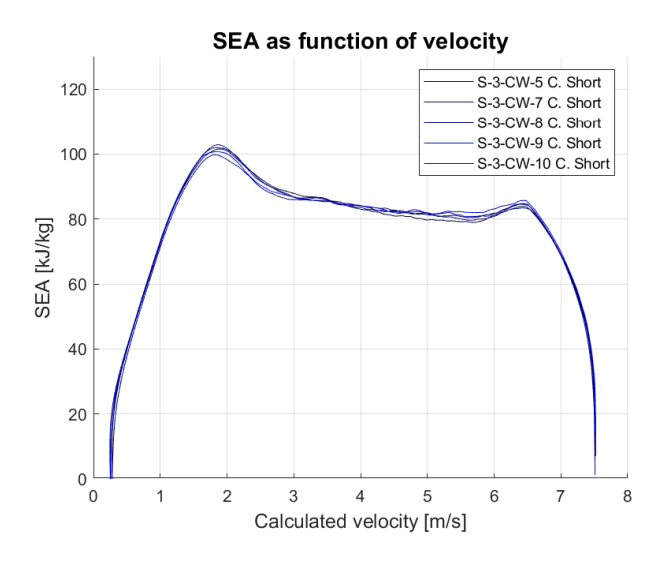


Figure 4.60: $SEA(\dot{x})$ -Crushing velocity curve for short corrugated setup CF-PA66.

CF-PC

Figure 4.61 shows the results for the splaying and tearing setups presented in a SEA-crushing velocity curve; both setups exhibited similar behavior in terms of a broad distribution of the SEA and a stable plateau after the trigger effect was surpassed. At low crushing velocities, there was an SEA decay for both setups.

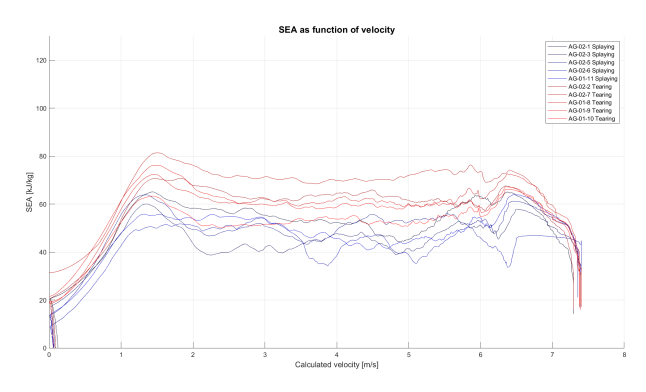


Figure 4.61: $SEA(\dot{x})$ -Crushing velocity curve for splaying and tearing setup CF-PC.

For the corrugated setup, the results are displayed in Figure 4.62 The curve exhibits stable behavior with a horizontal trend after the trigger effect has been surpassed. The previous analysis was consistent, showing no influence of the crushing velocity.

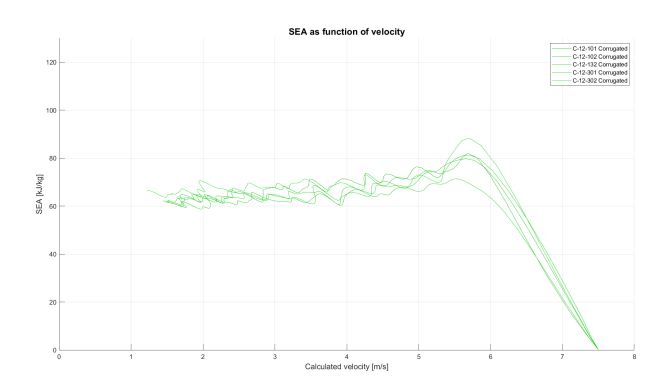


Figure 4.62: $SEA_{(\dot{x})}$ -Crushing velocity curve for short corrugated setup CF-PC.

GF-TEPEX

As observed in the previous study, this material was only possible to study the whole range for crushing velocity at the tearing setup; however, in Figure 4.63, the high-speed range for the $SEA_{(\dot{x})}$ is characterized by a disperse data of SEA and is not possible to address any trend. For the tearing setup (red), a slight increase in the SEA was observed as the crushing velocity decreased.

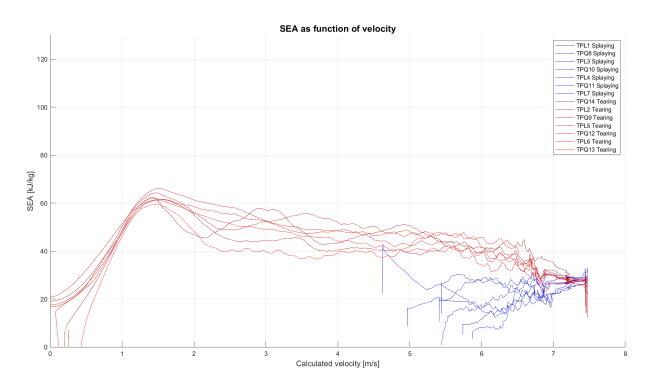


Figure 4.63: $SEA(\dot{x})$ -Crushing velocity curve for splaying and tearing setup GF-TEPEX.

Figure 4.64 presents the SEA velocity curve, in which the SEA of the material exhibits a relatively horizontal plateau but with a relatively high noise at its plateau, and no visible trends can be inferred.

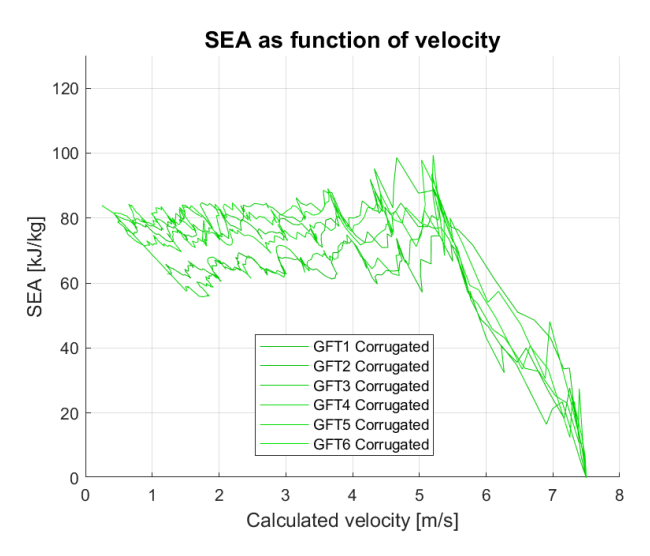


Figure 4.64: $SEA(\dot{x})$ -Crushing velocity curve for corrugated setup GF-TEPEX.

GF-PP

Figure 4.65 shows the SEA-crushing velocity curve for the splaying and tearing setups. It is characterized by both setups and an abrupt cut at relatively high speeds. Notably, in the experimental testing results, a lack of energy

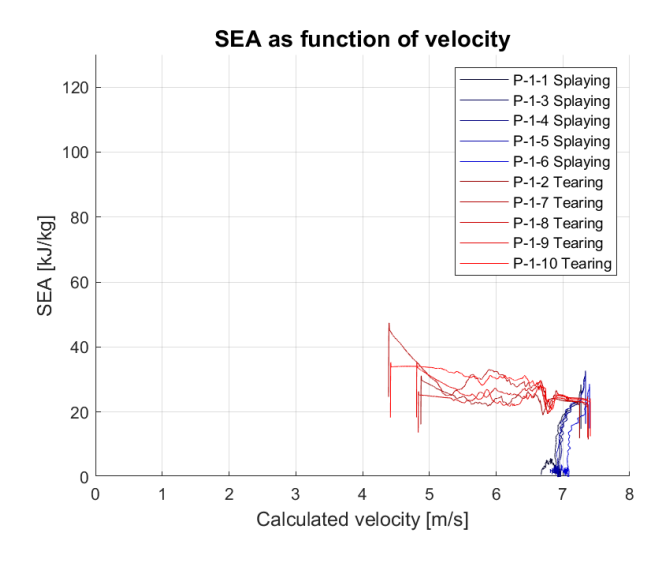


Figure 4.65: $SEA(\dot{x})$ -Crushing velocity curve for splaying and tearing setup GF-PP.

absorption and full inter-delamination of the specimens were observed in the experimental results. This explains the splaying setup behavior in blue, whereas for the tearing after the trigger effect, a plateau was observed, which stopped at relatively high speeds.

The short corrugated coupons results tested at Instron are exhibit in the figure 4.66 the SEA-crushing velocity curve presents a clear slope as the velocity decreases indicating that the material has a better performance at lower speeds and that the geometry plays a key factor for SEA.

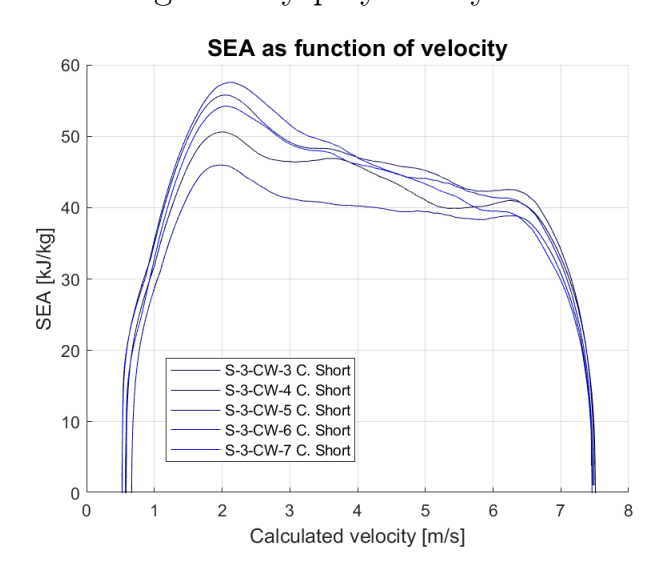


Figure 4.66: $SEA(\dot{x})$ -Crushing velocity curve for short corrugated setup GF-PP.

The results for the corrugated coupons with the IVW geometry are shown in Figure 4.67 as a SEA-crushing velocity curve. The results were characterized by a smaller slope than that of the short corrugated coupons; however,

there was a slight trend for the SEA to increase as the crushing velocity was reduced.

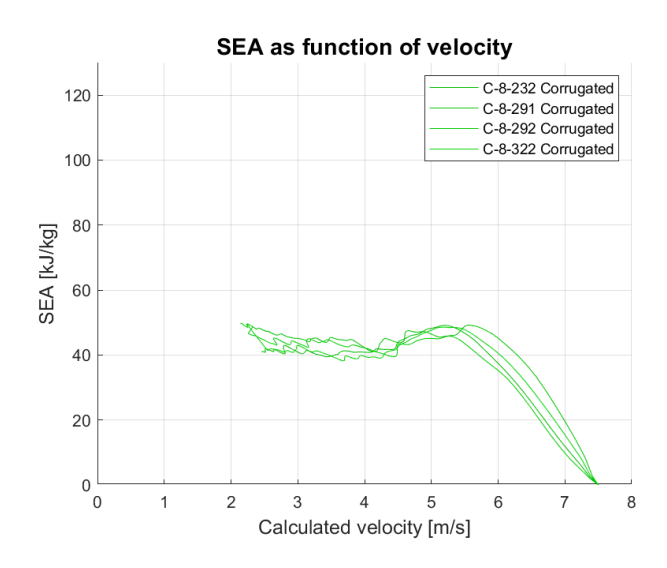


Figure 4.67: $SEA(\dot{x})$ -Crushing velocity curve for IVW corrugated setup GF-PP.

4.3 Statistical Fitting Models

Subsequent to data processing, there exists an opportunity to identify a model capable of understanding the influence of geometry, as demonstrated in various types of corrugated coupons, and their relationship with flat coupons, which are anticipated to exhibit a geometric influence. This is particularly relevant given the limited number of studies in the literature that address the impact of geometry on the performance of composites. The models considered in this analysis are as follows, with each model evaluated using linear, exponential, and logarithmic statistical fitting models to determine the best fit:

Number of curvatures

This initial model considers the number of curvatures present in the coupons as the primary parameter of reference. Specifically, in the context of flat coupons, there are two potential setups. In the Splaying setup, because there are no pillars at the base of the fixture to constrain the coupon, a value of zero curvatures is assigned. Conversely, in the Tearing setup, three pillars constrain the setup, which are considered the number of curvatures.

Material	$R^2 - Coeff$. Linear Model	$R^2 - Coeff$. Exp. Model	$R^2 - Coeff$. Log. Model
CF-Epoxy	0.86 [-]	0.84 [-]	0.85 [-]
CF-PA66	0.94 [-]	0.93 [-]	0.95 [-]
CF-PA6	0.15 [-]	0.14 [-]	0.25 [-]
CF-PC	0.67 [-]	0.64 [-]	0.78 [-]
GF-TEPEX	0.93 [-]	0.88 [-]	0.89 [-]
GF-PP	0.96 [-]	0.49 [-]	0.98 [-]

Table 4.10: Unaltered SEA $R^2 - Coeff$. for linear, exponential and logarithmic statistical fitting models.

Material	$R^2 - Coeff$. Linear Model	$R^2 - Coeff$. Exp. Model	$R^2 - Coeff$. Log. Model
CF-Epoxy	0.86 [-]	0.84 [-]	0.85 [-]
CF-PA66	0.94 [-]	0.93 [-]	0.95 [-]
CF-PA6	0.15 [-]	0.14 [-]	0.25 [-]
CF-PC	0.67 [-]	0.64 [-]	0.78 [-]
GF-TEPEX	0.93 [-]	0.88 [-]	0.89 [-]
GF-PP	0.96 [-]	0.49 [-]	0.98 [-]

Table 4.11: Normalized SEA $R^2 - Coeff$. for linear, exponential and logarithmic statistical fitting models.

This is illustrated in Figure 4.68, which depicts the number of curvatures in the coupons used during the experimental testing.



Figure 4.68: (A) Splaying setup coupon, (B) Tearing setup coupon, (C) IVW Geometry coupon, each of the coupons exhibit different number of curvatures.

After defining the primary parameter, statistical fitting models were developed using a MATLAB script, which was provided with the SEA input for each experimental test case. To enhance comprehensibility, three distinct input methodologies were employed: unaltered SEA, normalized SEA, and SEA normalized to the mean of the corrugated coupons.

As shown in Tables 4.10, 4.11, and 4.12, the statistical parameters remain constant following the normalization of the SEA, as the proportions are maintained. It is also apparent that the fitting models exhibit varying performance across different material cases. Notably, the logarithmic model demonstrated a good fit for most materials, except for CF-PA6, where the model performed poorly in capturing the trend. This observation may indi-

Material	$R^2 - Coeff$. Linear Model	$R^2 - Coeff$. Exp. Model	$R^2 - Coeff$. Log. Model
CF-Epoxy	0.86 [-]	0.84 [-]	0.85 [-]
CF-PA66	0.94 [-]	0.93 [-]	0.95 [-]
CF-PA6	0.15 [-]	0.14 [-]	0.25 [-]
CF-PC	0.67 [-]	0.64 [-]	0.78 [-]
GF-TEPEX	0.93 [-]	0.88 [-]	0.89 [-]
GF-PP	0.96 [-]	0.49 [-]	0.98 [-]

Table 4.12: SEA normalized to the mean of the corrugated coupons $R^2 - Coeff$. for linear, exponential and logarithmic statistical fitting models.

cate that the CF-PA6 material is not significantly influenced by the number of curvatures in the geometry.

The $R^2-Coefficient$ can range from zero to one, with zero indicating that the model does not characterize the behavior of the data, while a value of one describes a perfect fit, although $R^2-Coeff$. is great for statistically describing the data behavior, it is necessary to also understand the average magnitude of the errors between the data and the fitting curve. For this purpose, the RMSE parameter is obtained, and Table 4.13 describes the RMSE for this statistical fitting model, being aware that the proportions are kept equal is only relevant to present only one case being the chosen one the normalized SEA.

Material	RMSE – Coeff.	RMSE – Coeff.	RMSE – Coeff.
	Linear Model	Exp. Model	Log. Model
CF-Epoxy	0.078 [-]	0.076 [-]	0.082 [-]
CF-PA66	0.022 [-]	0.022 [-]	0.020 [-]
CF-PA6	0.075 [-]	0.072 [-]	0.071 [-]
CF-PC	0.073 [-]	0.071 [-]	0.060 [-]
GF-TEPEX	0.079 [-]	0.098 [-]	0.096 [-]
GF-PP	0.074 [-]	0.253 [-]	0.055 [-]

Table 4.13: Normalized SEA RMSE for linear, exponential and logarithmic statistical fitting models.

In Figure 4.69, the linear fitting model for all six materials is shown as a continuous line, while the experimental data of each of the coupons are represented by different symbols, as shown in Table 4.11 The models exhibit a good fit, except for CF-PA6, and for GF-PP, it can be observed that the model does not follow the correct form of convergence after the number of curvatures exceeds five.

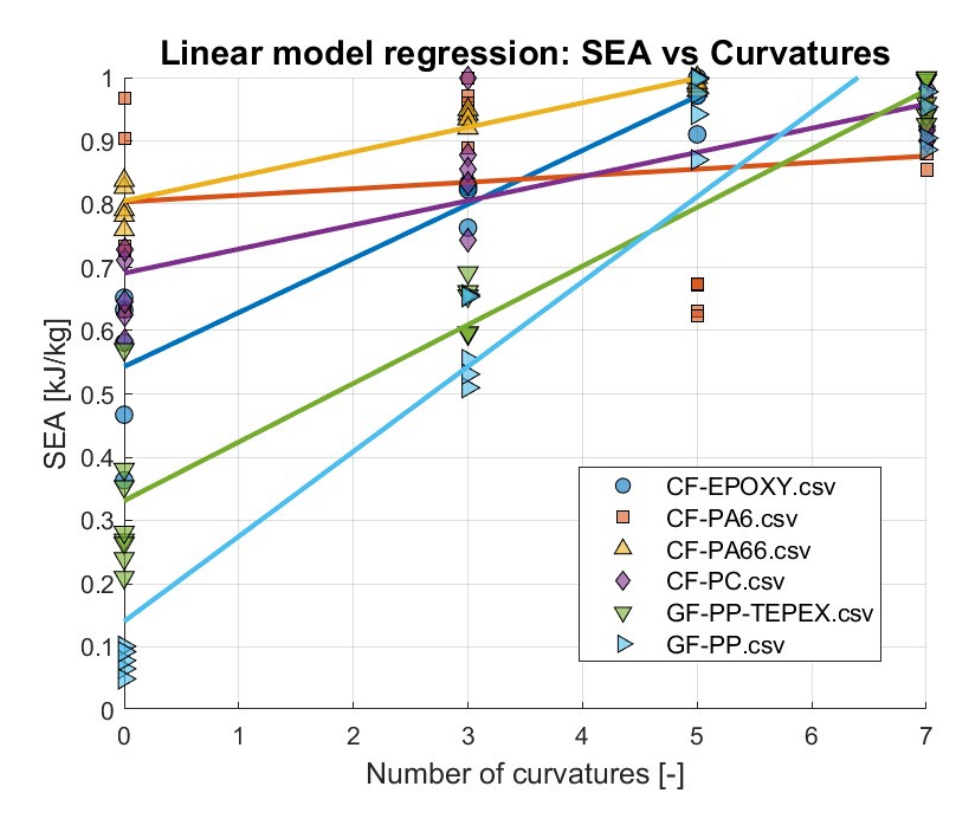


Figure 4.69: Linear statistical fitting model curve for the parameter of number of curvatures.

Figure 4.70 shows the exponential model for the number of curvatures in the $R^2 - Coeff$. this model exhibits the worst-case scenario in terms of fitting; in this figure, it can be appreciated how the model lacks in terms of characterizing the trend as the number of curvatures increases, being out of fit for a larger number of curvatures.

Figure 4.71 shows the curve for the logarithmic fitting model of the number of curvatures. In Table 4.11 this model exhibited the best fit compared to the previous two. In the figure, it can be observed how the convergence of the coupons with curvatures is well characterized. Again, the material CF-PA6 shows a poor fitting performance, with the experimental data being completely outside the model at approximately five curves.

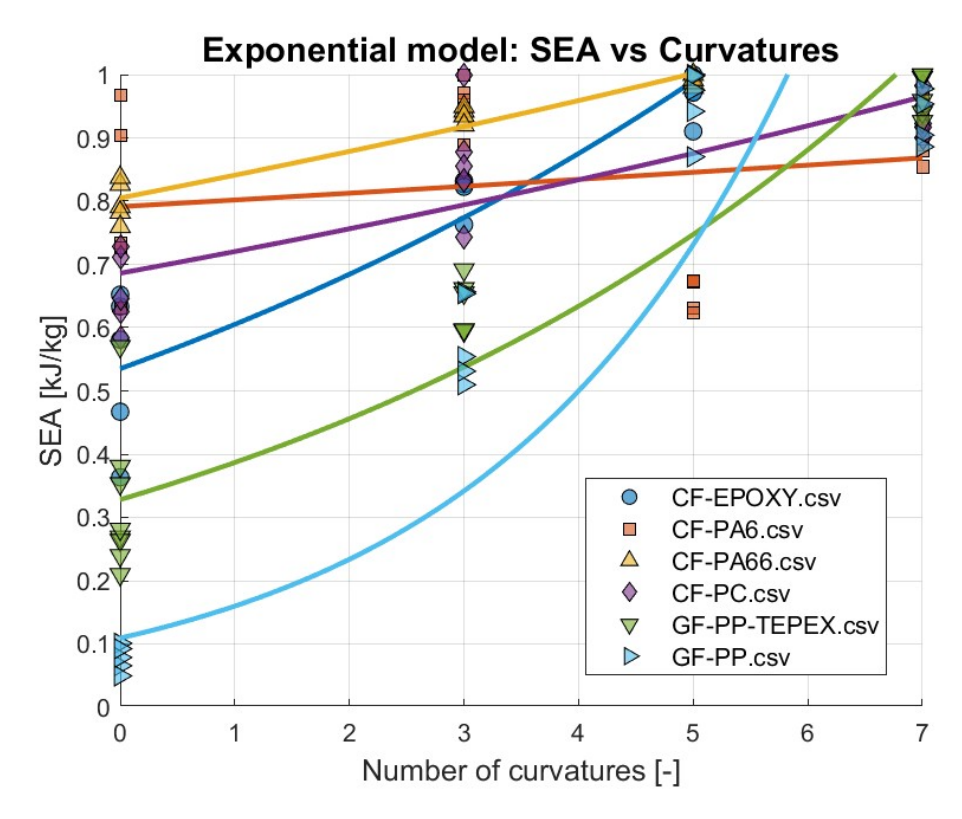


Figure 4.70: Exp. statistical fitting model curve for the parameter of the number of curvatures.

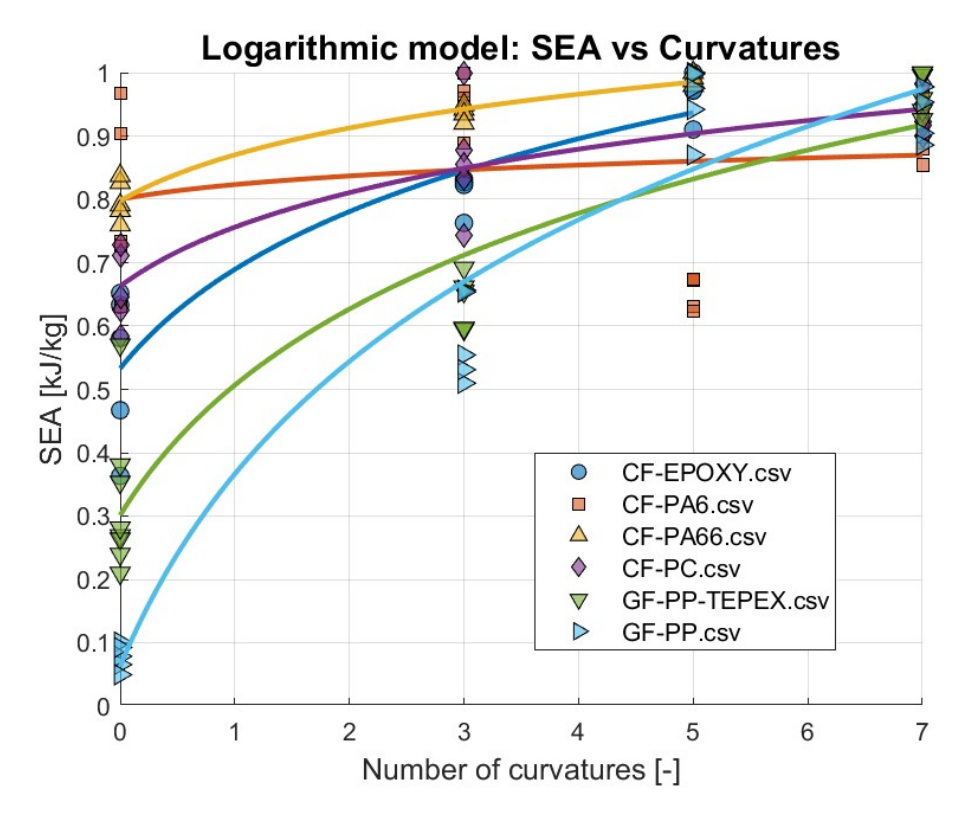


Figure 4.71: Log. statistical fitting model curve for the parameter of the number of curvatures.

Rate of total length over distance in between fixing points

This model considers the parameter for characterizing the rate between the total length of the coupon over the center of the fixing points or curvatures of the corrugated geometric coupons, as described in Figure 4.72. In the case of a complex geometry, such as Feraboli or IVW, the fixing point distance is considered to be shorter.

$$R = \frac{Total\ length\ of\ the\ fixing\ points}{Distance\ in\ between\ smallest\ fixing\ points} \tag{4.1}$$

For flat coupons, two possible R values are obtained depending on the setup of the test to be performed. For the splaying setup conditions, because there are no relative fixing points constraining the coupons at the failure contact point, R=0 [-], whereas for the tearing setup, R=2 [-]. For the corrugated coupons, since three different geometries were used during the experimental testing, the R parameter is intrinsic for each of them, being Feraboli geometry R=3.41 [-], Short IVW (Instron Geometry) R=3.82 [-], and IVW geometry R=6.05 [-].

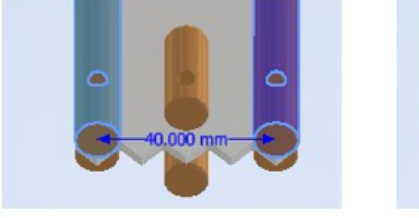




Figure 4.72: Left figure the total length for the fixing points in a tearing setup for flat coupon. The right figure is the length in between the smallest distance of fixing points for flat coupon under a tearing setup.

As for previous models, a MATLAB script was used to process all the statistical fitting models and obtain the statistical parameters to understand how well the model fit. Tables 4.14, 4.15 and 4.16 show the statistical parameter $R^2 - Coefficient$ found for each of the three cases: unaltered SEA, normalized SEA, and normalized SEA with the mean of the corrugated SEA for each of the six materials tested.

Material	$R^2 - Coeff$. Linear Model	$R^2 - Coeff$. Exp. Model	$R^2 - Coeff$. Log. Model
CF-Epoxy	0.86 [-]	0.84 [-]	0.85 [-]
CF-PA66	0.90 [-]	0.89 [-]	0.95 [-]
CF-PA6	0.11 [-]	0.10 [-]	0.20 [-]
CF-PC	0.60 [-]	0.57 [-]	0.74 [-]
GF-TEPEX	0.90 [-]	0.83 [-]	0.92 [-]
GF-PP	0.91 [-]	0.45 [-]	0.99 [-]

Table 4.14: Unaltered SEA $\mathbb{R}^2-Coeff$. for linear, exponential and logarithmic statistical fitting models.

Material	$R^2 - Coeff$. Linear Model	$R^2 - Coeff$. Exp. Model	$R^2 - Coeff$. Log. Model
CF-Epoxy	0.86 [-]	0.84 [-]	0.85 [-]
CF-PA66	0.90 [-]	0.89 [-]	0.95 [-]
CF-PA6	0.11 [-]	0.10 [-]	0.20 [-]
CF-PC	0.60 [-]	0.57 [-]	0.74 [-]
GF-TEPEX	0.90 [-]	0.83 [-]	0.92 [-]
GF-PP	0.91 [-]	0.45 [-]	0.99 [-]

Table 4.15: Unaltered SEA $\mathbb{R}^2-Coeff$. for linear, exponential and logarithmic statistical fitting models.

Material	$R^2 - Coeff$. Linear Model	$R^2 - Coeff$. Exp. Model	$R^2 - Coeff$. Log. Model
CF-Epoxy	0.86 [-]	0.84 [-]	0.85 [-]
CF-PA66	0.90 [-]	0.89 [-]	0.95 [-]
CF-PA6	0.11 [-]	0.10 [-]	0.20 [-]
CF-PC	0.60 [-]	0.57 [-]	0.74 [-]
GF-TEPEX	0.90 [-]	0.83 [-]	0.92 [-]
GF-PP	0.91 [-]	0.45 [-]	0.99 [-]

Table 4.16: Unaltered SEA $R^2 - Coeff$. for linear, exponential and logarithmic statistical fitting models.

As for the previous model, because the proportions are maintained while the normalization is performed, the statistical parameter $R^2 - Coefficient$ is kept constant along the three different calculations. For this model, a poor fitting performance was observed for the exponential model, having only three materials above a $0.8 R^2 - Coefficient$, while linear and logarithm models had a good performance for most of the materials. It is important to note that, as for the previous model, the material CF-PA6 did not achieve a model capable of describing its behavior, and all fitting models $R^2 - Coefficient$ are low.

Material	RMSE – Coeff.	RMSE – Coeff.	RMSE – Coeff.
Materiai	Linear Model	Exp. Model	Log. Model
CF-Epoxy	0.079 [-]	0.077 [-]	0.081 [-]
CF-PA66	0.027 [-]	0.027 [-]	0.019 [-]
CF-PA6	0.077 [-]	0.073 [-]	0.073 [-]
CF-PC	0.080 [-]	0.077 [-]	0.064 [-]
GF-TEPEX	0.09 [-]	0.113 [-]	0.081 [-]
GF-PP	0.114 [-]	0.263 [-]	0.036 [-]

Table 4.17: Normalized SEA RMSE for linear, exponential and logarithmic statistical fitting models.

Because the proportions are maintained after normalization and to make possible the comparison between models, normalized data are chosen to show the other important statistical parameter RMSE, which describes the average magnitude of the errors between the data and the fitting curve. Table 4.17 presents the RMSE for the normalized SEA of the rate of distance model. Compared to the previous model, a similar output was again found, with the exponential model having the poorest performance.

Figure 4.73 presents the curve for the linear model, which presents a good statistical fit with a low RMSE for most of the materials, except for CF-PA6 and GF-PP. It can be observed how the fitting model performs, being able to characterize the experimental data; however, the data seem to reach convergence as the rate of distance increases, and this model cannot follow that trend.

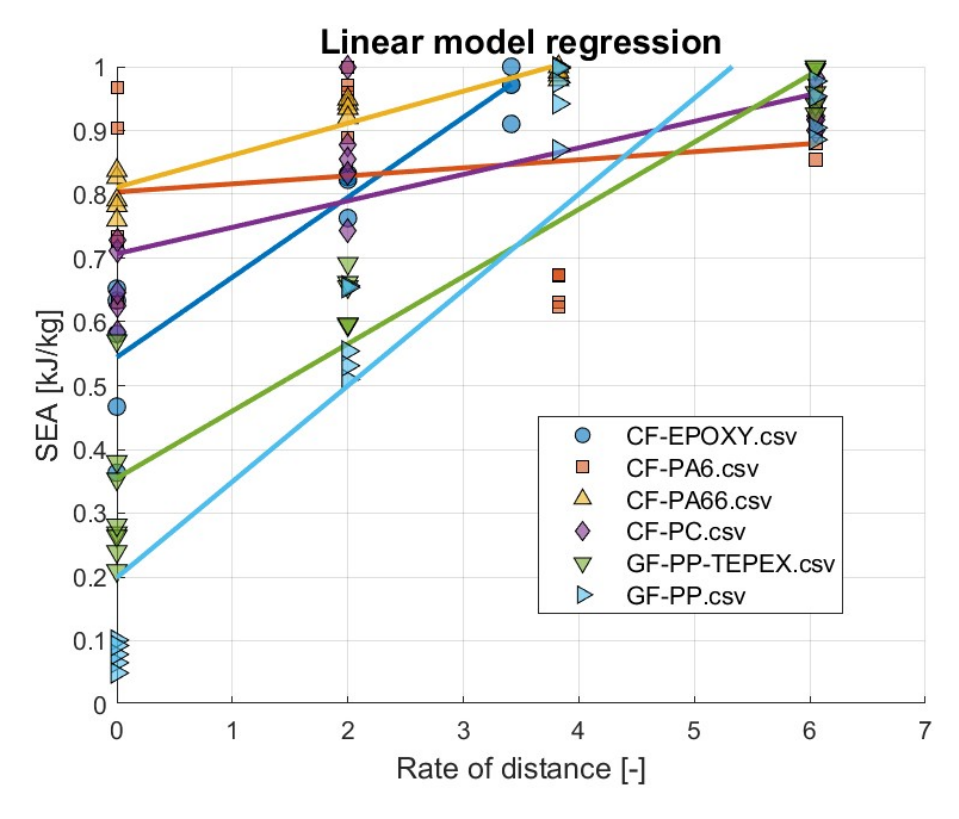


Figure 4.73: Linear statistical fitting model curve for the parameter Rate of distance.

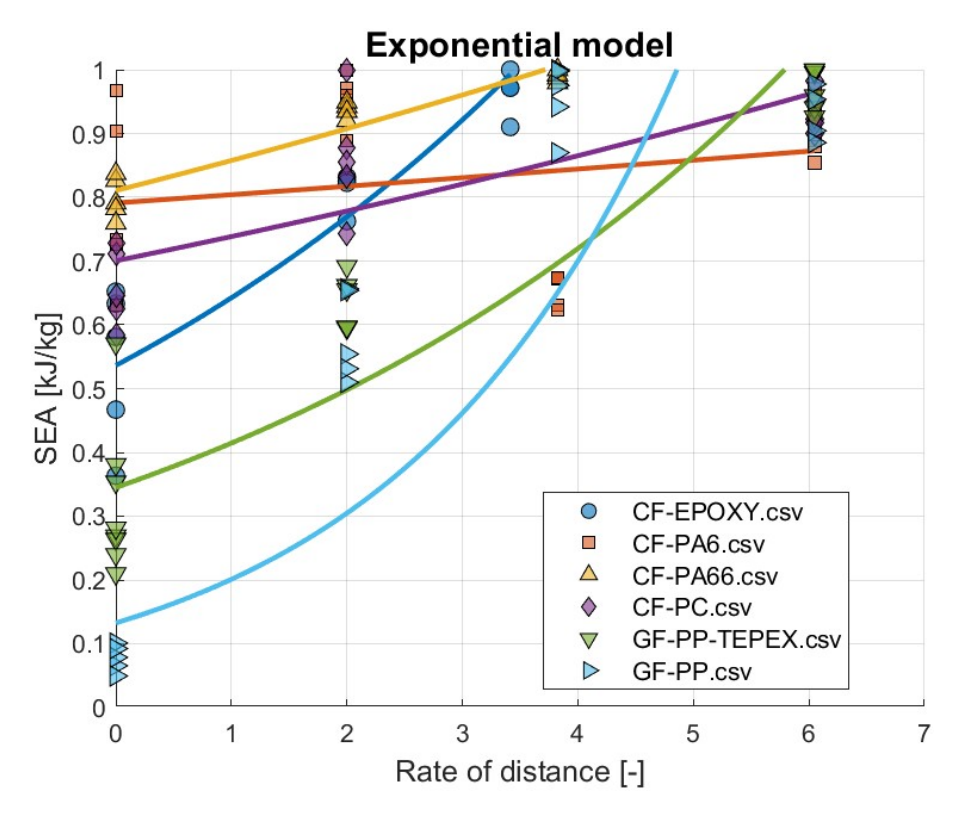


Figure 4.74: Exp. statistical fitting model curve for the parameter Rate of distance.

The exponential fitting model for the parameter of rate of distance is presented in figure 4.74, which is characterized by an increase in the SEA as the rate of distance increases. This trend is not followed by the experimental data, as the statistical parameters indicate that this model is not capable of realistically characterizing the behavior of the material.

Figure 4.75 presents the logarithmic model for the rate of distance. According to the results for the statistical parameters, this model presents the best characterization of the material behavior, as observed in the curve. The fitting model can follow the convergence trend of the SEA as the rate of the distance parameter increases, except for the GF-PP and CF-PA6, for which the model cannot characterize the experimental data.

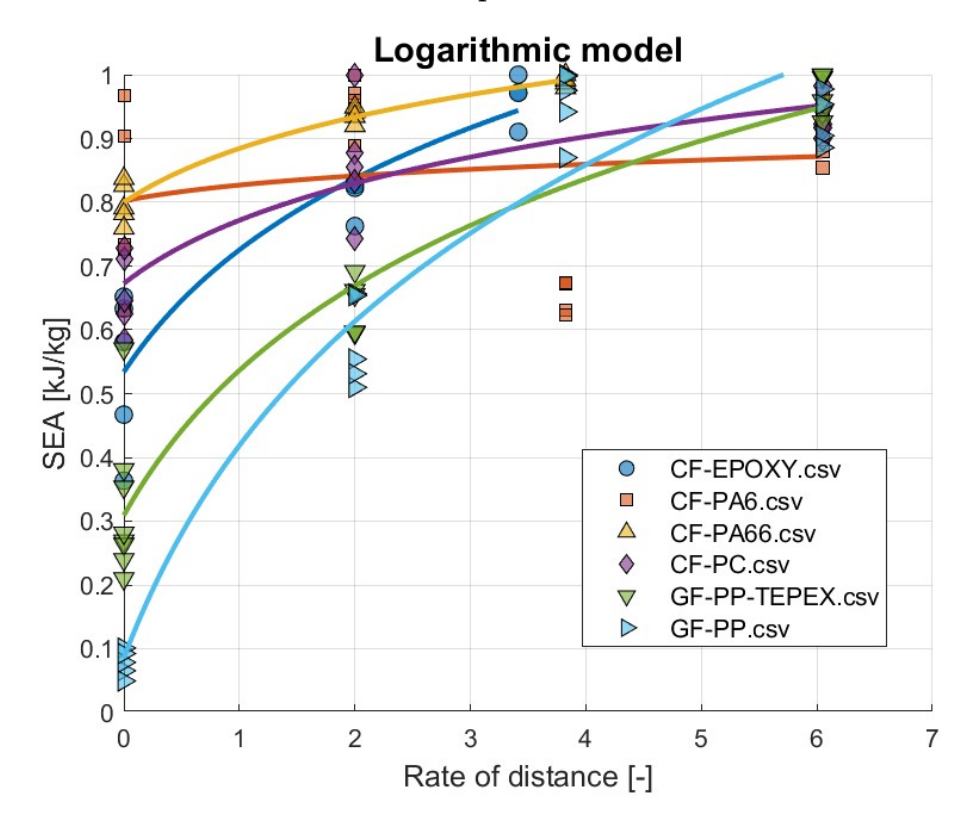


Figure 4.75: Log. statistical fitting model curve for the parameter Rate of distance.

4.4 Data Validation

As clarified in the Methodology section, the experimental data were collected from two distinct institutions, each employing a different setup. Consequently, it is imperative to confirm the comparability of the data being processed in the model. To this end, a statistical null hypothesis test was conducted on the two materials, CF-PA6 and GF-PP. Statistical analysis necessitates the formulation of a null hypothesis, H_0 , and an alternative hypothesis, H_a .

• H_0 : The mean SEA of the coupons tested at Instron is equal to the mean SEA of coupons tested at IVW.

$$H_0: \mu_{Instron} = \mu_{IVW} \tag{4.2}$$

• H_a : The mean SEA of the coupons tested at Instron is different to the mean SEA of coupons tested at IVW.

$$H_a: \mu_{Instron} \neq \mu_{IVW}$$
 (4.3)

For both materials, the fixing significance level will be defined at the Error Type I (α) with a confidence level of 5 %, therefore the Error type II (β) will remain a function of the degrees of freedom of each of the materials.

CF-PA6

The input for the statistical analysis was the statistical parameter data for the corrugated coupons shown in Table 4.18, which was processed using a MATLAB script that computes the statistical parameters of the mean, standard deviation, and degrees of freedom.

Statistical Parameter	Short Corrugated	IVW Corrugated
Mean	$59.8 \ [kJ \cdot kg^{-1}]$	$83.8 \ [kJ \cdot kg^{-1}]$
STD.	$1.04~[kJ\cdot kg^{-1}]$	$1.02~[kJ\cdot kg^{-1}]$
Degrees of freedom	5 [DOF]	11 [DOF]

Table 4.18: Statistical Parameters of CF-PA6 for the null hypothesis analysis.

The results obtained using the MATLAB script are listed in Table 4.19.

Statistical Parameter	Results
Type I Error	0.05 [-]
Type II Error	0.00 [-]
Critical T_{value}	$\pm 2.14 [-]$
$T_{Statistical}$	14.24 [-]

Table 4.19: Null Hypothesis results for CF-PA6 to the evaluation of H_0

Based on the results, it can be inferred with 95% confidence that H_0 is false, and there is a 0% probability of failing to reject it when it is indeed false. Given these results, it is not feasible to compare the experimental data between the two testing institutes. The examination of the statistical parameters indicated the underperformance of the coupons tested at the Instron facilities. Consequently, further investigation is warranted to determine whether defects were present in the coupons that may have influenced the material performance or whether biases in the testing facilities inhibited a valid comparison of the experimental data.

To assess the defects of the coupons, a CT-Scan was performed at the facilities of Politecnico di Torino in one of the coupons that was not tested to determine whether there were any imperfections or manufacturing defects. This means that the coupons could have had some voids formed while the matrix was infused in the fibers or a delamination occurred during the curing process, which explains the dramatic underperformance of the material, which had a significant 40% difference in SEA with respect to the IVW specimens.

Figure 4.76 presents the results of the CT-Scan, revealing several manufacturing defects. The figure on the left displays multiple interlaminar microvoids throughout the coupon. The central figure indicates the initiation of delamination accompanied by voids, whereas the figure on the right shows additional voids within the coupon. This analysis demonstrated that the coupon exhibited manufacturing defects along its entire length, which may account for the discrepancies in the Specific Energy Absorption (SEA) between the Instron and IVW. As it was not feasible to obtain another batch of coupons to restart the testing of CF-PA6, this material was not utilized to validate the comparison of data between the two institutions.



Figure 4.76: Manufacturing defects presented in a CF-PA6 coupon by a CT-Scan.

GF-PP

The experimental data from the SEA were the main input for the MATLAB script, and Table 4.20 presents the statistical parameters for this material. It is important to note the low DOF for this statistical test, which is translated into a high Type II Error due to the lack of power of the test.

Statistical Parameter	Short Corrugated	IVW Corrugated
Mean	$43.1 \ [kJ \cdot kg^{-1}]$	$41.9 [kJ \cdot kg^{-1}]$
STD.	$2.43 \ [kJ \cdot kg^{-1}]$	$1.92 \ [kJ \cdot kg^{-1}]$
Degrees of freedom	5 [DOF]	4 [DOF]

Table 4.20: Statistical Parameters of GF-PP for the null hypothesis analysis.

The results obtained using the MATLAB script are listed in Table 4.21.

Statistical Parameter	Results
Type I Error	0.05 [-]
Type II Error	0.92 [-]
$Critical\ T_{value}$	$\pm 2.36 [-]$
$T_{Statistical}$	-0.81 [-]

Table 4.21: Null Hypothesis results for GF-PP to the evaluation of H_0

The results of the null hypothesis test indicate the acceptance of hypothesis H_0 . This suggests, with 95 % confidence, that the results between Instron and IVW exhibit the same Specific Energy Absorption (SEA). However, the $\beta = 0.92$, which represents the probability of failing to reject H_0 when it is false, is notably high. This elevated probability is primarily attributed to the low degree of freedom available for testing. Nonetheless, given these

results, it can be asserted that the experimental data produced by the two institutions are comparable and reliable. Consequently, with this validation, the fitting and predictive models can be considered reliable, provided that they are statistically representative.

4.5 Predictive Models

Following the identification of the key parameters that influence the fitting of experimental data within statistical fitting models, this section elaborates on the development of predictive models. These models utilize the identified parameters to forecast the impact of geometry on the specific energy absorption (SEA) of a material. Additionally, they aimed to understand and predict the SEA of various geometric configurations from flat coupons, which should be unbiased by geometry.

Two primary parameters were identified as the most effective in fitting the material behavior trends: the number of curvatures and the ratio of the total length to the distance between the fixing points (hereafter referred to as the rate of distance). For each parameter, predictive models were constructed based on the most effective statistical fits, that is, linear and logarithmic regression models, as previously determined in this section.

The predictive framework, illustrated conceptually in Figure 3.7, operates as follows.

- 1. **Input**, The SEA values for the flat coupons for both testing setups Splaying and Tearing are used as the principal base for the models.
- 2. **Model Fitting**, using a MATLAB scrip two main regression models were used (Linear and Logarithmic) creating the relationship between the geometric parameter and the SEA, the following equations were the main drivers for the regression models computation.

$$SEA_{(x)} = c \cdot ln(x+1) + d$$
 (4.4)

$$SEA_{(x)} = b \cdot x + a \tag{4.5}$$

- 3. **Prediction of the middle point**, This model is then used to compute the corrugated geometry SEA by inputting the specific parameter which is intrinsic of the geometry.
- 4. **Prediction of the uncertainty**, Since being capable of accurately predicting the mean of the SEA is complex due to the variability of the nature of composite materials a confidence interval is desired to asses the prediction of the SEA, this is achieved by using two distinct methods: the Covariance Matrix of Coefficients (CMC) and the Monte Carlo (MC) method, as described in Section 3.5.

Number of curvatures

The prediction model output is the mean and standard deviation of a single point of the parameter that is desired to be predicted. Because both uncertainty models are intrinsically linked to the experimental data from the flat coupons, the STD is not fixed but varies depending on the geometry to be predicted. Figure 4.77 presents the linear prediction curve for the number of curvatures model, with the model represented by a continuous line.

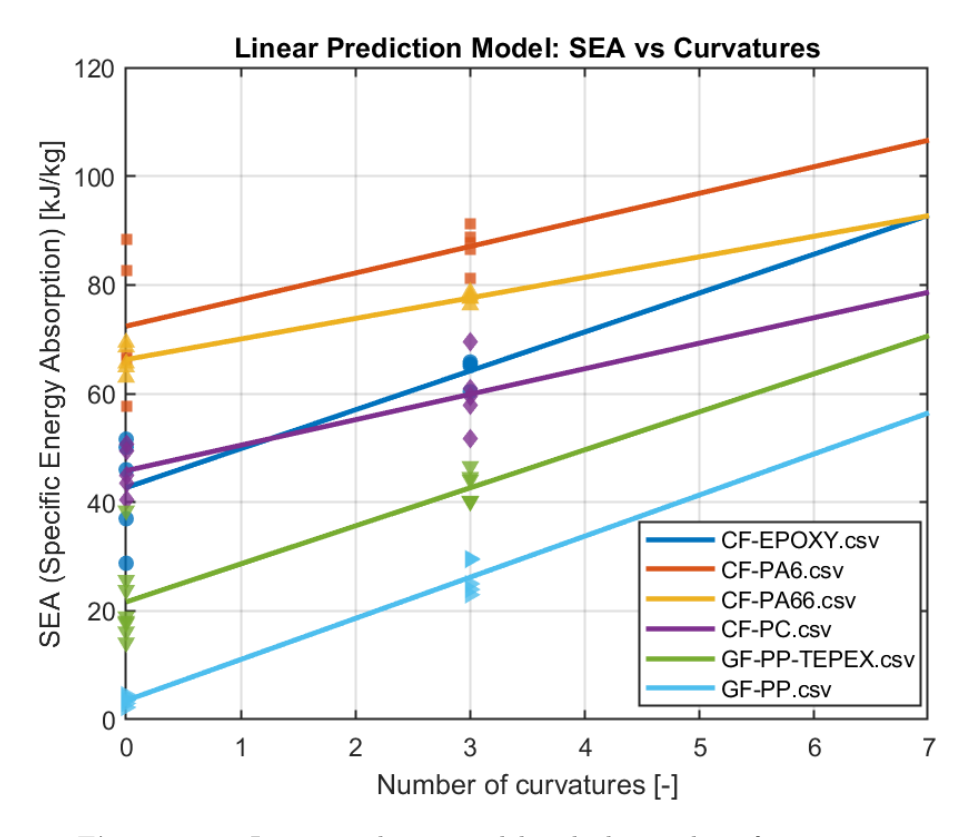


Figure 4.77: Linear predictive model with the number of curvatures.

For this model, Table 4.22 presents the STD of the corrugated coupons, which was set to be predicted. It is clearly observed how the CMC model offers a broader confidence interval than the Monte Carlo model, which is restricted to a narrow window of confidence interval. Given the experimental data, the MC model does not adequately represent the behavior of the composite materials. Therefore, in this prediction model, the CMC STD results were used for the prediction assessment.

Material	CMC	Model	MC Model			
Num. of curves $= 5$ Num. of curves $= 7$		Num. of curves $= 5$	Num. of curves $= 7$			
CF-EPOXY	$6.62 \ [kJ \cdot kg^{-1}]$	$9.81 \ [kJ \cdot kg^{-1}]$	$0.72 \ [kJ \cdot kg^{-1}]$	$0.71 \ [kJ \cdot kg^{-1}]$		
CF-PA6	7.51 $[kJ \cdot kg^{-1}]$	$11.24 \ [kJ \cdot kg^{-1}]$	$0.49 \ [kJ \cdot kg^{-1}]$	$0.49 \ [kJ \cdot kg^{-1}]$		
CF-PA66	1.59 $[kJ \cdot kg^{-1}]$	$2.39 \ [kJ \cdot kg^{-1}]$	$0.38 \ [kJ \cdot kg^{-1}]$	$0.38 \ [kJ \cdot kg^{-1}]$		
CF-PC	$4.37 \ [kJ \cdot kg^{-1}]$	$6.54 \ [kJ \cdot kg^{-1}]$	$0.47 \ [kJ \cdot kg^{-1}]$	$0.47 \ [kJ \cdot kg^{-1}]$		
GF-TEPEX	$4.48 \ [kJ \cdot kg^{-1}]$	6.61 $[kJ \cdot kg^{-1}]$	$0.70 \ [kJ \cdot kg^{-1}]$	$0.70 \ [kJ \cdot kg^{-1}]$		
GF-PP	$1.85 \ [kJ \cdot kg^{-1}]$	$2.77 \ [kJ \cdot kg^{-1}]$	$0.76 \ [kJ \cdot kg^{-1}]$	$0.76 \ [kJ \cdot kg^{-1}]$		

Table 4.22: Comparison of STD for linear model between CMC and MC Models for different materials.

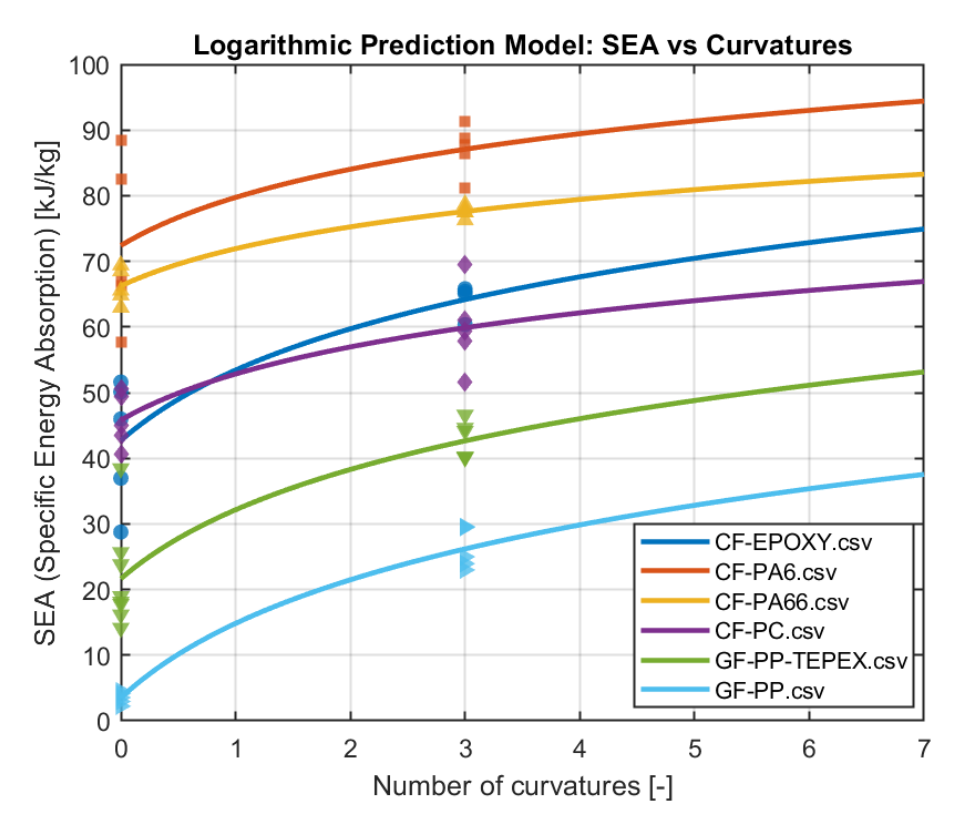


Figure 4.78: Log. predictive model with the number of curvatures.

Figure 4.78 presents the prediction model for the logarithmic regression of the number of curvature parameters. The curve is characterized by the

experimental data points assigned at point and the prediction models represented by a continuous line.

For the standard deviation, the two models were used to compute the uncertainty and build confidence intervals. The results of this computation are shown in Table 4.23 As for the previous model, the Monte Carlo model exhibited a restrictive approach, which was not representative of the composite material behavior during the experimental testing, whereas the CMC model presented an STD more adequate to the behavior of composite materials while also providing a wider confidence interval. For these reasons, as for the previous model, the Monte Carlo model will not be considered for the development of confidence intervals.

Material	CMC	Model	MC Model			
Num. of curves $= 5$ Num. of curves $= 7$		Num. of curves $= 5$	Num. of curves $= 7$			
CF-EPOXY	$4.93 \ [kJ \cdot kg^{-1}]$	$8.86 \ [kJ \cdot kg^{-1}]$	$0.26 \ [kJ \cdot kg^{-1}]$	$0.19 \ [kJ \cdot kg^{-1}]$		
CF-PA6	$5.54 \ [kJ \cdot kg^{-1}]$	6.61 $[kJ \cdot kg^{-1}]$	$0.18 \ [kJ \cdot kg^{-1}]$	$0.13 \ [kJ \cdot kg^{-1}]$		
CF-PA66	1.18 $[kJ \cdot kg^{-1}]$	1.40 $[kJ \cdot kg^{-1}]$	$0.14 \ [kJ \cdot kg^{-1}]$	$0.10 \ [kJ \cdot kg^{-1}]$		
CF-PC	$3.22 \ [kJ \cdot kg^{-1}]$	$3.85 \ [kJ \cdot kg^{-1}]$	$0.17 \ [kJ \cdot kg^{-1}]$	$0.13 \ [kJ \cdot kg^{-1}]$		
GF-TEPEX	$3.34 \ [kJ \cdot kg^{-1}]$	$3.96 \ [kJ \cdot kg^{-1}]$	$0.25 \ [kJ \cdot kg^{-1}]$	$0.19 \ [kJ \cdot kg^{-1}]$		
GF-PP	$1.37 \ [kJ \cdot kg^{-1}]$	1.63 $[kJ \cdot kg^{-1}]$	$0.27 \ [kJ \cdot kg^{-1}]$	$0.21 \ [kJ \cdot kg^{-1}]$		

Table 4.23: Comparison of STD for log. model between CMC and MC Models for different materials.

Rate of distance

The second parameter, which can fit the trend that follows the composite materials tested, is the rate of distance. The same approach as for the previous parameter was followed. Figure 4.79 presents the curve for the linear prediction model, presented with a continuous line as the predictive model, whereas the experimental data points are assigned by dot symbols depending on each material. With this model, only the mean prediction point was found, which can only provide a poor prediction of the real SEA of corrugated geometry coupons.

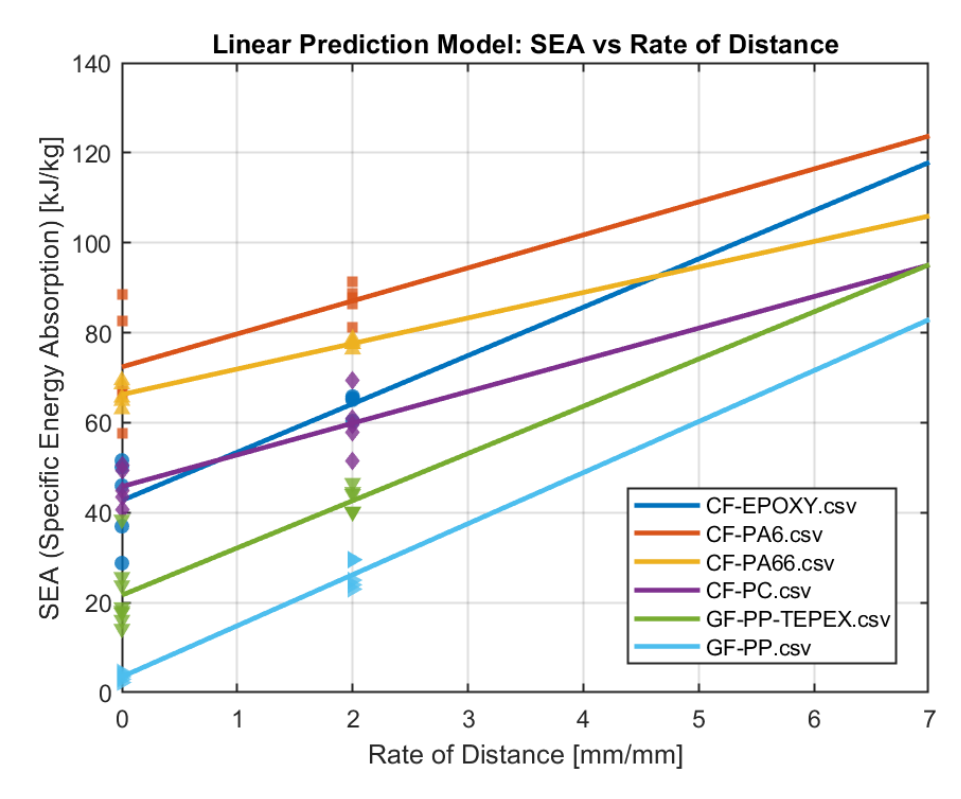


Figure 4.79: Linear predictive model with the Rate of distance parameter.

For the computation of the uncertainty defined by the STD given by the two models CMC and MC, Table 4.24 presents the computation for both of the models, compared to the previous parameter the STD exhibits a marginal increase for both of the models, the CMC model provides a similar STD to the base input of flat coupons which is translated into a more appropriate confidence interval, whereas the MC model presents a narrow confidence interval with a restrictive STD not relatable with the input of the flat coupons, given this the MC model was not considered for the build up of the confidence intervals.

Material	CMC	Model	MC Model			
Materiai	R = 3.82	R = 6.05	R = 3.82	R = 6.05		
CF-EPOXY	$10.62 \ [kJ \cdot kg^{-1}]$	$15.54 \ [kJ \cdot kg^{-1}]$	$1.07 \ [kJ \cdot kg^{-1}]$	$1.07 \ [kJ \cdot kg^{-1}]$		
CF-PA6	12.19 $[kJ \cdot kg^{-1}]$	$17.99 \ [kJ \cdot kg^{-1}]$	$0.73 \ [kJ \cdot kg^{-1}]$	$0.73 \ [kJ \cdot kg^{-1}]$		
CF-PA66	$2.59 \ [kJ \cdot kg^{-1}]$	$3.82 \ [kJ \cdot kg^{-1}]$	$0.57 \ [kJ \cdot kg^{-1}]$	$0.57 \ [kJ \cdot kg^{-1}]$		
CF-PC	7.10 $[kJ \cdot kg^{-1}]$	$10.46 \ [kJ \cdot kg^{-1}]$	$0.70 \ [kJ \cdot kg^{-1}]$	$0.70 \ [kJ \cdot kg^{-1}]$		
GF-TEPEX	7.15 $[kJ \cdot kg^{-1}]$	$10.44 \ [kJ \cdot kg^{-1}]$	$1.05 \ [kJ \cdot kg^{-1}]$	$1.04 \ [kJ \cdot kg^{-1}]$		
GF-PP	$3.01 \ [kJ \cdot kg^{-1}]$	$4.44 \ [kJ \cdot kg^{-1}]$	$1.13 \ [kJ \cdot kg^{-1}]$	$1.14 \ [kJ \cdot kg^{-1}]$		

Table 4.24: Comparison of STD for linear model between CMC and MC Models for different materials.

Finally, the last model, the logarithm prediction model with the parameter

of rate of distance, presented in Figure 4.80 is the curve that accounts for the prediction model capable of delivering the mean predicted value for the corrugated coupons exhibited with a continuous line, while the experimental data points of the flat coupons are presented with symbol dots assigned to each of the materials.

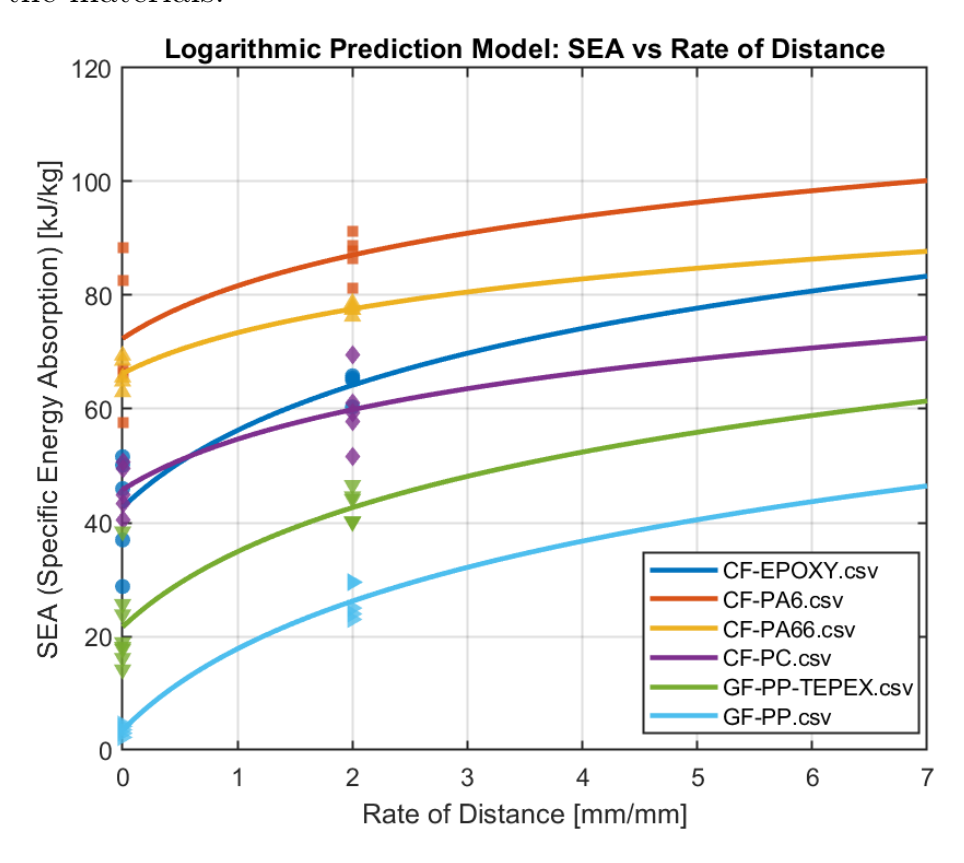


Figure 4.80: Log. predictive model with the Rate of distance parameter.

Table 4.25 presents the STD uncertainties from both the CMC and MC models. The model that is the most suitable for developing the confidence intervals is the CMC, given that the STD generated by it is more characteristic of composite materials, with a wider dispersion compared to the MC model, which offers a narrow and unrealistic for building a predictive model.

Material	CMC	Model	MC Model			
$R = 3.82 \qquad R = 6.05$		3.82 $R = 6.05$ $R = 3.82$		R = 6.05		
CF-EPOXY	$6.46 \ [kJ \cdot kg^{-1}]$	7.69 $[kJ \cdot kg^{-1}]$	$0.33 \ [kJ \cdot kg^{-1}]$	$0.24 \ [kJ \cdot kg^{-1}]$		
CF-PA6	7.31 $[kJ \cdot kg^{-1}]$	$8.75 \ [kJ \cdot kg^{-1}]$	$0.22 \ [kJ \cdot kg^{-1}]$	$0.17 \ [kJ \cdot kg^{-1}]$		
CF-PA66	$1.55 \ [kJ \cdot kg^{-1}]$	$1.86 \ [kJ \cdot kg^{-1}]$	$0.17 \ [kJ \cdot kg^{-1}]$	$0.13 \ [kJ \cdot kg^{-1}]$		
CF-PC	$4.25 \ [kJ \cdot kg^{-1}]$	$5.09 [kJ \cdot kg^{-1}]$	$0.21 \ [kJ \cdot kg^{-1}]$	$0.16 \ [kJ \cdot kg^{-1}]$		
GF-TEPEX	$4.36 \ [kJ \cdot kg^{-1}]$	$5.19 \ [kJ \cdot kg^{-1}]$	$0.32 \ [kJ \cdot kg^{-1}]$	$0.24 \ [kJ \cdot kg^{-1}]$		
GF-PP	$1.80 \ [kJ \cdot kg^{-1}]$	$2.16 \ [kJ \cdot kg^{-1}]$	$0.34 \ [kJ \cdot kg^{-1}]$	$0.26 \ [kJ \cdot kg^{-1}]$		

Table 4.25: Comparison of STD for Log. model between CMC and MC Models for different materials.

Chapter 5

Results and Discussion

5.1 Experimental Observations

This section synthesizes the key empirical findings from the crashworthiness testing of the six composite materials studied.

General Performance Trends: The experimental data confirmed the theory that energy absorption is highly dependent on the failure mode. Consistently across most materials (CF-epoxy, CF-PA66, CF-PC, GF-TEPEX, and GF-PP), the splaying setup, which was dominated by interlaminar delamination and friction, yielded the lowest SEA. The tearing setup, which forced fiber fracture and matrix cracking, yielded intermediate SEA values. The highest SEA was achieved by the corrugated coupons, which combine the benefits of multiple constrained failure mechanisms and higher structural stability.

Influence of Impact Velocity: The investigation into SEA as a function of crushing velocity revealed material-specific sensitivities.

- CF-PA66 showed a clear positive correlation between decreasing crushing velocity and increasing SEA, particularly in tearing and corrugated setups, suggesting a strain-rate sensitive behavior.
- GF-PP demonstrated a strong dependence on dynamic loading. Quasistatic tests revealed a stable, high-force plateau, whereas dynamic tests resulted in severe premature delamination and poor energy absorption. Variable-velocity tests further confirmed that higher impact velocities exacerbated this behavior, leading to a significant drop in performance.

Notable Exception CF-PA6: exhibited anomalous behavior. Its flat coupons, particularly in the tearing setup, exhibited surprisingly high SEA owing to fiber failure and brittle matrix fracture, whereas the splaying setup was characterized by a broad performance range, reaching the performance of corrugated coupons. More critically, the short corrugated coupons tested using the Instron significantly underperformed compared to the IVW-tested corrugated coupons. Subsequent CT scan analysis revealed widespread manufacturing defects, including interlaminar microvoids and delamination initiation, explaining this performance discrepancy and highlighting the critical impact of manufacturing quality on crashworthiness.

5.2 Confidence intervals

The base foundation for the confidence intervals was the predictive model, and the aim of the intervals was to provide a reasonable range of SEA for a specific chosen geometry, in this case, the number of curves in a coupon or the rate of distance between the total length and the minimum fixing points distance. For the construction of these intervals, the mean predicted value (μ) was first taken, and then the STD was added and subtracted, as defined in the following formula:

$$SEA_{Predicted} = \mu \pm STD_{CMC}$$
 (5.1)

This interval was then compared with the experimental data which was also converted into a confidence interval but in order to consider the 95 % of the possible values that the material can sustain according to the statistical *Student's t* distribution, for the development of this intervals the following equation was used:

$$SEA_{experimental} = \bar{x} \pm t_{\alpha,df} \cdot \frac{s}{\sqrt{n}}$$
 (5.2)

where the parameter $t_{\alpha,df}$ is given by the desired probability and the degrees of freedom available from the sample.

CF-Epoxy

Table 5.1 presents the confidence interval data for the experimental data of the material and the predicted values for each of the models. It is important to note that because the corrugated coupons were tested at the IVW, the predicted values account for that geometry.

	Experimental Data				Prediction model							
Model	Data IVW		Data Instron		Linear model		Log. model					
	Lower	Upper	Lower	Upper	Lower	Upper	Lower	Upper				
Number of curves - Short Corrugated	71.5 81.0				71.9	85.1	65.5	75.4				
Rate of distance - Short Corrugated		71.5 91.0	01.0	01.0	91 O	5 91.0			76.0	91.5	67.9	79.0
Number of curves - IVW Corrugated		81.0	_	_	83.0	102.6	69.1	80.8				
Rate of distance - IVW Corrugated					94.5	120.9	73.7	88.0				

Table 5.1: Confidence intervals data of Experimental Data and Prediction Models for CF-EPOXY (in all cases, values are given in $[kJ \cdot kg^{-1}]$).

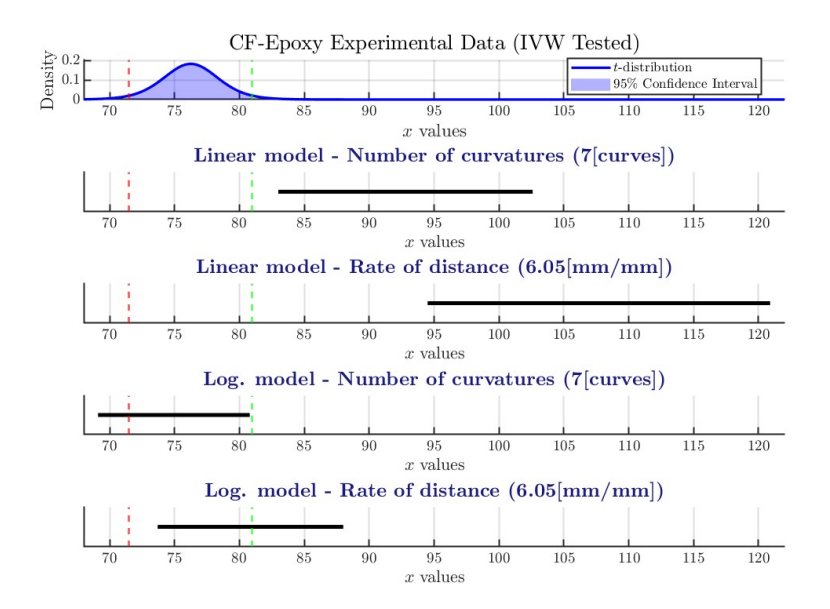


Figure 5.1: Confidence intervals curve of Experimental Data and Prediction Models for CF-EPOXY

Figure 5.1 presents the results for the predictive models and compares them with the t-distribution of the experimental data. The dashed lines show the range of values at which the experimental data can be found, followed from top to bottom by the linear models for both the number of curvatures and rate of distance, and finally, the same disposition but for logarithmic models. It is important to note that all materials presented this disposition to show

the results.

It can be observed that neither linear model can correctly predict the SEA, whereas the logarithmic models cover a range of experimental data. Subsequently, in the statistical validation, null hypothesis tests were performed to statistically assess the performance of each model.

CF-PA66

Table 5.2 and figure 5.2 presents the results for the confidence intervals computing the prediction for the geometry of short corrugated coupons tested at Instron. Here, only the two logarithm models are capable of covering a range of the experimental data values, with the last one rate of distance the only one covering all the range of experimental data.

	Experimental Data				Prediction model				
Model	Data IVW		Data Instron		Linear model		Log. model		
	Lower	Upper	Lower	Upper	Lower	Upper	Lower	Upper	
Number of curves - Short Corrugated	_	-			83.6	86.8	79.7	82.1	
Rate of distance - Short Corrugated			-	81.3	82.8	86.1	89.8	81.2	83.8
Number of curves - IVW Corrugated				_	_	01.3	02.0	90.3	95.1
Rate of distance - IVW Corrugated					97.3	103.8	84.7	88.1	

Table 5.2: Confidence intervals data of Experimental Data and Prediction Models for CF-PA66 (in all cases, values are given in $[kJ \cdot kg^{-1}]$).

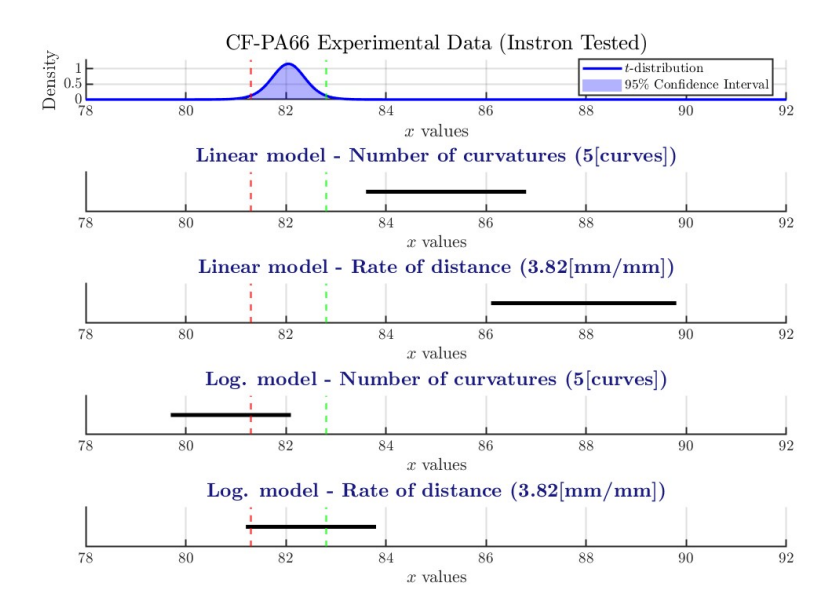


Figure 5.2: Confidence intervals curves of Experimental Data and Prediction Models for CF-PA66

CF-PA6

Table 5.3 presents the results of the predictive models and experimental data. Because tests were performed at both institutions, the table exhibits both datasets. Figure 5.3 presents the curves only for the results given for the Instron institution, which is not capable of correctly predicting the experimental data with any of the models.

	Experimental Data				Prediction model								
Model	Data IVW		Data Instron		Linear model		Log. model						
	Lower	Upper	Lower	Upper	Lower	Upper	Lower	Upper					
Number of curves - Short Corrugated	81.53	3 86.09			89.3	104.3	85.8	96.9					
Rate of distance - Short Corrugated			86.00	86.00	86.00	86.00	86.00	56.93	62.69	91.6	109.3	87.2	99.7
Number of curves - IVW Corrugated			00.93	02.09	95.4	117.9	87.8	101.0					
Rate of distance - IVW Corrugated					101.6	132.0	90.4	106.6					

Table 5.3: Confidence intervals data of Experimental Data and Prediction Models for CF-PA6 (in all cases, values are given in $[kJ \cdot kg^{-1}]$).

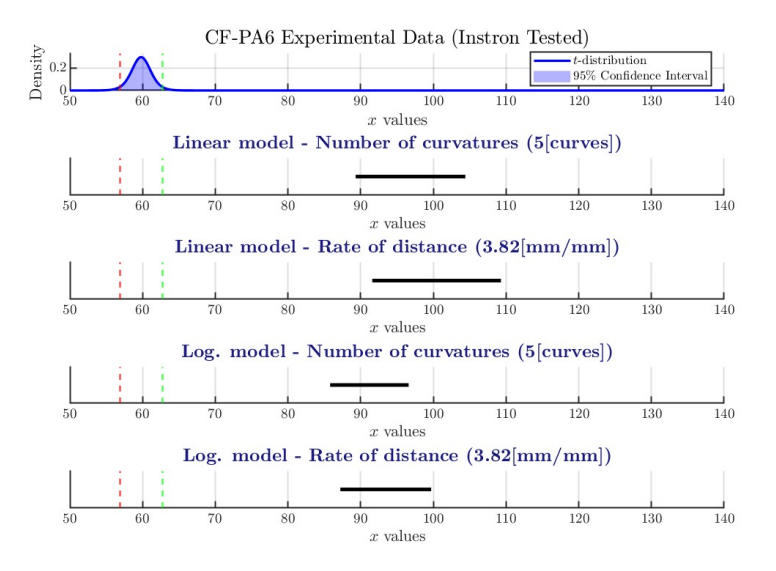


Figure 5.3: Confidence intervals curves of Experimental Data and Prediction Models for CF-PA6 tested at Instron.

Figure 5.4 shows the results for the IVW coupons, and as for the results of Instron, none of the models are capable of precisely predicting the SEA values.

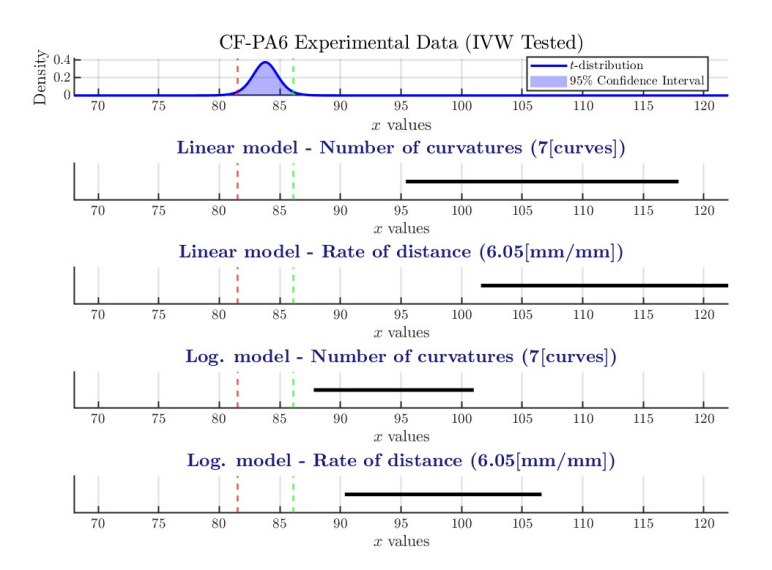


Figure 5.4: Confidence intervals curves of Experimental Data and Prediction Models for CF-PA6 tested at IVM.

CF-PC

Table 5.4 and figure 5.5 present the prediction results and experimental data for the IVW configuration. Only the logarithmic models performed acceptably, to be evaluated by statistical tests.

	Experimental Data				Prediction model			
Model	Data IVW		Data Instron		Linear model		Log. model	
	Lower	Upper	Lower	Upper	Lower	Upper	Lower	Upper
Number of curves - Short Corrugated					64.9	73.6	60.8	67.2
Rate of distance - Short Corrugated	62.1	67.7	_		67.6	77.9	62.3	69.6
Number of curves - IVW Corrugated	02.1			_	72.1	85.2	63.1	70.8
Rate of distance - IVW Corrugated					79.5	97.2	66.1	75.5

Table 5.4: Confidence intervals data of Experimental Data and Prediction Models for CF-PC (in all cases, values are given in $[kJ \cdot kg^{-1}]$).

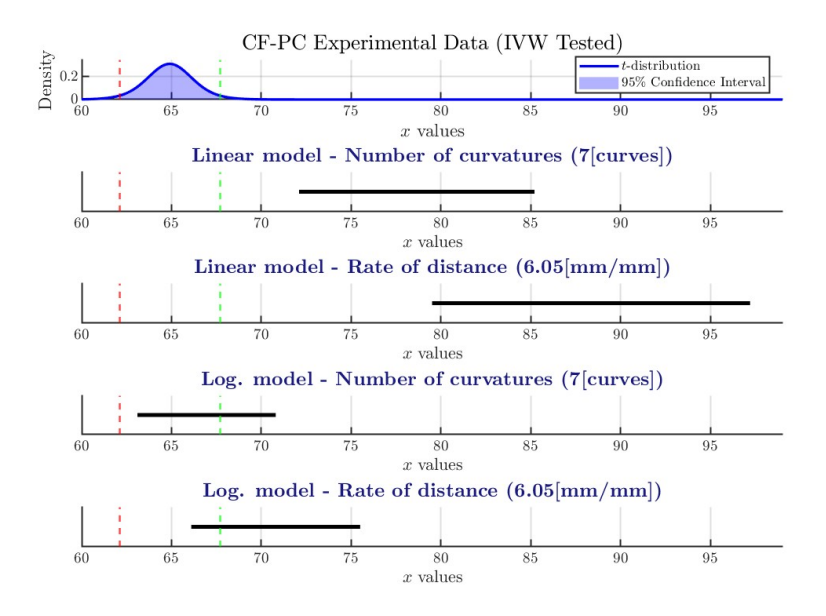


Figure 5.5: Confidence intervals curves of Experimental Data and Prediction Models for CF-PC

GF-TEPEX

For this material, the only predictive model that fell within the range of the experimental data tested at the IVW was the log. model with the parameter of the rate of distance. The results are shown in Table 5.1 and Figure 5.6.

	Experimental Data				Prediction model			
Model	Data IVW		Data Instron		Linear model		Log. model	
	Lower	Upper	Lower	Upper	Lower	Upper	Lower	Upper
Number of curves - Short Corrugated		67.7	_		52.2	61.1	45.4	52.1
Rate of distance - Short Corrugated	63.1				56.5	67.0	48.0	55.5
Number of curves - IVW Corrugated	05.1			_	64.0	77.3	49.2	57.1
Rate of distance - IVW Corrugated					76.3	94.0	54.2	63.8

Table 5.5: Confidence intervals data of Experimental Data and Prediction Models for GF-TEPEX (in all cases, values are given in $[kJ \cdot kg^{-1}]$).

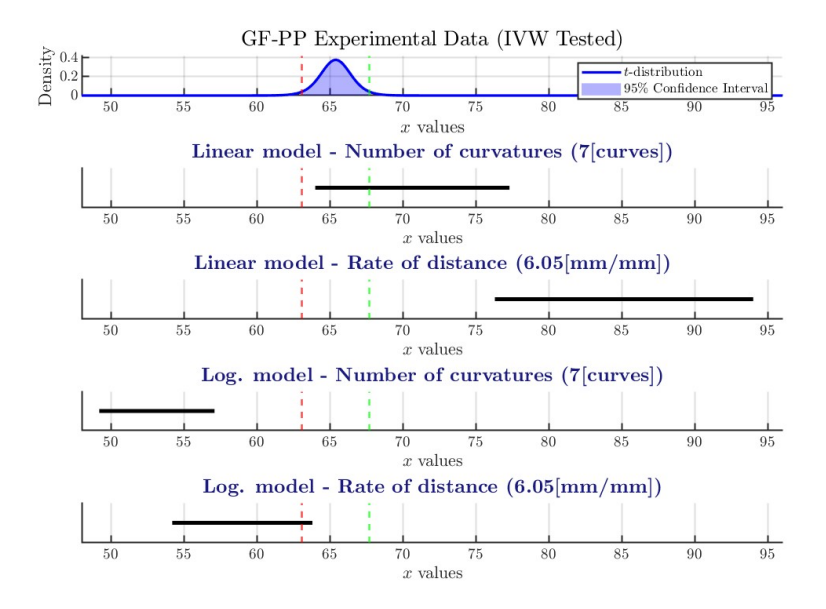


Figure 5.6: Confidence intervals curves of Experimental Data and Prediction Models for GF-TEPEX.

GF-PP

For the coupons tested and their prediction of the Instron geometry, Figure 5.7 exhibits the results obtained, and it can be observed that the linear models are capable of predicting the experimental SEA. The data are presented in Table 5.6.

	Experimental Data				Prediction model			
Model	Data IVW		Data Instron		Linear model		Log. model	
	Lower	Upper	Lower	Upper	Lower	Upper	Lower	Upper
Number of curves - Short Corrugated		45.0	40.1	46.2	39.5	43.2	31.5	34.2
Rate of distance - Short Corrugated	38.9				44.7	49.1	34.5	37.5
Number of curves - IVW Corrugated	36.9		40.1		53.7	59.2	35.9	39.2
Rate of distance - IVW Corrugated					68.4	75.9	41.8	45.8

Table 5.6: Confidence intervals data of Experimental Data and Prediction Models for GF-PP (in all cases, values are given in $[kJ \cdot kg^{-1}]$).

Equivalently, Figure 5.8 presents the results for the IVW geometry, for which the models capable of predicting the SEA are logarithmic.

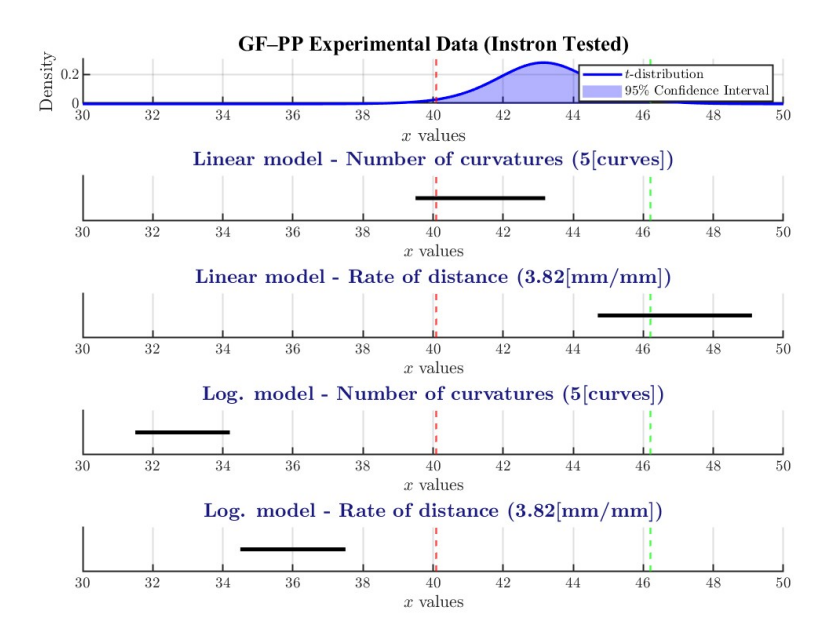


Figure 5.7: Confidence intervals curves of Experimental Data and Prediction Models for GF-PP tested at Instron.

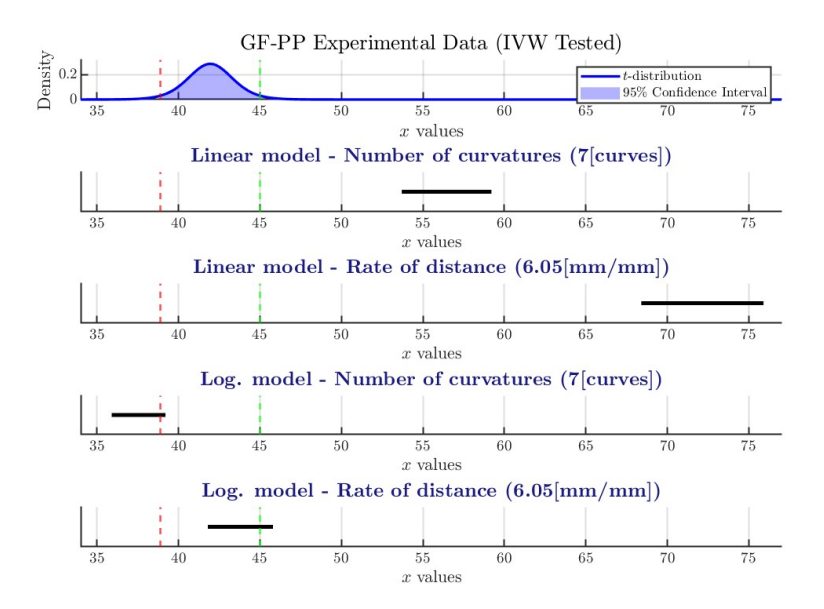


Figure 5.8: Confidence intervals curves of Experimental Data and Prediction Models for GF-PP tested at IVW.

5.3 Statistical Validation

Following the computation of confidence intervals and an initial assessment of their performance, a comprehensive statistical analysis is required to evaluate their efficacy and determine whether the predictions are statistically valid. To achieve this, was employ the null hypothesis framework previously utilized for data validation between the two institutions. In this context, the null hypothesis H_0 posits that $H_0: \bar{x}_{experimental} = \bar{x}_{predicted}$, while the alternative hypothesis H_a asserts that $H_a: \bar{x}_{experimental} \neq \bar{x}_{predicted}$. The results are presented in two categories: first, the models that are statistically validated as accurately predicting the SEA, and subsequently, the models that are not capable of predicting the SEA.

Material	Model	Error	Type I	Error Type II	
		$t_{ m critical}$	t-value	β (%)	
CF-Epoxy	Log. Model – Rate of distance	±2.20	-0.95	88.2	
Ст-Ероху	Log. Model – Num. of curvatures	± 2.20	0.32	95.6	
CF-PA66	Log. Model – Rate of distance	±2.16	-0.53	93.6	
CI'-1 A00	Log. Model – Num. of curvatures	± 2.16	1.46	75.1	
CF-PC	Log. Model – Rate of distance	± 2.16	-1.92	59.3	
OF-1 C	Linear Model – Num. of curvatures	± 2.16	-0.80	90.1	
GF-TEPEX Linear Model – Num. of curvatures		± 2.10	-1.09	83.7	
GF-TELEX	Log. Model – Rate of distance	± 2.10	1.83	60.4	
GF-PP	Linear Model – Rate of distance	± 2.16	1.29	80.0	
Gr-11	Log. Model – Num. of curvatures	± 2.20	-1.20	82.6	

Table 5.7: Null hypothesis results of predictive models with positive predictive outcomes.

Table 5.7 presents the results for the models that successfully predicted the SEA of experimental testing. Because the t-value falls in between the $t_{critical}$ interval, it can be inferred with a confidence of 95% that the $\bar{x}_{experimental} = \bar{x}_{predicted}$, which is the null hypothesis of the Error Type I. However, it is notable that for all of the models, β presents a high probability, which is the probability of not rejecting the model given that it does not predict correctly the SEA of experimental testing. The reason for β to be that high is the low degree of freedom available for each material.

The performance of the rest of the predictive models is presented in Table 5.8, which presents only the results for the null hypothesis test since the H_0 is rejected, there is no need to understand the β and as presented in the table all the rest of the models t_{value} do not fall in the $t_{critical}$ interval.

Material	Model	Error Type I		
		$t_{ m critical}$	t-value	
CE From	Linear Model – Rate of distance	± 2.20	-3.55	
CF-Epoxy	Linear Model – Num. of curvatures	$\pm \ 2.20$	-2.51	
CF-PA66	Linear Model – Rate of distance	$\pm \ 2.16$	-4.95	
Cr-rA00	Linear Model – Num. of curvatures	$\pm \ 2.16$	-3.04	
CF-PC	Linear Model – Rate of distance	$\pm \ 2.16$	-4.13	
Cr-rC	Linear Model – Num. of curvatures	$\pm \ 2.16$	-3.25	
GF-TEPEX	Log. Model – Num. of curvatures	$\pm \ 2.10$	4.24	
GI-TELEX	Linear Model – Rate of distance	$\pm \ 2.10$	-3.10	
GF-PP	Log. Model – Num. of curvatures	$\pm \ 2.18$	3.36	
Gr-FF	Linear Model – Rate of distance	± 2.18	-11.00	
CF-PA6	Linear Model – Rate of distance	$\pm \ 2.09$	-5.09	
Cr-rA0	Linear Model – Num. of curvatures	$\pm \ 2.09$	-4.71	
CF-PA6	Log. Model – Rate of distance	$\pm \ 2.09$	-4.11	
Or-1 A0	Log. Model – Num. of curvatures	$\pm \ 2.09$	-3.56	

Table 5.8: Null hypothesis results of predictive models with not capable predictive outcomes.

5.4 Performance of Prediction Models

Table 5.9 summarizes the performance of the predictive models described in Table 5.7. These models have been statistically proven to be capable of characterizing the influence of geometry on the SEA of the materials and are capable of predicting their behavior from flat coupons with only the characterization of the splaying and tearing setup.

It is clear that the model with outstanding predictive performance is the logarithm model with the rate of distance parameter, which is capable of correctly characterizing five out of the six composite materials and correctly predicts the SEA convergence trend as the rate of distance parameter increases and the geometry changes.

Materials correctly predicted	Predictive Model						
Materials correctly predicted	Num.	of curvatures	Rate of distance				
	Linear	Logarithm	Linear	Logarithm			
Short Corrugated geometry	1/3	1/3	0/3	1/3			
IVW Geometry	1/5	2/5	0/5	5/6			
Total	2/6	2/6	0/6	5/6			

Table 5.9: Performance of predictive models by materials correctly predicted.

Although the log. model with the rate of distance parameter exhibits great performance for most of the materials, for some specific materials, other models present a better fit with lower β values, as is the case for the linear model with the number of curvatures parameter for CF-PC and GF-TEPEX.

Chapter 6

Conclusions and Future Work

This study validated that composite materials exhibit complex failure mechanisms that are difficult to isolate. In addition, numerous parameters influence the performance of the specific energy absorption (SEA) of a material. Nonetheless, it has also demonstrated that these parameters can be predicted and understood. The principal conclusions are as follows.

- There is no single universal model applicable to all of the materials but specific models with specific parameters which characterize properly the behavior of the composite materials, reflecting the unique failure mechanics of each composite system, confirmed by the CF-PA6 material which none of the models were capable of correctly characterizing the behavior of the influence which the geometry has on it, confirming that there are particular parameters which drive the geometry influence to the SEA.
- The Logarithmic model driven by the rate of distance parameter has prove to be the most robust predictive framework, capable of predicting the geometry influence for the SEA for 5 out of 6 materials. However, there is a high risk of mistakenly accepting the prediction given that this one is false, whereas other models present a better statistical fit with lower (β) values, confirming the non-universality model.
- Crushing velocity is a parameter to be consider since it has been demonstrated that some composite materials like GF-PP are highly dependent to it, suffering severe degradation on its performance for dynamic load-

ings and for other materials as CF-PA66 experimental data shows that the performance of the material is linked to the crushing velocity.

This study has a major limitation, which is the relatively small sample size, which leads to wide confidence intervals and high Type II Errors (β) , reducing the statistical power of the conclusions and indicating that the predictive models, while promising, would benefit from validation with larger datasets.

The findings of this study present the opportunity to continue research on composite material failure mechanisms, refine the predictive models with larger sample sizes to improve the robustness of the statistical models, and being capable of refine the prediction towards more complex geometries. The importance of the crushing velocity given the nature of the SEA parameter is vital, and having a better understanding of the nature of the discrepancies in the performance of composite materials as soon as a dynamic load is imposed is crucial.

Bibliography

- [1] Serge Abrate. *Impact on Composite Structures*. Cambridge University Press, 1998.
- [2] ASTM International. ASTM D7136/D7136M-20: Standard Test Method for Measuring the Damage Resistance of a Fiber-Reinforced Polymer Matrix Composite to a Drop-Weight Impact Event. https://www.astm.org/d7136_d7136m-20.html, 2020. ASTM International, West Conshohocken, PA.
- [3] Béla Barényi. Vehicle body with deformation zones, 1952. Historical automotive safety.
- [4] Maomao Cui, Zhao Wang, Leigang Wang, and Yao Huang. Numerical simulation and multi-objective optimization of partition cooling in hot stamping of the automotive b-pillar based on rsm and nsga-ii. *Metals*, 10(9), 2020.
- [5] John Dagys. Toyota set to replace monocoque after sebring accident, 2023. Accessed: 2025-06-18.
- [6] European Environment Agency. Transport and environment report 2022, 2022.
- [7] European Rotorcraft Forum. Crashworthy design in helicopters, 2021. Accessed: 2025-05-24.
- [8] Gary L. Farley and Robert M. Jones. Energy-absorption capability of composite tubes and beams. Technical Report NASA-TM-101634, NASA, 1989. Work of the U.S. Government. Public use permitted.

- [9] Paolo Feraboli. Development of a modified flat-plate test specimen and fixture for composite materials crush energy absorption. *Journal of Composite Materials*, 43(19):1967–1990, 2009.
- [10] Paolo Feraboli and Ben Wade. Crashworthiness of automotive composite structures. *International Journal of Impact Engineering*, 38(4):254–263, 2011. CFRP crash behavior.
- [11] Paolo Feraboli, Bonnie Wade, Francesco Deleo, and Mostafa Rassaian. Crush energy absorption of composite channel section specimens. *Composite Structures*, 89(1):90–101, 2009. Departments: University of Washington and Boeing Phantom Works.
- [12] Paolo Feraboli, Brent Wade, Frank Deleo, Andrew Byar, and Todd Helms. Modular shock tube design for high strain rate testing of composite materials. *Composite Structures*, 94(3):895–904, 2012.
- [13] Yutong Fu and Xuefeng Yao. A review on manufacturing defects and their detection of fiber reinforced resin matrix composites. *Composites Part C: Open Access*, 8:100276, 2022.
- [14] Fei Ge, Yuan Lin, Fukai Zhang, Zhongwei Zhang, and Mingyang Wang. Crushing characteristics comparison between aluminum/cfrp and aluminum/cfrp/aluminum hybrid tubes. State Key Laboratory for Disaster Prevention & Mitigation of Explosion & Impact, Army Engineering University of PLA, 2023. Correspondence: ly9038@mail.ecust.edu.cn (Y.L.); zhangzhongwei.cn@gmail.com (Z.Z.).
- [15] S. Hanagud, J. I. Craig, P. Sriram, and W. Zhou. Energy absorption behavior of graphite epoxy composite sine webs. *Journal of Composite Materials*, 23:448–459, 1989.
- [16] D. Hull. A unified approach to progressive crushing of fibre-reinforced composite tubes. *Composites*, 22(5):377–385, 1991.
- [17] International Organization for Standardization. ISO 6603-2: Plastics Determination of puncture impact behaviour of rigid plastics Part

- 2: Instrumented impact testing. https://www.iso.org/standard/27699.html, 2000. ISO, Geneva, Switzerland.
- [18] International Organization for Standardization. ISO 179-2: Plastics Determination of Charpy impact properties Part 2: Instrumented impact test. https://www.iso.org/standard/74150.html, 2020. ISO, Geneva, Switzerland.
- [19] George C. Jacob, James F. Fellers, and Srboljub Simunovic. Energy absorption in polymer composites for automotive crashworthiness. *Journal of Composite Materials*, 36(7):813–850, 2002. SEA in composites.
- [20] George C. Jacob and J. Michael Starbuck. New test method for determining energy absorption mechanisms in polymer composite plates. Journal of Composite Materials, 34(7):575–593, 2000.
- [21] George C. Jacob, J. Michael Starbuck, Srdan Simunovic, and John F. Fellers. New test method for determining energy absorption mechanisms in polymer composite plates. *Polymer Composites*, 24(6):706–715, 2003. Accessed June 2025.
- [22] Dirk Lukaszewicz. Automotive composite structures for crashworthiness.

 Advanced Composite Materials for Automotive Applications: Structural

 Integrity and Crashworthiness, pages 99–127, 01 2013.
- [23] J. Morton, editor. Structural Impact and Crashworthiness, volume 1. Elsevier, London, 1984. Collection: Internet Archive Books; In Library; Print Disabled.
- [24] NASA. Planetary mission entry vehicles quick reference guide, 2022. Accessed: 2025-05-24.
- [25] Davide Salvatore Paolino. Course on lightweight design and composite materials. University lecture, 2024. Politecnico di Torino, Master's Degree in Mechanical Engineering.
- [26] Kevin Potter. Toward industrial implementation of robust automated composite manufacturing processes. In *Proceedings of the 17th Inter-*

- national Conference on Composite Materials (ICCM-17), page Plenary P1.5, 2009. Accessed: 2025-06-17.
- [27] United Nations Framework Convention on Climate Change (UNFCCC). Paris agreement, 2015. Accessed: Feb. 25, 2025.
- [28] Lorenzo Vigna. Development of an Innovative Procedure to Assess the Crashworthiness of Composite Materials. Doctoral dissertation, Politecnico di Torino, February 2022. Doctoral Program in Mechanical Engineering (35th Cycle).
- [29] Xinran Zhang, Robert Heusner, Zhaohui Jin, Andrew Hurst, Peter Horvath, Miroslav Krstic, David Wagner, Vivek Dwivedi, and Adam Joines. Crashworthiness evaluation of composite subfloor structure for evtol application. In SAE Technical Paper Series, number 2021-01-0286. SAE International, 2021.